

Anton Bochkarev

# **Cu Impurity Diffusion in TiN from First Principles**

Doctoral thesis

conducted at the Materials Center Leoben Forschung GmbH  
Austria

submitted at the Institute of Physics  
University of Graz  
Austria

under the supervision of  
Assoc.-Prof. Dr. P. Puschnig

Graz, 2017



# Abstract

Titanium nitride is an important technological material which has a broad spectrum of applications. One of such applications is to act as a diffusion barrier preventing the Cu interconnects in microelectronic components from interacting with surrounding materials. Despite a wide technological use, the atomic phenomena underlying the excellent performance of TiN as diffusion barrier are poorly understood. The results of the few experimental studies devoted to measuring the Cu diffusion coefficient in TiN are rather inconsistent and provide no clear information about the atomistic mechanisms of diffusion. However, such insights would be important for a rational design and improvement of the TiN-based diffusion barriers demanded by continuous miniaturization.

Motivated by the unsatisfactory state of the art, this work presents an extensive first-principles study of Cu impurity diffusion in bulk TiN aiming to discover the Cu diffusion mechanism. A number of mechanisms are examined: interstitial and vacancy-driven diffusion on both sublattices (Ti and N). In addition, we investigate the effect of the non-stoichiometry of TiN on its diffusion properties, for TiN is known to exist over the wide range of compositions. Moreover, we take into account the effect of temperature on all thermodynamic quantities within the quasiharmonic approximation. This way, we obtain the temperature dependent Cu diffusion coefficients in TiN for the considered mechanisms and TiN compositions.

On the basis of our findings, we conclude that Cu diffusion in stoichiometric TiN occurs via a vacancy mechanism on the Ti sublattice, while for N-deficient TiN it occurs via a vacancy mechanism on the N sublattice. Our results for the N-deficient TiN are in good agreement with the available high-temperature experimental data. The insights obtained in this work allow us to suggest a possible explanation for the discrepancy among the experimental measurements.



# Kurzzusammenfassung

Titannitrid ist ein technologisch relevantes Material mit einem breiten Anwendungsspektrum. Eine dieser Anwendungen ist die Verwendung als Diffusionsbarriere, die verhindert, dass Cu in mikroelektronischen Komponenten mit den Umgebungsmaterialien reagiert. Trotz der gängigen Verwendung als Diffusionsbarriere weiß man erst wenig über die zugrundeliegenden atomaren Vorgänge, auf denen die hervorragenden Diffusionseigenschaften von TiN basieren. Die spärlichen experimentellen Studien zur Diffusion von Cu in TiN sind widersprüchlich und geben keine klare Auskunft über den Diffusionsmechanismus selbst. Die Kenntnis des Mechanismus ist entscheidend für gezielte Verbesserungen, die durch die kontinuierliche Miniaturisierung notwendig gemacht werden.

Daher setzt sich diese Arbeit zum Ziel, die Massendiffusion von Cu in TiN mit Hilfe von ab-initio Methoden zu untersuchen und damit den Mechanismus der Diffusion von Cu in TiN aufzuklären. Dafür betrachten wir zwei verschiedene Mechanismen: interstitielle und Leerstellen-Diffusion auf beiden Untergittern (Ti und N). Zusätzlich wird der Effekt von nicht-stöchiometrischem TiN auf die Diffusion untersucht, denn TiN kommt in verschiedenen Zusammensetzungen vor. Weiteres wird der Effekt von Temperatur auf alle thermodynamischen Größen mittels der quasiharmonischen Näherung miteinbezogen. Auf diesem Weg erhalten wir temperaturabhängige Diffusionskoeffizienten für Cu in TiN für den gewählten Mechanismus und die TiN Zusammensetzung.

Aus unseren Erkenntnissen schließen wir, dass die Cu Diffusion in stöchiometrischem TiN über Leerstellen des Ti-Untergitters erfolgt, während in stickstoffarmen TiN die Leerstellen des N-Untergitters für die Diffusion infrage kommen. Unsere Ergebnisse für stickstoffarmes TiN zeigen gute Übereinstimmung mit Hoch-Temperatur Experimenten. Außerdem bieten unsere Erkenntnisse eine Erklärung, warum voneinander abweichen einzelne experimentelle Messungen.



# Contents

<b>Abstract</b>	<b>iii</b>
<b>Kurzzusammenfassung</b>	<b>v</b>
<b>1 Introduction</b>	<b>1</b>
<b>2 Density Functional Theory</b>	<b>5</b>
2.1 Many-electron Problem. Wave Function Methods . . . . .	5
2.2 Density Functional Theory . . . . .	7
2.2.1 Hohenberg & Kohn Theorem . . . . .	7
2.2.2 Density Variational Principle . . . . .	8
2.2.3 Kohn-Sham Self-Consistent Equations . . . . .	9
2.3 Exchange-Correlation Energy Functional . . . . .	11
2.3.1 Local Density Approximation . . . . .	11
2.3.2 Generalized Gradient Approximation . . . . .	12
<b>3 Diffusion in Solids</b>	<b>15</b>
3.1 Phenomenological Description . . . . .	15
3.2 Diffusion as a Random Walk . . . . .	16
3.3 Diffusion as a Migration Over an Energy Barrier . . . . .	20
3.4 Diffusion Mechanisms and Correlation . . . . .	25
3.4.1 Interstitial Mechanism . . . . .	25
3.4.2 Vacancy Mechanism . . . . .	26
<b>4 Point Defects</b>	<b>31</b>
4.1 Vacancies in Pure Metals . . . . .	31
4.2 Vacancies in Dilute Substitutional Binary Alloy . . . . .	35
4.3 Point Defects in Non-dilute Alloys . . . . .	36
<b>5 A Single-Volume Approach for Vacancy Formation Thermodynamics Calculations</b>	<b>39</b>
5.1 Introduction . . . . .	41
5.2 Thermodynamic Properties of Vacancies . . . . .	42
5.3 Computational Details . . . . .	44

## CONTENTS

5.4	Results . . . . .	46
5.5	Summary . . . . .	49
<b>6</b>	<b>Cu Diffusion in Single-crystal and Polycrystalline TiN Barrier Layers: A High-Resolution Experimental Study Supported by First-principles Calculations</b>	<b>51</b>
6.1	Introduction . . . . .	53
6.2	Experimental and Computational Details . . . . .	55
6.3	Experimental Results and Discussion . . . . .	57
6.3.1	Structure of Pristine TiN/Cu Stacks . . . . .	57
6.3.2	Diffusion in Annealed TiN/Cu Stacks . . . . .	61
6.4	Theoretical Considerations on Cu Diffusion in Single-crystal TiN(001)	66
6.4.1	Defect Concentrations . . . . .	68
6.4.2	Migration Barriers and Activation Energies . . . . .	70
6.5	Conclusions . . . . .	73
<b>7</b>	<b><i>Ab initio</i> Study of Cu Impurity Diffusion in Bulk TiN</b>	<b>75</b>
7.1	Introduction . . . . .	76
7.2	Methodology . . . . .	78
7.3	Computational Details . . . . .	80
7.4	Results and Discussion . . . . .	81
7.4.1	Thermal Properties . . . . .	81
7.4.2	Point Defects . . . . .	82
7.4.3	Migration Barriers . . . . .	84
7.4.4	Diffusion Coefficients . . . . .	87
7.5	Summary . . . . .	90
<b>8</b>	<b>Summary and Conclusions</b>	<b>93</b>
	<b>Acknowledgment</b>	<b>97</b>
	<b>List of Figures</b>	<b>99</b>
	<b>List of Tables</b>	<b>103</b>
	<b>Bibliography</b>	<b>105</b>

# Chapter 1

## Introduction

Miniaturization of the components in integrated circuits (IC), which is motivated by higher production costs and functional efficiency, still remains one of the major trends in the semiconductor industry [1]. Advancing size reduction poses an issue as the decrease in the IC spatial dimensions consequently leads to increase of the interconnect resistivity [2]. Thus, in order to diminish this problem Cu has been incorporated into IC as an interconnect material. Despite having low resistivity, copper interconnects possess some drawbacks: Cu atoms diffuse into the surrounding dielectric materials [3], doping Si with Cu leads to formation of deep energy levels in Si [4], and Cu also reacts with Si producing a  $\text{Cu}_3\text{Si}$  [5]. In order to prevent a resulting deterioration of the device's electrical performance, the Cu interconnects need to be isolated from the surrounding materials. This can be done by placing a diffusion barrier layer between copper and the dielectric. The perfect diffusion barrier should efficiently prevent interdiffusion of all the components and should not react with them. Moreover, it should have the least possible effect on the electrical characteristics of the metallic contact to the Si [6, 7]. Thanks to its high thermal and chemical stability as well as low resistivity, TiN appears to be a suitable candidate for a diffusion barrier between Cu and Si [8, 9].

The performance of the TiN barriers against Cu diffusion was studied in a great number of works [10–24]. The performance was graded according to the time a film can withstand a certain annealing temperature before failure, i.e., before Cu penetrates through the entire barrier film. It was shown that the diffusion properties of the TiN barrier films are affected by a number of characteristics, such as film density, composition, or microstructure. However, the exact mechanism of this influence is not clear. Several experimental studies went further and measured the diffusion coefficient of Cu in TiN within various temperature ranges [25–28]. In these works, the authors also attempted to interpret their measurements according to the certain types of diffusion mechanisms, e.g. bulk or grain boundary diffusion. However, the conclusions drawn from these works

## Chapter 1. Introduction

significantly differ from each other. For example, Chamberlain [25] obtained an activation energy of 4.43 eV for Cu diffusion in TiN for the temperature interval from 600 to 700°C and identified this as the grain boundary diffusion, while Lim *et al.* [26] for the temperatures 400-640°C reported an activation energy of only 0.29 eV and also identified this as the grain boundary diffusion. Clearly, a detailed study of the atomistic mechanisms of diffusion in TiN is required to address this discrepancy. The first *ab initio* study of Cu diffusion in TiN was done by Tsetseris *et al.* [29]. In this work, the authors considered several diffusion mechanisms and calculated corresponding migration barriers, which allowed them to estimate the relative importance of different mechanisms. However, this is not enough to draw an unambiguous conclusion regarding the operative diffusion mechanism since the effect of temperature was not taken into account.

The main goal of this work is to obtain not only the migration barriers, but the full temperature-dependent diffusion coefficient for Cu impurity migration in TiN. Calculating the absolute values of the diffusion coefficients corresponding to the various diffusion mechanisms allows to uniquely identify the operative mechanism for Cu diffusion. Moreover, the knowledge of the mechanism and corresponding diffusion coefficient makes possible the direct comparison between the theory and experiment, and therefore, can help understanding the origin of the observed diffusion behavior as well as the ways to control it.

This work is structured as follows. In the first three chapters an overview of the theoretical methods, which are applied in this work, is given. In Chapter 2 we briefly review the basics of density functional theory, including its essential equations and the most common approximations for the exchange-correlation energy. Then, in Chapter 3 we consider diffusion process in solids. Applying the theory of random walk, we write equations for the diffusion coefficient for several atomistic diffusion mechanisms. The correlation effect and calculation of the jump rates are also discussed. Chapter 4 deals with the theory of point defects. There, we obtain relations for calculating the concentrations of point defects in the monoatomic systems as well as in the dilute and concentrated alloys.

In Chapter 5 we introduce a simplified approach for obtaining the vacancy formation free energies from *ab initio* calculations. The formation free energies are required for calculating the concentrations of defects which are, in turn, used for calculating diffusion coefficient.

In Chapter 6 we begin investigating the Cu impurity diffusion in bulk TiN. We identify the most abundant point defects as the function of TiN composition and correspondingly choose the diffusion mechanism for our study. The respective migration barriers are calculated and the correlation effect is acknowledged. As a result, we evaluate the activation energies for considered diffusion mechanisms. The effect of temperature is not explicitly taken into account at this stage.

Finally, Chapter 7 extends the results of the previous chapter by considering the

effect of temperature. The vibrational free energy contributions are computed for all thermodynamic quantities. Thus, we obtain the temperature dependent coefficients for Cu diffusion in bulk TiN. We identify the operative diffusion mechanisms depending on the TiN stoichiometry and compare results of our calculations to the available experimental data. The remarkable agreement between theory and experiment allows us for the interpretation of the experimental measurements on the basis of the theoretical calculations.



# Chapter 2

## Density Functional Theory

In this thesis, all calculations are performed within the formalism of the density functional theory (DFT). Therefore, a brief overview of the basic principles of the theory are presented below, including summary of its advantages and limitations. The most common approximations to the exchange-correlation functional are discussed.

### 2.1 Many-electron Problem. Wave Function Methods

If one interested in calculating the properties of a many-electron system, this can be achieved via solving the time-independent Schrödinger equation:

$$\left( \underbrace{-\frac{1}{2} \sum_{i=1}^N \nabla_i^2}_{\hat{T}} + \underbrace{\frac{1}{2} \sum_i \sum_{j \neq i} \frac{1}{|\mathbf{r}_i - \mathbf{r}_j|}}_{\hat{U}} - \underbrace{\sum_{i,l} \frac{Z_l}{|\mathbf{r}_i - \mathbf{R}_l|}}_{\hat{V}_{ext}} \right) \Psi(\mathbf{r}_1, \dots, \mathbf{r}_N) = E \Psi(\mathbf{r}_1, \dots, \mathbf{r}_N). \quad (2.1)$$

Here,  $\Psi(\mathbf{r}_1, \dots, \mathbf{r}_N)$  is the many-electron wave function with  $\mathbf{r}_i$  denoting spatial and spin coordinates of the  $i$ -th electron from the total number of  $N$  electrons. The first term in parentheses in (2.1) is the kinetic energy of the electrons, the second terms is the repulsive Coulomb interaction involving pairs of electrons and the third term represents the attractive Coulomb interaction of electrons with nuclei (index  $l$  runs over the number of nuclei). Within the Born-Oppenheimer approximation [30] which is utilized throughout this work, the electronic and nuclear variables are treated separately. Then, if one interested in solving the electronic problem of the many-electron system, the nuclear kinetic energy can

## Chapter 2. Density Functional Theory

be neglected and the nuclear coordinates  $\mathbf{R}_l$  enter equation (2.1) as parameters. Note that we use atomic units, so that

$$\frac{e^2}{4\pi\epsilon_0} = \hbar = m_e = 1, \quad (2.2)$$

where  $e$  is the electronic charge,  $\epsilon_0$  is the vacuum permittivity,  $\hbar$  is Planck's constant, and  $m_e$  is the electronic mass.

The many-electron wave function  $\Psi(\mathbf{r}_1, \dots, \mathbf{r}_N)$  contains all possible information about the system. But since it is a function of many variables it is possible to solve Eq. 2.1 only for very simple cases. Therefore, some approximation to the wave function has to be found. A widely used approach is to represent the wave function in terms of a single Slater determinant  $\Phi$ :

$$\Phi = \frac{1}{\sqrt{N!}} \sum_P (-1)^P \psi_1(P1) \psi_2(P2) \dots \psi_N(PN), \quad (2.3)$$

where  $\psi_i$  are single-particle wave functions (orbitals) which are the eigenfunctions of a single-particle time-independent Schrödinger equation.  $P$  is any permutation of the labels  $1, 2, \dots, N$ , and  $(-1)^P$  equals  $+1$  for an even permutation and  $-1$  for an odd permutations. This accounts for the fact that the electronic wave function has to be antisymmetric upon permutations, as it describes a fermionic system. The method which uses a single Slater determinant as a representation of a many-electron wave function is known as the Hartree-Fock approximation [31, 32]. A single Slater determinant, however, does not provide sufficient accuracy since electron correlations are not taken into account. A considerable improvement can be achieved by taking into account a linear combination of Slater determinants each with a different configuration of single electron orbitals. This leads to the configuration interaction (CI) method. CI is, in principle, exact, however, its accuracy depends on the number of configurations included. And the number of required configurations grows rapidly when increasing the number of electrons in the system [33]. Therefore, only relatively small systems with a limited amount of electrons can be treated accurately with the CI method.

On the contrary, methods based on the electronic density do not require explicitly calculating the many-electron wave function. All the information about an  $N$  electron system can be determined from its ground state density,  $n(\mathbf{r})$ . Thus, in the following sections we will discuss the method allowing such calculations, namely density functional theory (DFT).

## 2.2 Density Functional Theory

### 2.2.1 Hohenberg & Kohn Theorem

The basis for DFT provides the Hohenberg-Kohn [34] theorem. It states that the density  $n(\mathbf{r})$  of a nondegenerate ground state of a bound system of interacting electrons in some external potential  $v(\mathbf{r})$  determines this potential uniquely (up to an arbitrary additive constant). The proof of this theorem can be done by demonstrating that the negation of the theorem leads to a contradiction. Suppose  $n(\mathbf{r})$  is the density of a nondegenerate ground state of  $N$  electrons in the potential  $v_1(\mathbf{r})$ , which corresponds to the ground state  $\Psi_1$ , and the energy  $E_1$ . Then,

$$E_1 = \langle \Psi_1 | \hat{H}_1 | \Psi_1 \rangle = \int v_1(\mathbf{r})n(\mathbf{r})d\mathbf{r} + \langle \Psi_1 | \hat{T} + \hat{U} | \Psi_1 \rangle, \quad (2.4)$$

where  $\hat{H}_1$  is the total Hamiltonian corresponding to  $v_1(\mathbf{r})$ , and  $\hat{T}$  and  $\hat{U}$  are the kinetic and potential energy operators defined in Eq. (2.1). Now, let us assume that there is a second potential  $v_2(\mathbf{r})$ , different from  $v_1(\mathbf{r})$ , with ground state  $\Psi_2$ , which give rise to the same  $n(\mathbf{r})$ . Thus,

$$E_2 = \int v_2(\mathbf{r})n(\mathbf{r})d\mathbf{r} + \langle \Psi_2 | \hat{T} + \hat{U} | \Psi_2 \rangle. \quad (2.5)$$

Then, according to the Rayleigh-Ritz minimal principle for  $\Psi_1$  gives the following inequality

$$\begin{aligned} E_1 &< \langle \Psi_2 | \hat{H}_1 | \Psi_2 \rangle \\ &= \int v_1(\mathbf{r})n(\mathbf{r})d\mathbf{r} + \langle \Psi_2 | \hat{T} + \hat{U} | \Psi_2 \rangle \\ &= E_2 + \int [v_1(\mathbf{r}) - v_2(\mathbf{r})] n(\mathbf{r})d\mathbf{r}. \end{aligned} \quad (2.6)$$

Equivalently,

$$E_2 < \langle \Psi_1 | \hat{H}_2 | \Psi_1 \rangle = E_1 + \int [v_2(\mathbf{r}) - v_1(\mathbf{r})] n(\mathbf{r})d\mathbf{r}. \quad (2.7)$$

Adding Eqs. (2.6) and (2.7) leads to the contradiction

$$E_1 + E_2 < E_1 + E_2, \quad (2.8)$$

from what follows that our initial assumption of the existence of a second potential  $v_2(\mathbf{r})$ , which is not equal to  $v_1(\mathbf{r})$  but leads to the same density  $n(\mathbf{r})$  is wrong.

## Chapter 2. Density Functional Theory

Thus, the Hohenber & Kohn theorem is proven. Note that the requirement of the non-degeneracy of the ground state considered during proof can be lifted [35].

The density  $n(\mathbf{r})$  determines  $v(\mathbf{r})$  as well as  $N$  through

$$N = \int n(\mathbf{r})d\mathbf{r}, \quad (2.9)$$

therefore, it provides the full Hamiltonian  $\hat{H}$  for the electronic system. Consequently, the density  $n(\mathbf{r})$  implicitly contains all properties derivable from  $\hat{H}$  via solution of the Schrödinger equation.

### 2.2.2 Density Variational Principle

The most important property of an electronic ground state is its total energy  $E_0$  [36]. According to the Rayleigh-Ritz principle, it can be found by minimizing  $\langle \Psi | \hat{H} | \Psi \rangle$  over all normalized, antisymmetric  $N$ -particle wave functions  $\Psi$  [37]:

$$E_0 = \min_{\Psi} \langle \Psi | \hat{H} | \Psi \rangle. \quad (2.10)$$

The formulation of the minimal principle in terms of density can be separated into two steps [38]. First we consider all wave functions  $\Psi$  which give a given density  $n(\mathbf{r})$ , and minimize over those wave functions:

$$E_v[n(\mathbf{r})] = \min_{\Psi \rightarrow n(\mathbf{r})} \langle \Psi | \hat{H} | \Psi \rangle = \min_{\Psi \rightarrow n(\mathbf{r})} \langle \Psi | \hat{T} + \hat{U} | \Psi \rangle + \int v(\mathbf{r})n(\mathbf{r})d\mathbf{r}, \quad (2.11)$$

where we use the fact that all wave functions that give the same  $n(\mathbf{r})$  also give the same  $v(\mathbf{r})$ . Then we define the universal functional

$$F[n(\mathbf{r})] = \min_{\Psi \rightarrow n(\mathbf{r})} \langle \Psi | \hat{T} + \hat{U} | \Psi \rangle = \langle \Psi_n^{min} | \hat{T} + \hat{U} | \Psi_n^{min} \rangle, \quad (2.12)$$

where  $\Psi_n^{min}$  is that wave function which provides the minimum for a given  $n(\mathbf{r})$ . Finally we minimize over all  $N$ -electron densities  $n(\mathbf{r})$ :

$$\begin{aligned} E_0 &= \min_{n(\mathbf{r})} E_v[n(\mathbf{r})] \\ &= \min_{n(\mathbf{r})} \left( F[n(\mathbf{r})] + \int v(\mathbf{r})n(\mathbf{r})d\mathbf{r} \right). \end{aligned} \quad (2.13)$$

The potential  $v(\mathbf{r})$  is held fixed during minimization and thus, the minimizing density is the ground state density. Thus, Eq. (2.13) represents the density or Hohenberg-Kohn variational principle.

### 2.2.3 Kohn-Sham Self-Consistent Equations

We now write the Hohenberg-Kohn variational principle for a fictitious system of noninteracting electrons moving in the external potential  $v_s(\mathbf{r})$  [36, 39], so it reads as

$$E_{v_s(\mathbf{r})}[n(\mathbf{r})] \equiv \int v_s(\mathbf{r})n(\mathbf{r})d\mathbf{r} + T_s[n(\mathbf{r})] \geq E, \quad (2.14)$$

where  $T_s[n(\mathbf{r})]$  is the kinetic energy functional of the ground state of noninteracting electrons with density distribution  $n(\mathbf{r})$ . We use the  $\geq$  sign because the nondegeneracy of the ground state was not assumed.

The Euler-Lagrange equations, with the constraint of the constant total number of particles (2.9), has the following form

$$\delta E_v[n(\mathbf{r})] \equiv \int \delta n(\mathbf{r}) \left( v(\mathbf{r}) + \frac{\delta}{\delta n(\mathbf{r})} T_s[n(\mathbf{r})] - \epsilon \right) d\mathbf{r} = 0, \quad (2.15)$$

where  $n(\mathbf{r})$  is the ground state density for  $v(\mathbf{r})$ . The Lagrange multiplier  $\epsilon$  ensures that the number of electrons is fixed. For this case, the ground state energy and density can be obtained as

$$E = \sum_{i=1}^N \epsilon_i; \quad n(\mathbf{r}) = \sum_{i=1}^N |\phi_i(\mathbf{r})|^2, \quad (2.16)$$

where  $\epsilon_i$  and  $\phi_i(\mathbf{r})$  are respectively the eigenvalues and eigenfunctions of the noninteracting, single-particle equations

$$\left( -\frac{1}{2}\nabla^2 + v_s(\mathbf{r}) - \epsilon_i \right) \phi_i(\mathbf{r}) = 0. \quad (2.17)$$

Considering now the problem of interacting electrons, we decompose the functional  $F[n(\mathbf{r})]$  of Eq. (2.12) into the following terms

$$F[n(\mathbf{r})] = T_s[n(\mathbf{r})] + \frac{1}{2} \int \frac{n(\mathbf{r})n(\mathbf{r}')}{|\mathbf{r} - \mathbf{r}'|} d\mathbf{r}d\mathbf{r}' + E_{xc}[n(\mathbf{r})]. \quad (2.18)$$

Here, the first term on the right side is the kinetic energy functional for noninteracting electrons, Eq. (2.14). The second term is the electro-static Hartree energy [31]. The last term is the so-called exchange-correlation energy functional and it is defined by Eq. (2.18). It contains, in principle, all many-body effects, which are not accounted for in the first two terms.

## Chapter 2. Density Functional Theory

Now, the Hohenberg-Kohn variational principle for interacting electrons has the following form

$$E_v[n(\mathbf{r})] \equiv \int v(\mathbf{r})n(\mathbf{r})d\mathbf{r} + T_s[n(\mathbf{r})] + \frac{1}{2} \int \frac{n(\mathbf{r})n(\mathbf{r}')}{|\mathbf{r} - \mathbf{r}'|} d\mathbf{r}d\mathbf{r}' + E_{xc}[n(\mathbf{r})] \geq E. \quad (2.19)$$

The corresponding Euler-Lagrange equations, for a given total number of electrons has the form

$$\delta E_v[n(\mathbf{r})] \equiv \int \delta n(\mathbf{r}) \left( v_{\text{eff}}(\mathbf{r}) + \frac{\delta}{\delta n(\mathbf{r})} T_s[n(\mathbf{r})] - \epsilon \right) d\mathbf{r} = 0, \quad (2.20)$$

where

$$v_{\text{eff}}(\mathbf{r}) = v(\mathbf{r}) + \int \frac{n(\mathbf{r}')}{|\mathbf{r} - \mathbf{r}'|} d\mathbf{r}' + v_{xc}(\mathbf{r}) \quad (2.21)$$

and

$$v_{xc}(\mathbf{r}) \equiv \frac{\delta}{\delta n(\mathbf{r})} E_{xc}[n(\mathbf{r})]. \quad (2.22)$$

Now the form of Eq. (2.20) is identical to Eq. (2.15) for noninteracting electrons moving in some effective external potential  $v_{\text{eff}}(\mathbf{r})$  instead of  $v_s(\mathbf{r})$ . This means that minimizing  $n(\mathbf{r})$  can be obtain via solving the single-particle equation

$$\left( -\frac{1}{2}\nabla^2 + v_{\text{eff}}(\mathbf{r}) - \epsilon_i \right) \phi_i(\mathbf{r}) = 0, \quad (2.23)$$

with

$$n(\mathbf{r}) = \sum_{i=1}^N |\phi_i(\mathbf{r})|^2 \quad (2.24)$$

and  $v_{\text{eff}}(\mathbf{r})$  defined by Eq. (2.21). The set of Eqs. (2.21)-(2.24) has to be solved self-consistently since the local exchange-correlation potential (2.22) functionally depends on the density distribution  $n(\mathbf{r})$ . These equations are called Kohn-Sham equations. The self-consistent procedure carries on as follows: one begins with a trial effective potential  $v_{\text{eff}}$ , then diagonalizes the equations (2.23) producing the one-electron energies  $\epsilon_i$  and orbitals  $\phi_i(\mathbf{r})$ , which are used to create the density  $n(\mathbf{r})$  via (2.24). This density then determines a new effective potential through

## 2.3. Exchange-Correlation Energy Functional

equations (2.21) and (2.22). The procedure is repeated until the ground state density is converged. The ground state energy  $E$  is then given by

$$E = \sum_i \epsilon_i + E_{xc}[n(\mathbf{r})] - \int v_{xc}(\mathbf{r})n(\mathbf{r})d\mathbf{r} - \frac{1}{2} \int \frac{n(\mathbf{r})n(\mathbf{r}')}{|\mathbf{r} - \mathbf{r}'|}d\mathbf{r}d\mathbf{r}'. \quad (2.25)$$

The practical usefulness of ground-state DFT depends entirely on whether approximations for the functional  $E_{xc}[n(\mathbf{r})]$  can be found which are at the same time sufficiently simple and sufficiently accurate [36]. In the next sections we briefly introduce the most common approximations to the exchange-correlation energy functional.

## 2.3 Exchange-Correlation Energy Functional

### 2.3.1 Local Density Approximation

The most simple approximation for  $E_{xc}[n(\mathbf{r})]$  (2.18) has already been proposed in the original work of Kohn and Sham [39] and is called the local-density approximation (LDA). If  $n(\mathbf{r})$  is varying sufficiently slowly, then it can be shown [34] that

$$E_{xc}^{LDA}[n(\mathbf{r})] = \int e_{xc}(n(\mathbf{r}))n(\mathbf{r})d\mathbf{r}, \quad (2.26)$$

where  $e_{xc}(n)$  is the exchange-correlation energy per particle of a uniform electron gas of density  $n$ . Its exchange part,  $e_x(n)$ , can be evaluated analytically and is given as

$$e_x(n) = -\frac{3}{4\pi}(3\pi^2n)^{\frac{1}{3}} = -\frac{3}{4\pi} \frac{(9\pi/4)^{\frac{1}{3}}}{r_s} = -\frac{0.458}{r_s}, \quad (2.27)$$

where  $r_s$  is the Wigner-Seitz radius defined as  $(4\pi/3)r_s^3 = n^{-1}$ .

Exact analytic expressions for the correlation energy part,  $e_c(n)$ , are known only in extreme limits, namely in the high-density limit ( $r_s \rightarrow 0$ ) or the weak-coupling limit [40] and in the low-density limit ( $r_s \rightarrow \infty$ ) or the strong coupling limit [41]. An expression which encompasses both limits can be written in the following form [42]

$$e_c(n) = -2c_0(1 + \alpha_1 r_s) \ln \left( 1 + \frac{1}{2c_0(\beta_1 r_s^{1/2} + \beta_2 r_s + \beta_3 r_s^{3/2} + \beta_4 r_s^2)} \right), \quad (2.28)$$

where

$$\beta_1 = \frac{1}{2c_0} \exp\left(-\frac{c_1}{2c_0}\right), \quad (2.29)$$

$$\beta_2 = 2c_0\beta_1^2. \quad (2.30)$$

The coefficients  $c_0 = 0.031091$  and  $c_1 = 0.046644$  are known from the many-body perturbation theory results for high-density limit [40], while  $\alpha_1 = 0.21370$ ,  $\beta_3 = 1.6382$ , and  $\beta_4 = 0.49294$  were obtained by fitting to accurate quantum Monte Carlo correlation energies by [43]. These parameters provide representation of the correlation energy of the non spin-polarized system. Representations for the other types of systems are also available [44, 45].

It is obvious that LDA is exact for a uniform electron gas. It was expected to be valid only for densities varying slowly on the scale of the local Fermi wavelength  $\lambda_F$ . However, LDA has proven to be useful for many systems which deviate significantly from a uniform electron gas. Being much more easier to solve, comparing for example to the Hartree-Fock equations, the Kohn-Sham equations in the LDA give ionization energies of atoms, dissociation energies of molecules and cohesive energies with an error within 10-20%. At the same time, the error for bond lengths of molecules and lattice parameters of solids is only a few percent. Owing to its simplicity and accuracy, the LDA is still in use today despite the existence of the generally more accurate gradient approximations, which we discuss in the next section.

### 2.3.2 Generalized Gradient Approximation

The natural way for improvement of the LDA (2.26), which is the first term of the gradient expansion [36, 39, 46] for the slowly varying electronic densities, might appear to be the inclusion of the higher terms of the expansion. However, the second-order gradient expansion approximation (GEA)

$$E_{xc}^{GEA}[n(\mathbf{r})] = \int e_{xc}(n(\mathbf{r}))n(\mathbf{r})d\mathbf{r} + \int C_{xc}(n(\mathbf{r}))\frac{|\nabla n(\mathbf{r})|^2}{n(\mathbf{r})^{4/3}}d\mathbf{r}, \quad (2.31)$$

provides no systematic improvement to the LDA but, on the contrary, often worsens its results. The reason for this failure arises from the unphysical behavior of the GEA exchange and correlation holes [47]. The remedy is called generalized gradient approximations (GGA) and has the following form for the exchange-correlation energy:

$$E_{xc}^{GGA}[n(\mathbf{r})] = \int f(n(\mathbf{r}), \nabla n(\mathbf{r}))d\mathbf{r}. \quad (2.32)$$

### 2.3. Exchange-Correlation Energy Functional

Here, the function of density and its gradient  $f$  is chosen to satisfy known exact properties of the exchange-correlation energy. This is achieved via introducing a cut-off procedure to get rid of the spurious long range part of the GEA exchange and correlation hole. The GGA generally improves over the LDA description for structural properties for systems significantly different from the uniform electron gas, such as molecules. For solids, however, the error is of similar magnitude as for the LDA but of the opposite sign for most of the cases [48, 49]. While the LDA tends to underestimate the lattice constants of solids, the GGA with approximately the same error overestimates the bond length. While there is only one LDA, there are many different variants of GGA in use [50–52]. Currently the most widely used implementation of the GGA is the PBE functional [53]. There also exists a modification of this functional developed specifically to improve the description of solids and is called the PBEsol [54]. This particular functional is used in the first principles calculations performed in the current work.



# Chapter 3

## Diffusion in Solids

### 3.1 Phenomenological Description

The equation which formally describes the diffusive motion of particles in an isotropic medium has been first written in 1855 by Fick [55] and has the following form:

$$\mathbf{J}_i = -D_i \nabla C_i \quad (3.1)$$

This equation is called Fick's first law and relates the flux of the  $i$ -th component,  $\mathbf{J}_i$ , with its concentration gradient  $\nabla C_i$  through a coefficient of proportionality  $D_i$ , which is called the diffusion coefficient or the diffusivity of the component. The diffusion flux has dimension of par  $\text{m}^{-2}\text{s}^{-1}$  (number of particles (moles) traveling through the unit area per unit time) and the concentration has dimension of par  $\text{m}^{-3}$  (number of particles (moles) per unit volume). Thus, the diffusion coefficient has dimension of  $\text{m}^2\text{s}^{-1}$ .

If the number of diffusing particles during diffusion process is conserved, which is usually the case, the continuity equation for diffusion process can be written [56]:

$$-\nabla \cdot \mathbf{J}_i = \frac{\partial C_i}{\partial t} \quad (3.2)$$

Combining equation (3.2) and Fick's first law (3.1), assuming that the diffusion coefficient does not depend on concentration, one obtains Fick's second law:

$$\frac{\partial C_i}{\partial t} = D_i \Delta C_i \quad (3.3)$$

This equation is also called the diffusion equation. The solution of the diffusion equation provides the spatial and temporal distribution of the concentration [57].

## Chapter 3. Diffusion in Solids

By measuring the concentration distribution in an experiment and using an appropriate solution of the diffusion equation the diffusion coefficient can be obtained [58].

In the number of experiments, it is also observed that the temperature dependence of the diffusion coefficient can be accounted for by an Arrhenius equation:

$$D = D_0 \exp\left(-\frac{Q}{k_B T}\right). \quad (3.4)$$

Here, the pre-exponential factor  $D_0$  and the activation energy  $Q$  are assumed to be temperature independent. Plotting the experimental dependence  $D(T)$  in the coordinates  $\ln(D)$  vs.  $1/T$  one obtains  $D_0$  and  $Q$ . These quantities serve as quantitative parameters for describing of the diffusion properties of the particular system and also have proven useful in establishing a qualitative connection between diffusion and the other thermal properties of the materials.

### 3.2 Diffusion as a Random Walk

Despite the practical importance of equations (3.1) and (3.3), they provide no information about the atomistic nature of the diffusion process. In 1905, Einstein related the diffusion coefficient to the microscopic random motion, the Brownian motion, of the particles [59, 60]. Considering motion of in total  $N$  particles, Einstein introduced a quantity  $\delta$  which represents the change in position in one dimension  $x$  of an individual particle within the time interval  $\tau$ . The value of  $\delta$  is different for each particle and has a certain probability distribution  $\phi(\delta)$  such, that the number  $dN$  of the particles which are shifted between  $\delta$  and  $\delta+d\delta$  within the time interval  $\tau$  can be written in the following form

$$dN = N\phi(\delta)d\delta, \quad (3.5)$$

where

$$\int_{-\infty}^{+\infty} \phi(\delta)d\delta = 1. \quad (3.6)$$

Moreover,  $\phi$  only differs from zero for small values of  $\delta$  and fulfils the requirement

$$\phi(\delta) = \phi(-\delta). \quad (3.7)$$

Assuming that the number of particles per unit volume  $\rho$  depends only on  $x$  and  $t$ , and using a Taylor series one gets the following:

### 3.2. Diffusion as a Random Walk

$$\begin{aligned}
\rho(x, t + \tau) &= \rho(x, t) + \tau \frac{\partial \rho}{\partial t} + O(\tau^2) \\
&= \int_{-\infty}^{+\infty} \rho(x + \delta, t) \phi(\delta) d\delta \\
&= \rho \int_{-\infty}^{+\infty} \phi(\delta) d\delta + \frac{\partial \rho}{\partial x} \int_{-\infty}^{+\infty} \delta \phi(\delta) d\delta + \frac{\partial^2 \rho}{\partial x^2} \int_{-\infty}^{+\infty} \frac{\delta^2}{2} \phi(\delta) d\delta + \dots
\end{aligned} \tag{3.8}$$

In the first line of the equation we neglect the high order terms because  $\tau$  is very small. Using a Taylor expansion for  $\rho(x + \delta, t)$  leads to the third line of (3.8). Note that the terms containing odd powers of  $\delta$  vanish due to the symmetry property (3.7). The integral in the first term is equal to one due to the definition of  $\phi(\delta)$  (3.6). Taking into account only the first and the third terms in the third line of the equation (3.8) and denoting

$$D = \frac{1}{\tau} \int_{-\infty}^{+\infty} \frac{\delta^2}{2} \phi(\delta) d\delta, \tag{3.9}$$

equation (3.8) transforms into the following:

$$\frac{\partial \rho}{\partial t} = D \frac{\partial^2 \rho}{\partial x^2}. \tag{3.10}$$

In this differential equation one can identify the diffusion equation (3.3) for one dimension with  $D$  being the diffusion coefficient. Assuming that  $N$  particles start their mutually independent movements at the origin at the initial time  $t = 0$ , the diffusion equation has the following solution:

$$\rho(x, t) = \frac{N}{\sqrt{4\pi Dt}} e^{-\frac{x^2}{4Dt}}. \tag{3.11}$$

From this equation, the mean square displacement of the particle in the direction of the  $x$ -axis can be calculated as

$$\langle x^2 \rangle = 2Dt. \tag{3.12}$$

For an isotropic medium, the displacements along the  $x$ -,  $y$ - and  $z$  axis are equal. Therefore, with  $R$  being the total displacement of the particle

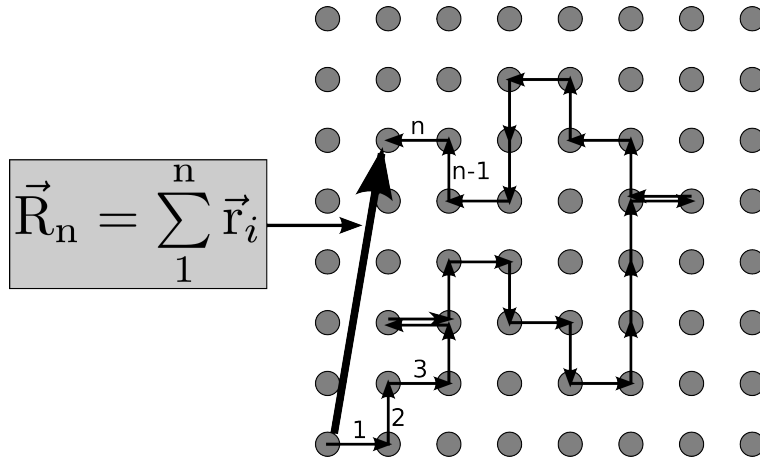


**Figure 3.1:** Schematic illustration for a random walk of a particle on a lattice

$$\langle x^2 \rangle = \langle y^2 \rangle = \langle z^2 \rangle = \frac{1}{3} \langle R^2 \rangle \quad (3.13)$$

and

$$D = \frac{\langle R^2 \rangle}{6t}. \quad (3.14)$$

Equations (3.12) and (3.14) relate the diffusion coefficient of the particle with its mean square displacement which is known as the Einstein relation.

Now let us consider the random walk of a particle on a lattice. In this case, the total displacement  $\mathbf{R}$  of a particle is composed of a sequence of many individual nearest-neighbor jumps of discrete length  $d$ . If the coordination number of lattice is  $Z$ , then each jump direction will occur with the probability  $1/Z$ .

According to Fig. 3.1 the total displacement of an individual particle in a sequence of  $n$  jumps is

$$\mathbf{R} = \sum_{i=1}^n \mathbf{r}_i, \quad (3.15)$$

where  $\mathbf{r}_i$  is the jump vector. Then, the square of the total displacement is

$$\mathbf{R}^2 = \sum_{i=1}^n \mathbf{r}_i^2 + 2 \sum_{i=1}^{n-1} \sum_{j=i+1}^n \mathbf{r}_i \mathbf{r}_j. \quad (3.16)$$

An averaging over an ensemble of particles produces the following:

### 3.2. Diffusion as a Random Walk

$$\langle \mathbf{R}^2 \rangle = \sum_{i=1}^n \langle \mathbf{r}_i^2 \rangle + 2 \sum_{i=1}^{n-1} \sum_{j=i+1}^n \langle \mathbf{r}_i \mathbf{r}_j \rangle. \quad (3.17)$$

The first term on the right hand side of the equation contains only an average of the individual jump lengths. The second term contains averages between jump  $i$  and all subsequent jumps  $j$ .

If we consider a situation when each subsequent jump of a diffusing particle is completely independent of all previous jumps, than the double summation in (3.17) vanishes. This is because in the ensemble for every pair  $\mathbf{r}_i \mathbf{r}_j$  there is another particle with a pair  $\mathbf{r}_i \mathbf{r}_j$  equal and opposite in sign [61]. Such a jump sequence is denoted as a Markov sequence or as an uncorrelated random walk. Thus, in this case Eq. 3.17 reduces to

$$\langle \mathbf{R}^2 \rangle = \sum_{i=1}^n \langle \mathbf{r}_i^2 \rangle. \quad (3.18)$$

This relation can be further modified as in a lattice the jump vectors can take only certain values. Assuming that only nearest-neighbor jumps occur, we obtain

$$\langle \mathbf{R}^2 \rangle = \langle n \rangle d^2, \quad (3.19)$$

with  $\langle n \rangle$  being the average number of jumps of a particle. Now, combining (3.14) and (3.19), we obtain the following expression for the diffusion coefficient:

$$D = \frac{\langle n \rangle d^2}{6t}. \quad (3.20)$$

We can introduce the quantity  $\Gamma$ , which is called the jump rate and is defined as the average number of jumps a particle executes per unit time into one of its  $Z$  neighboring sites, thus

$$\Gamma \equiv \frac{\langle n \rangle}{Zt}. \quad (3.21)$$

Then, we get for the diffusion coefficient of a particle diffusing via a random walk

$$D = \frac{1}{6} d^2 Z \Gamma. \quad (3.22)$$

There are, however, certain types of diffusion mechanisms for which every jump of a diffusing particle is not independent but has a memory about previous jumps. Usually those are the mechanisms where defects serve as a diffusion vehicle, e.g.

vacancy mediated diffusion, which will be discussed in more detail in Section 3.4. The presence of a defect results in a predominance of the reverse direction for the successive jump. As a consequence, the double summation in (3.17) does not vanish. This effect is called the correlation effect and can be accounted for by introducing the correlation factor  $f$  [62] via

$$f \equiv \frac{D}{D_{\text{random}}}, \quad (3.23)$$

where  $D$  stands for the diffusivity from correlated diffusion, while  $D_{\text{random}}$  denotes the hypothetical diffusion coefficient from uncorrelated jump sequences. Using (3.22) we can define an expression for the diffusion coefficient in more general case:

$$D = \frac{1}{6} f d^2 Z \Gamma. \quad (3.24)$$

Herein,  $f = 1$  for uncorrelated diffusion and  $f < 1$  for correlated process. The exact value of the correlation factor depends on the crystal structure and the diffusion mechanism. The calculation of this parameter will be discussed in more detail in Section 3.4.

### 3.3 Diffusion as a Migration Over an Energy Barrier

The theory of random walk considers diffusion as a sequence of many atomic jumps. It is, therefore, important to know at which rates these jumps occur. This can be achieved on a basis of the theory of absolute reaction rates, which originally was formulated for calculating rates of chemical reactions [63]. The theory postulates that the system, moving on a potential energy surface along the reaction coordinates from an initial state to a final state, should overcome some critical configuration at which the probability to reach the final state is certain. This critical configuration is denoted as the activated complex or the transition state and corresponds to a saddle point on the potential energy surface. It is assumed that at any time there is equilibrium between the initial state and the transition state configurations.

Wert and Zener [62, 64] applied this idea to the diffusion of a single atom in a crystal. Consider an atom jumping in a crystalline solid in the  $x$ -direction from the initial state (IS) configuration with the coordinate  $x_0$  to the final state (FS) with the coordinate  $x_1$  through the transition state (TS) configuration with the coordinate  $x'$  (this process is illustrated in Fig. 3.2). Let the jumping atom have three vibrational degrees of freedom in the IS and in the FS. In the TS, it

### 3.3. Diffusion as a Migration Over an Energy Barrier

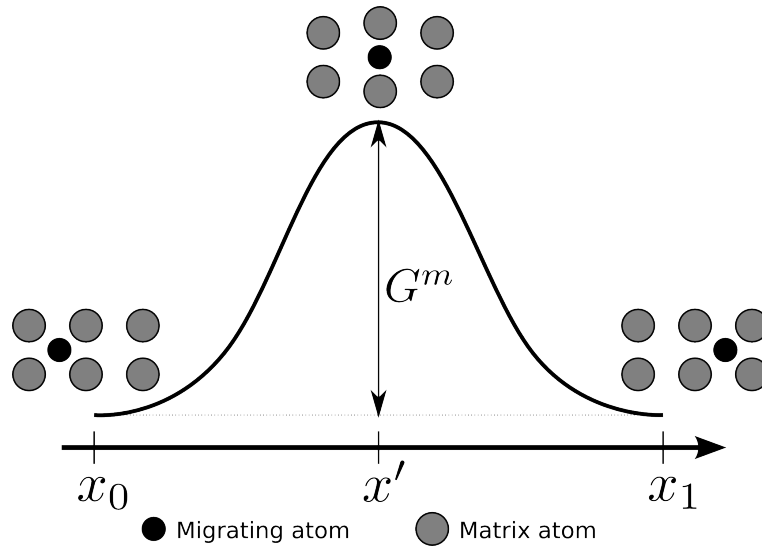


**Figure 3.2:** Atom migration in a crystalline solid from the initial configuration at  $x_0$  to the final configuration at  $x_1$  passing through the transition state configuration at  $x'$ . Circles illustrate the change in atomic configuration during migration while the curve shows the corresponding change in the free energy of the system.

has two vibrational degrees of freedom in the plane perpendicular to the jump direction. The jumping atom interacts with all other atoms in the crystal. Thus, the potential energy of the system  $\phi(x, y, z, q_i)$  depends on the position of the jumping atom  $(x, y, z)$  and the positions of other atoms  $(q_1, q_2, q_3, \dots)$ . In the ensemble of such atoms the jump rate  $w$ , i.e. the total number of jumps per unit time is written as

$$w = \alpha n' \langle v_x \rangle, \quad (3.25)$$

and the jump rate of a single atom is

$$\omega = \frac{w}{n} = \alpha \frac{n'}{n} \langle v_x \rangle. \quad (3.26)$$

Here  $n'$  is the linear density of particles at  $x'$ ;  $n$  is the number of particles in the site about  $x_0$  before the jump;  $\langle v_x \rangle$  is the average velocity of the particles at  $x'$  crossing the barrier from site at  $x_0$  to  $x_1$ ;  $\alpha$  is the transmission coefficient of the barrier ( $\alpha \approx 1$  in the classical case, and  $\alpha > 1$  if the tunneling occurs. Further  $\alpha$  considered to be unity).

According to the Boltzmann distribution the average velocity  $\langle v_x \rangle$  can be calculated in the following way:

Chapter 3. Diffusion in Solids

$$\langle v_x \rangle = \frac{\int_{-\infty}^{\infty} v_x \exp\left(-\frac{mv_x^2}{2k_B T}\right) dv_x}{\int_{-\infty}^{\infty} \exp\left(-\frac{mv_x^2}{2k_B T}\right) dv_x} = \left(\frac{k_B T}{2\pi m}\right)^{1/2}, \quad (3.27)$$

where  $m$  is the mass of the atom.

Since the atoms in the IS and in the TS are in equilibrium, we have

$$\frac{n'}{n} = \frac{P'_{(2)}}{P_{(3)}}, \quad (3.28)$$

where  $P'_{(2)}$  and  $P_{(3)}$  are the partition functions for the particles oscillating in the TS and IS respectively. Note, that subscripts indicate the number of degrees of freedom in these states. In the TS one vibrational degree of freedom is replaced with the translational one.

Assuming that kinetic energies of the particles at  $x_0$  and  $x'$  are equal, only the potential energy  $\phi$  remains in  $P$  giving

$$\frac{n'}{n} = \frac{\int_{-\infty}^{\infty} \dots \int_{-\infty}^{\infty} \exp[-\phi(x', y, z, q_i)/k_B T] dy dz \prod_i dq_i}{\int_{-\infty}^{\infty} \dots \int_{-\infty}^{\infty} \exp[-\phi(x, y, z, q_i)/k_B T] dx dy dz \prod_i dq_i} \quad (3.29)$$

In the harmonic approximation one can expand the function  $\phi(x, y, z, q_i)$  at  $x = x_0$  restricting to the first two terms:

$$\phi(x, y, z, q_i) = \phi(x_0, y, z, q_i) + \frac{K}{2} (x - x_0)^2. \quad (3.30)$$

Here,  $K = \left(\frac{\partial^2 \phi}{\partial x^2}\right)_{x=x_0}$ , and  $\left(\frac{\partial \phi}{\partial x}\right)_{x=x_0} = 0$ .

The integration yields

$$\frac{n'}{n} = \sqrt{\frac{K}{2\pi k_B T}} \frac{P'_{(2)}}{P_{(2)}}. \quad (3.31)$$

Inserting (3.27) and (3.31) into (3.26), and using the expression for the Gibbs free energy

$$G = -k_B T \ln P \quad (3.32)$$

one arrives at the following relation for the jump frequency:

### 3.3. Diffusion as a Migration Over an Energy Barrier

$$\omega = \nu \exp\left(-\frac{\Delta G^m}{k_B T}\right). \quad (3.33)$$

Here  $\nu = \frac{1}{2\pi} \sqrt{\frac{K}{m}}$  is the frequency of small oscillations about  $x_0$ , which is interpreted as the attempt rate.  $\Delta G^m$  is the free energy difference (note that in the following, the  $\Delta$  sign is omitted for convenience) of the particle oscillating in the  $yz$  plane at  $x'$  and  $x_0$  respectively and it is called the migration free energy.

This theory, however, possesses a fundamental restriction. In order for the definitions of the thermodynamic properties of the transition state (its energy, entropy, volume, etc.) to make sense, the transition state has to exist long enough compared to the time of thermal relaxation of the lattice in the region surrounding the saddle point. This means the atom should climb to the energy barrier slow enough such that at every intermediate stage, including the transition state, the system remains in equilibrium.

There are several other assumptions which have been made during the derivation of (3.33): (i) The harmonic approximation is used. This is a general feature of all diffusion calculations. However, it should be noted that at the saddle point the critical displacement amplitude reaches about the half of the whole jump length and, therefore, by far exceeds the harmonic limit; (ii) Quantum effects are ignored. Those are, however, likely to be important at low temperatures or for diffusion of light atoms [65]; (iii) Essentially single atom jumps are considered although the potential  $\phi$  contains the coordinates of all other atoms.

Instead of the model of the isolated atom, Vineyard introduces a strict many-body approach [66]. The approach is very similar to the one by Wert and Zener, however, instead of considering jumps of a particular atom which occurs if the fluctuation of the energy is big enough, all  $N$  atoms of the crystal having  $3N$  vibrational degrees of freedom are considered. He derives the following relation for the jump frequency  $\omega$ :

$$\omega = \nu^* \exp\left(-\frac{E^m}{k_B T}\right), \quad (3.34)$$

where

$$\nu^* = \frac{\prod_{i=1}^{3N} \nu_i}{\prod_{i=1}^{3N-1} \nu'_i}. \quad (3.35)$$

Here,  $E^m$  is the potential energy difference between the system in the TS and in the IS. This is different from the result of Wert and Zener (3.33) in which the

### Chapter 3. Diffusion in Solids

free energy difference has to be used. The quantity  $\nu^*$  defined in Eq. 3.35 is the ratio of the product of  $3N$  normal mode frequencies of the lattice in the IS to the product of  $3N - 1$  normal mode frequencies of the lattice in the saddle point.

It is important to note that in Vineyard's theory no thermodynamic arguments have been applied, like for instance (3.28) and (3.32). Therefore, there is no need to postulate equilibrium during all stages of migration. The transition state which was the highest point on the free energy curve now corresponds to the special atomic configuration in the crystal for which migration leads to the smallest increase of the potential energy. However, for atoms in this special configuration, Vineyard introduced a new set of frequencies  $\nu'$  what led to appearance of  $\nu^*$ . These frequencies are a purely mathematical construct and would not appear in the real crystal since the transition state configuration is unstable. However, they can be calculated using, for instance, first-principles methods.

Equation (3.34) can be written in slightly different form by using the following relations [67]

$$\begin{aligned} \prod_{i=1}^{3N} \nu_i &= \left(\frac{k_B T}{h}\right)^{3N} \exp \left[ \sum_{i=1}^{3N} \ln \left( \frac{h\nu_i}{k_B T} \right) \right], \\ \prod_{i=1}^{3N-1} \nu'_i &= \left(\frac{k_B T}{h}\right)^{3N-1} \exp \left[ \sum_{i=1}^{3N-1} \ln \left( \frac{h\nu'_i}{k_B T} \right) \right]. \end{aligned} \quad (3.36)$$

In the high-temperature limit ( $k_B T \gg h\nu$ ) the vibrational entropy of a harmonic system is given as

$$S = 3Nk_B - k_B \sum_j^{3N} \ln \left( \frac{h\nu_j}{k_B T} \right). \quad (3.37)$$

Thus, (3.36) and (3.37) can be rewritten in the following way

$$\begin{aligned} \prod_{i=1}^N \nu_i &= \left(\frac{k_B T}{h}\right)^{3N} \exp \left( -\frac{S}{k} \right), \\ \prod_{i=1}^N \nu'_i &= \left(\frac{k_B T}{h}\right)^{3N-1} \exp \left( -\frac{S'}{k} \right), \end{aligned} \quad (3.38)$$

where  $S$  and  $S'$  are the vibrational entropies of the IS and the TS respectively. Equation 3.34 now can be written as

$$\omega = \frac{k_B T}{h} \exp \left( -\frac{E^m - TS^m}{k_B T} \right), \quad (3.39)$$

### 3.4. Diffusion Mechanisms and Correlation

where  $S^m = S' - S$  is the entropy of migration. Defining the Gibbs free energy of migration as  $G^m = E^m - TS^m$  the alternative expression for the jump rate becomes

$$\omega = \frac{k_B T}{h} \exp\left(-\frac{G^m}{k_B T}\right). \quad (3.40)$$

Again, it should be noted that here the free energy of migration is not a free energy in the usual sense, since it is related to the special configuration of the system (transition state) having one degree of freedom less than in its normal state. This missing degree of freedom is responsible for the factor  $k_B T/h$  in the formulae for the jump rate.

## 3.4 Diffusion Mechanisms and Correlation

In a crystalline lattice, the atomic positions and therefore the migration paths of atoms are subject to certain restrictions. This allows a simple description of the diffusion process in terms of certain mechanisms. The knowledge of a diffusion mechanism is important for identifying the parameters which enter Eq. (3.24), therefore, for obtaining the diffusion coefficient. Knowledge about the diffusion mechanism is particularly important for describing the correlation effect discussed in Section 3.2 and consequently for determining the correlation factor  $f$ . There are several diffusion mechanisms proposed in the literature, which might occur in solids [56, 61, 65]. Here we consider only two such mechanisms, which are relevant for this work: interstitial diffusion and vacancy mediated diffusion.

### 3.4.1 Interstitial Mechanism

An atom is considered to diffuse via an interstitial mechanism if it jumps from one interstitial site to another nearest-neighbor interstitial site without permanently displacing any surrounding atoms. As can be seen from Figure 3.3, in order to move from one interstitial site to another, one atom should pull apart surrounding atoms. It also requires energy to break bond with neighbors, however, bonding of interstitials to the surrounding atoms is usually weak compared to the atoms at normal lattice sites. Thus, the energy barrier, an interstitial atom has to overcome changing sites, is primarily due to the lattice distortion.

Usually, the fraction of interstitial sites occupied by atoms is very small compared to the empty sites. This implies that all possible directions for the jump of an interstitial atom to adjacent interstitial sites are equally probable and independent of the previous jumps. Thus, the sequence of jumps of the interstitial atom is uncorrelated and consequently the correlation factor equals unity,  $f = 1$ . Also,

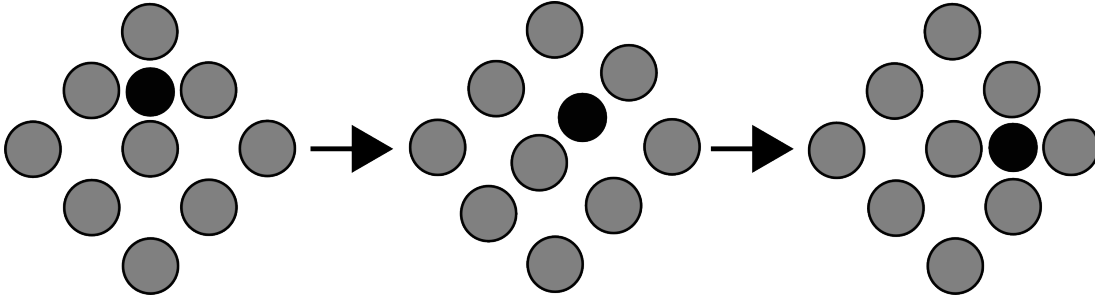


**Figure 3.3:** Schematic illustration of the interstitial diffusion mechanism

since no defects are needed for jumps via this mechanism, the jump rate  $\Gamma$  in Eq. (3.24) is simply determined by (3.40). Therefore, the diffusion coefficient  $D_I$  of an atom diffusing via an interstitial mechanism is obtained as

$$D_I = \frac{k_B T}{h} \frac{Z}{6} d^2 \exp\left(-\frac{G_I^m}{k_B T}\right). \quad (3.41)$$

The interstitial mechanism is known to operate in interstitial alloys with elements of small atomic radius such as boron, carbon or nitrogen (e.g. C in  $\alpha$ - and  $\gamma$ -iron). It may also occur in radiationally damaged substitutional alloys. Highly energetic particles, for instance neutrons, can kick out atoms from their normal lattice sites forming so-called self-interstitials, which are quite mobile once formed.

### 3.4.2 Vacancy Mechanism

Vacancy mechanisms are the dominant mechanisms for self-diffusion and diffusion of substitutional solutes in metals [56]. An atom is said to diffuse via a vacancy-mediated mechanism if it jumps into an adjacent vacant site (Fig. 3.4). Consequently, atoms travel through the crystal via a series of exchange jumps with vacancies, which are occasionally situated in the vicinity.

To jump from one lattice site to another, an atom needs energy to break bond with the neighboring atoms. However, in a close-packed lattice, the distortion caused by the movement of an atom into a vacancy is rather small, thus the energy barrier of migration is comparably low. Nevertheless, diffusion via this mechanism is significantly slower than for the interstitial mechanism. This is due to the limited amount of vacant lattice sites. Hence, each atom must wait an appreciable period of time until a vacancy becomes available. Thus, the jump rate  $\Gamma$  of an atom exchange with a particular neighboring vacant site can be written as

$$\Gamma = \omega_V p. \quad (3.42)$$

### 3.4. Diffusion Mechanisms and Correlation

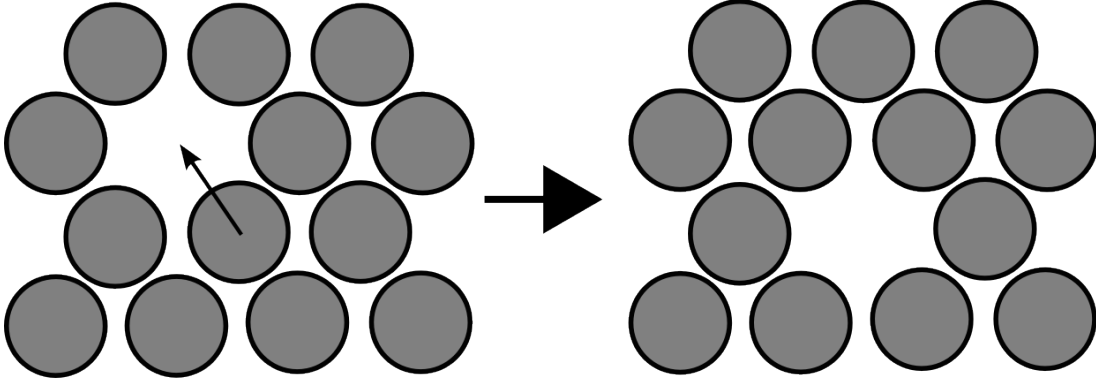


**Figure 3.4:** Schematic illustration of the vacancy diffusion mechanism

Here,  $\omega_V$  denotes the exchange rate between an atom and a vacancy and  $p$  is the probability to find a vacancy on a nearest-neighbor of a diffusing atom. In the case of the self-diffusion,  $p$  is simply the vacancy concentration,  $C_v = \exp(-G_V^f/k_B T)$  [67], with  $G_v^f$  being the vacancy formation free energy. The properties of vacancies are discussed in detail in Chapter 4. The correlation effect for the vacancy mechanism is related to the fact that to perform an exchange with a vacancy an atom must wait for the appearance of a vacancy on one of the adjacent sites. And immediately after the first vacancy-atom exchange jump, the vacancy is available for a reverse jump. Thus, the diffusing atom has a higher probability to go backwards.

In the case of self-diffusion, the correlation factor is a constant number for a given crystal structure. For example, for an fcc lattice  $f = 0.7815$ , for bcc  $f = 0.7272$  (see [68, 69] for details). Thus, the self-diffusion coefficient  $D$  via vacancy mechanism in a cubic lattice has the following form

$$D = \frac{k_B T}{h} f a^2 \exp\left(-\frac{G_0^m}{k_B T}\right) \exp\left(-\frac{G_V^f}{k_B T}\right). \quad (3.43)$$

Here,  $a$  denotes the lattice parameter and  $G_0^m$  is the migration free energy of the atom-vacancy exchange jump.

Next we consider the vacancy-mediated solute diffusion. In this case, the probability  $p$  to find a vacancy at a nearest-neighbor site of a solute atom is different from the one in the pure solvent and can be written as

$$p = C_v \exp\left(-\frac{G^B}{k_B T}\right). \quad (3.44)$$

The difference is due to the interaction between a vacancy and the solute which can be expressed in terms of the Gibbs free energy of binding  $G^B$  (see Chapter 4

Chapter 3. Diffusion in Solids

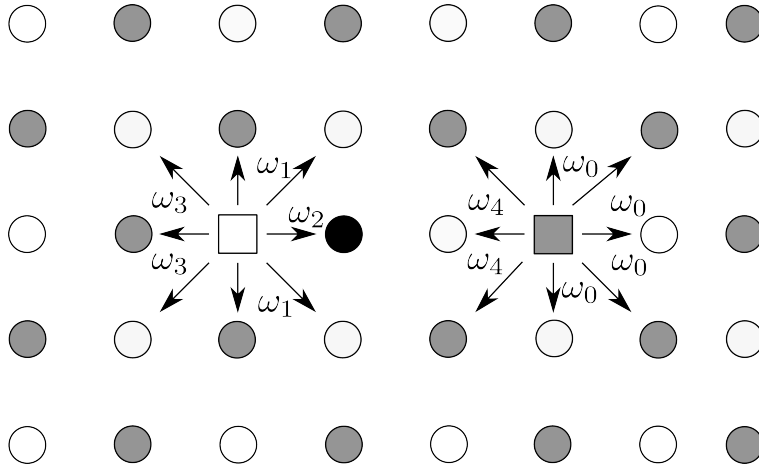


**Figure 3.5:** Schematic representation of the “five-frequency” model in an fcc lattice. Gray and white balls depict the solvent atoms in the different (100) planes, the black ball is the impurity atom and the squares illustrate the vacancies.

for details). If  $G^B$  is negative (positive) the probability  $p$  is enhanced (reduced) compared to diffusion of the solvent atoms.

We consider a dilute fcc alloy for describing the correlation process of the solute diffusion by the vacancy mechanism. To do so, the so-called ‘five-frequency model’ [70–73] is often applied. In a dilute alloy each solute atom can be considered to diffuse in a pure solvent. Within the ‘five-frequency’ model, the interaction of a solute atom with its surroundings is considered up to the first nearest-neighbor distance. This leads to five types of vacancy-atom exchange rates, which are illustrated in Fig. 3.5.

$\omega_2$  corresponds to the rate of the solute-vacancy exchange jump,  $\omega_1$  is the rate of the solvent-vacancy exchange,  $\omega_3$  is the rate of a vacancy-solute pair dissociation and  $\omega_4$  is the rate of the reverse process. All other types of vacancy-solvent jumps are assumed to happen at a rate corresponding to the one in the pure solvent,  $\omega_0$ . Within this formalism Manning [74] derived the expression for the correlation factor  $f_2$  of the solute diffusion:

$$f_2 = \frac{2\omega_1 + 7F\omega_3}{2\omega_2 + 2\omega_1 + 7F\omega_3}. \quad (3.45)$$

$F$  is called the escape probability. It has the following numerical expression in terms of the parameter  $\alpha = \omega_4/\omega_0$ :

$$7F = 7 - \frac{10\alpha^4 + 180.5\alpha^3 + 927\alpha^2 + 1341\alpha}{2\alpha^4 + 40.2\alpha^3 + 254\alpha^2 + 597\alpha + 436}. \quad (3.46)$$

### 3.4. Diffusion Mechanisms and Correlation

It varies between  $\frac{2}{7}$  and 1 when the ratio  $\alpha$  is changed from infinity to zero.

The correlation factor  $f_2$  depends on all vacancy-atom exchange rates. It, therefore, also depends on temperature, unlike the correlation factor  $f$  for the self-diffusion. There are several special cases to be emphasized: (i) If the solute-vacancy exchange is much slower than vacancy-solvent exchanges ( $\omega_2 \ll \omega_1, \omega_3, \dots$ ),  $f_2$  goes to unity. Frequent vacancy-solvent exchanges randomize the vacancy position before the next solute jump. Thus, the solute diffusion turns out to be practically uncorrelated. (ii) In the opposite situation, when the vacancy-solute exchange is much faster than vacancy-solvent exchanges ( $\omega_2 \gg \omega_1, \omega_3, \dots$ ),  $f_2$  goes to zero. Thus, the solute motion is highly correlated. The solute atom bounces back and forth between two neighboring lattice sites. (iii) For a tightly bound solute-vacancy pair, dissociation jumps  $\omega_3$  are highly unlikely. Then, (7.3) simplifies to

$$f_2 \approx \frac{\omega_1}{\omega_2 + \omega_1}. \quad (3.47)$$

In this case the vacancy-solute pair travels as a unit via  $\omega_1$  and  $\omega_2$  jumps.



# Chapter 4

## Point Defects

Point defects affect various important crystal properties. They contribute to the thermal and electrical conductivity, they influence the microstructure and the mechanical properties of metals and they often control the diffusion mechanisms. Lattice vacancies are the predominant defects in simple metals. The concentration of other types of point defects is relatively low in hcp and fcc structures, while interstitials are also important for more open structures, such as bcc and the diamond structure. The theory of point defect concentration arises from purely statistical mechanical considerations, since the Gibbs phase rule postulates that pressure and temperature are sufficient to fix all macroscopic thermodynamic properties of a one-component system [67, 75]. Therefore, statistical mechanics is needed to account for the very existence of point defects. It is convenient to use the constant pressure ensemble for describing defects in crystals since volume is not constant upon introducing point defects. Hence, defect concentration formulae are usually expressed in terms of the Gibbs free energy for which temperature and pressure are the thermodynamic independent variables [67]. Below, we first consider the case of a monoatomic metallic system and assume the concentration of point defects to be so low, such that there is no interaction between them. Further, we treat the case of a dilute substitutional binary alloy and the influence of impurities on defect concentrations.

### 4.1 Vacancies in Pure Metals

Consider an ensemble of  $X$  crystals, all having the same number  $N$  of identical atoms. Each crystal can have any volume  $V_i$  and any number of vacancies  $N_v$  and can exist in any of a set of quantum states with energy  $E_j$ . The probability  $f(N_v, E_j, V_i)$  that a crystal exists in a state with particular values of  $V_i$ ,  $N_v$  and  $E_j$  is given as [67]

## Chapter 4. Point Defects

$$f(N_v, E_j, V_i) = \frac{1}{Z_p} w(N_v) \Omega(N_v, E_j, V_i) e^{-(E_j + PV_i)/k_B T}. \quad (4.1)$$

Here,  $Z_p$  is the partition function, which is connected to the Gibbs free energy of the system through the relation

$$Z_p = e^{-G/k_B T}. \quad (4.2)$$

The term  $w(N_v)\Omega(N_v, E_j, V_i)$  in (4.1) is the degeneracy factor which represents the number of distinct wave functions for a crystal with  $N_v$  vacancies in a state with volume  $V_i$  and energy  $E_j$ . In this factor,  $w(N_v)$  is the configurational statistical count – the number of ways to distribute  $N$  atoms and  $N_v$  vacancies over the lattice sites. It is associated with the configurational entropy  $S_c$  via Boltzmann's formula

$$S_c = k_B \ln w(N_v). \quad (4.3)$$

$\Omega(N_v, E_j, V_i)$  is the degeneracy of the crystal containing  $N_v$  vacancies, except for the configurational contribution. For a given energy and volume,  $\Omega$  depends only on the number of vacancies and not on the configuration of their distribution over the lattice sites. Performing the summation in Eq. 4.1 over all energies and volumes for a given number of vacancies one obtains the probability that the crystal has  $N_v$  vacancies:

$$f(N_v) = \frac{1}{Z_p} w(N_v) \sum_{E_j, V_i} \Omega(N_v, E_j, V_i) e^{-(E_j + PV_i)/k_B T}. \quad (4.4)$$

Here, it is assumed that all lattice sites are equivalent, i.e., there is no dependence of the energy and volume on the distance between vacancies.

Let us introduce the free energy  $G\{N_v\}$  by

$$e^{-G\{N_v\}/k_B T} = \sum_{E_j, V_i} \Omega(N_v, E_j, V_i) e^{-(E_j + PV_i)/k_B T}. \quad (4.5)$$

Then, (4.4) reads as

$$f(N_v) = \frac{1}{Z_p} w(N_v) e^{-G\{N_v\}/k_B T}. \quad (4.6)$$

The free energy defined in (4.5) does not include the configurational entropy term arising from the configurational statistical count  $w(N_v)$ . This fact is identified by braces for the argument of this free energy.

#### 4.1. Vacancies in Pure Metals

Now, we perform summation of (4.6) over all values of  $N_v$  yielding

$$e^{-G/k_B T} = \sum_{N_v} w(N_v) e^{-G\{N_v\}/k_B T}, \quad (4.7)$$

where  $G$  is the total Gibbs free energy of a crystal and  $G\{N_v\}$  is the Gibbs free energy of a crystal containing  $N_v$  vacancies, except for the configurational contribution of the vacancies. While deriving (4.7), we taken into account the fact that the sum of the probabilities is unity,  $\sum_{N_v} f(N_v) = 1$ , and applied the relation (4.2).

The equilibrium value of  $N_v$  is given by the most probable value of (4.6) which is obtained by requiring the following

$$\left[ \frac{\partial \ln f(N_v)}{\partial N_v} \right]_{N_v = \bar{N}_v} = 0. \quad (4.8)$$

Here,  $\bar{N}_v$  is the equilibrium number of vacancies. Then applying (4.8) to (4.4) and using (4.5) one obtains the following relation:

$$\left[ \frac{\partial \ln w(N_v)}{\partial N_v} \right]_{N_v = \bar{N}_v} = \frac{1}{k_B T} \left[ \frac{\partial G\{N_v\}}{\partial N_v} \right]_{N_v = \bar{N}_v}. \quad (4.9)$$

It should be noted that the number of atoms is held fixed while performing the differentiation above. Thus, vacancies can be thought to be formed by moving atoms from the sites inside the lattice to the crystal surface. The right hand side of the equation (4.9) represents the Gibbs free energy increase due to adding one vacancy to the crystal, but does not include the configurational entropy contribution. It is called the free energy of vacancy formation and denoted as  $G_v^f$ :

$$G_v^f = \left( \frac{\partial G\{N_v\}}{\partial N_v} \right)_{N_v = \bar{N}_v}. \quad (4.10)$$

On the left hand side of (4.9), the quantity  $w(N_v)$  represents the number of ways to distribute  $N$  atoms and  $N_v$  vacancies among the  $(N + N_v)$  lattice sites, therefore

$$w(N_v) = \frac{(N + N_v)!}{N! N_v!}. \quad (4.11)$$

Using the formula of Stirling,  $\ln x! \approx x \ln x$ , one can approximate the logarithm of (4.11) as

Chapter 4. Point Defects

$$\ln w(N_v) = (N + N_v) \ln(N + N_v) - N \ln N - N_v \ln N_v, \quad (4.12)$$

from which we can compute the derivative

$$\frac{\partial \ln w(N_v)}{\partial N_v} = \ln \frac{N + N_v}{N_v}. \quad (4.13)$$

Now inserting (4.10) and (4.13) into (4.9) one obtains the expression for the vacancy concentration  $C_v$ :

$$C_v = \frac{\overline{N_v}}{N + \overline{N_v}} = e^{-\frac{G_v^f}{k_B T}}. \quad (4.14)$$

This equation shows that the vacancy concentration increases with temperature via a Boltzmann factor of the free energy of vacancy formation. Since  $G_v^f$  is typically much larger than  $k_B T$ , even close to the melting temperature, the number of vacant sites is much smaller than the number of normal sites and, hence,  $\overline{N_v}$  is often neglected in the denominator of (4.14).

An alternative and somewhat more compact way to obtain (4.14) is to write the total Gibbs free energy of a crystal  $G(N_v)$  containing an arbitrary number of vacancies  $N_v$  as sum of the configurationless Gibbs free energy  $G\{N_v\}$  and the configurational entropy as

$$G(N_v) = G\{N_v\} - k_B T \ln w(N_v). \quad (4.15)$$

Then, the equilibrium concentration of vacancies can be obtained as

$$\frac{\partial G(N_v)}{\partial N_v} = 0. \quad (4.16)$$

In analogy to the previous procedure, the total number of atoms in the crystal is kept constant while performing the derivative, therefore vacancies are assumed to form by transferring atoms from the inside to the surface of the crystal.

Similar to the vacancy concentration, expressions for the concentration of other types of point defects can be obtained, e.g. divacancies, self-interstitials. Generalizing expression (4.15) for the case of a crystal containing various point defects, it can be shown [67] that the concentration  $C_X$  of defects of type  $X$  is

$$C_X = g e^{-\frac{G_X^f}{k_B T}}, \quad (4.17)$$

where  $G_X^f$  is the formation Gibbs free energy of a defect  $X$  and  $g$  is a geometrical factor which accounts for the existence of the number of equivalent configurations of a defect.

## 4.2 Vacancies in Dilute Substitutional Binary Alloy

A binary alloy of atoms A and B is called dilute when the number of atoms B is much smaller than the number of atoms A (not more than a few percent). In this case B is called the solute (or impurity) and A the solvent (or matrix). In a substitutional alloy, atoms A and B as well as vacancies occupy sites of the same lattice.

It is important to note that the vacancy energetics is altered by the presence of a solute atom, i.e. the Gibbs free energy of vacancy formation in an alloy is different from the one in the pure solvent. Considering that the interaction of solute and vacancy is restricted to the first coordination sphere, it is possible to distinguish the Gibbs free energy of vacancy formation in the pure solvent  $G_v^f(A)$  from the one next to a solute atom  $G_v^f(B)$ . If  $G_v^f(A) > G_v^f(B)$ , then there is attractive interaction between the vacancy and the solute, while the interaction is repulsive in the opposite case. We can introduce the Gibbs free energy of binding  $G^b$  as

$$G^B \equiv G_v^f(B) - G_v^f(A). \quad (4.18)$$

Note that hence a negative sign of  $G^b$  indicates attractive solute-vacancy interaction. Then, the total concentration of vacancies in a dilute substitutional binary  $C_v^{tot}$  alloy can be written as [56]

$$C_v^{tot} = e^{-\frac{G_v^f(A)}{k_B T}} \left( 1 - Z C_B + Z C_B e^{-\frac{G^b}{k_B T}} \right). \quad (4.19)$$

Here  $Z$  is the coordination number and  $C_B$  is the solute fraction. The first term in Eq. (4.19) represents the equilibrium vacancy concentration in the pure solvent. The term in parenthesis is larger (smaller) than unity if the interaction between solute and vacancy is attractive (repulsive), and consequently the total vacancy concentration in the alloy is higher (lower) than in the pure solvent. We define the quantity

$$p = C_v \exp\left(-\frac{G^B}{k_B T}\right) \quad (4.20)$$

which expresses the probability that a vacancy can be found in the vicinity of a solute atom. This expression is particularly interesting for studying the vacancy mechanism of solute diffusion.

### 4.3 Point Defects in Non-dilute Alloys

When the number of atoms B is comparable to the number of atoms A, then such a binary alloy  $A_xB_{1-x}$  cannot be considered as a dilute alloy. Therefore, Eq. (4.19) is no longer valid and alternative approach has to be applied for calculating point defect concentrations. The dilute solution model (DSM) [76, 77] can serve as such an approach. It is a grand-canonical method which is based on the statistical-mechanical formalism of low-temperature expansion [78] and allows calculating point defects concentrations as a function of both temperature and the alloy composition.

Let us consider a crystalline compound consisting of  $N$  lattice sites, with  $N_i$  being the number of sites occupied by a chemical species  $i$ .  $N_i$  can be written as a sum  $N_i = \sum_p c_i(p)$  of site-occupation numbers  $c_i(p)$  over lattice sites  $p$ .  $c_i(p)$  is equal to 1 if the lattice site is occupied by species  $i$  and equal to 0 otherwise. We then introduce a thermodynamic potential  $\Omega(\mu_i, T, V, N)$ , where  $T$  is the temperature,  $V$  is the the crystal volume and  $\mu_i$  are the chemical potentials of species  $i$ . The grand canonical potential  $\Omega$  is related to the grand canonical partition function  $Z$ ,

$$\Omega = -k_B T \ln Z, \quad (4.21)$$

where  $Z$  is defined as

$$Z = \sum_{\sigma} \exp \left[ - \left( E^{\sigma} - \sum_i \mu_i N_i^{\sigma} \right) / k_B T \right]. \quad (4.22)$$

Here, the sum is over all possible arrangements  $\sigma$  of atoms over  $N$  lattice sites, and  $E^{\sigma}$  and  $N_i^{\sigma}$  denote the energy and number of sites occupied by species  $i$  for configuration  $\sigma$ . Inserting (4.22) into (4.21) and using a Taylor series expansion for the logarithm, one obtains

$$\begin{aligned} \Omega = & \left( E^0 - \sum_i \mu_i \sum_p c_i^0(p) \right) \\ & - k_B T \sum_p \sum_{\epsilon} \exp \left[ - \left( \delta E^{\epsilon}(p) - \sum_i \mu_i \delta c_i^{\epsilon}(p) \right) / k_B T \right]. \end{aligned} \quad (4.23)$$

In this equation,  $E^0$  and  $c_i^0(p)$ , respectively, denote the energy and composition of species  $i$  at site  $p$  in the ground state configuration. The second term of Eq. (4.23) represents the sum over different possible changes  $\epsilon$  of chemical identity at a given lattice site  $p$ . The variables  $\delta E^{\epsilon}(p)$  and  $\delta c_i^{\epsilon}(p)$ , respectively, are the change in energy and site-composition with respect to the ground state configuration due

### 4.3. Point Defects in Non-dilute Alloys

to the change  $\epsilon$  at site  $p$ . Thus,  $\delta E^\epsilon(p) = E^\sigma - E^0$  for a change at the site  $p$ .  $N_i^\sigma = \sum_p c_i^\sigma(p)$  as given above, and then  $\delta c_i^\epsilon(p) = c_i^\sigma(p) - c_i^0(p)$  for a species  $i$  at the site  $p$ . It is -1 if the species was removed, +1 if added, and 0 if unchanged. So, effectively,  $(\delta E^\epsilon(p) - \sum_i \mu_i \delta c_i^\epsilon(p))$  is the defect formation energy and then the sum runs over all types of defects and all sites to account for the changes upon introducing a defect.

The average concentration of species  $i$  on lattice cite  $p$ ,  $\langle c_i(p) \rangle$ , can be derived from eq. (4.23) as follows:

$$\langle c_i(p) \rangle = - \frac{\partial \Omega}{\partial \mu_i(p)} = c_i^0(p) + \sum_{\epsilon} \delta c_i^\epsilon(p) \exp \left[ - \left( \delta E^\epsilon(p) - \sum_j \mu_j \delta c_j^\epsilon(p) \right) / k_B T \right]. \quad (4.24)$$

This equation expresses the defect concentrations in terms of the chemical potentials. For an alloy with  $n$  chemical species the values of the chemical potentials at a given temperature are fixed by specifying the  $n - 1$  relative compositions  $N_i/N_j$ . It is also required that  $\Omega$  should vanish at zero pressure. From these  $n$  constraints the chemical potentials at a given alloy composition and temperature are determined, thus, the sublattice concentrations of point defects can be computed from Eq. (4.24).

The expressions obtained above are expected to be accurate for dilute concentrations of defects, since only the first-order terms are considered in the expansion of the logarithm when deriving (4.23). For higher concentrations, the terms beyond the first-order must be considered in the expression for the thermodynamic potential  $\Omega$  in order to account for the interaction between defects [79].



## Chapter 5

# A Single-Volume Approach for Vacancy Formation Thermodynamics Calculations

This chapter describes a simplified computational technique of calculating the Gibbs free energy as well as the entropy and enthalpy for vacancy formation. We apply this method in order to obtain the concentration of vacancies as the function of temperature.

The creation of a point defect in the system associated with a volume change. When calculating the properties connected to this defect, e.g. formation energy, the influence of the volume change has to be taken into account. In practice, this means that a number of supercell calculations for systems with vacancy has to be performed in order to find the equilibrium volume separately for the supercell with and without a vacancy. While such calculations can be routinely accomplished with state-of-the-art computers and codes, they may become a serious issue when the effect of temperature needs to be accounted for. Therefore, it would be convenient to develop a formalism in which the vacancy formation volume can be ignored and which allows to use the same equilibrium volume for both supercells with and without a vacancy. In the work presented below, we discuss how dropping the volume dependence in such computations affects the vacancy formation thermodynamics and show the way to restore the true thermodynamic quantities from the single-volume calculations. The results have been published in *Europhysics Letters* and this publication [80] is reproduced below. The header of the article is shown in Fig. 5.1.

### Author contributions

Andrei Ruban originally suggested the idea for this work and also was the author of the initial draft of the manuscript. Sergey Zamulko and Oleg Gorbatov have

## A single-volume approach for vacancy formation thermodynamics calculations

A. S. BOCHKAREV<sup>1,2</sup>, S. O. ZAMULKO<sup>3,4</sup>, O. I. GORBATOV<sup>5,6,7</sup>, S. I. SIDORENKO<sup>3</sup>, P. PUSCHNIG<sup>2</sup>  
and A. V. RUBAN<sup>1,5</sup>

<sup>1</sup> *Materials Center Leoben Forschung GmbH (MCL) - Roseggerstraße 12, A-8700 Leoben, Austria*

<sup>2</sup> *University of Graz, Institute of Physics, NAWI Graz - Universitätsplatz 5, A-8010 Graz, Austria*

<sup>3</sup> *Metal Physics Department, National Technical University of Ukraine "Kyiv Polytechnic Institute" Kyiv 03056, Ukraine*

<sup>4</sup> *Centre for Materials Science and Nanotechnology, University of Oslo - P. O. Box 1048 Blindern, NO-0316 Oslo, Norway*

<sup>5</sup> *Department of Materials Science and Engineering, KTH Royal Institute of Technology SE-100 44 Stockholm, Sweden*

<sup>6</sup> *Institute of Quantum Materials Science - Ekaterinburg 620107, Russia*

<sup>7</sup> *Magnitogorsk State Technical University - Magnitogorsk 455000, Russia*

**Figure 5.1:** Header of the article [80], which was published in Europhysics Letters. It shows the reference, title and all contributing authors with their affiliations. This chapter reproduces this article.

contributed to the discussion and preparation of the manuscript. I have performed and analyzed all calculations and also prepared the figures for this publication. Peter Puschnig has suggested numerous improvements to the manuscript and has made a significant contribution to its content. The final version was developed together with all co-authors.

### Abstract

The vacancy formation Gibbs free energy, enthalpy and entropy in fcc Al, Ag, Pd, Cu, and bcc Mo are determined by first-principles calculations using the quasi-harmonic approximation to account for vibrational contributions. We show that the Gibbs free energy can be determined with sufficient accuracy in a single-volume approach using the fixed equilibrium volume of the defect-free supercell. Although the partial contributions to the Gibbs free energy, namely, the formation enthalpy and entropy exhibit substantial errors when obtained directly in this approach, they can be computed from the Gibbs free energy using the proper thermodynamic relations. Compared to experimental data, the temperature dependence of the vacancy formation Gibbs free energy is accounted for at low temperatures, while it overestimates the measurements at high temperature, which is attributed to the neglect of anharmonic effects.

## 5.1 Introduction

The vacancy formation energy is an important parameter which determines phase and structural transformations in solids at finite temperatures. Being difficult to measure [81–83], it is generally believed that it can be obtained relatively easily by first-principles calculations based on density functional theory (DFT) as has been done in the past in a large number of publications [84–108].

However, there are two major problems in such DFT calculations. First, it is not clear to what extent the inevitable approximations in the exchange-correlation functional affect the results. Even for metallic systems, where effective short-range screening of electrostatic interactions takes place, an accurate account of the large gradient of the electron density near the vacant site may still pose a problem [54, 107, 109–112]. The second problem arises if one wishes to account for the temperature dependence of the vacancy formation energy.

On the one hand, most of the existing phenomenological models, which involve this quantity, assume that the vacancy formation energies and entropies are temperature independent, and, therefore, it is enough to determine the vacancy formation energy only at 0 K. On the other hand, it has been demonstrated in several *ab initio* calculations [90, 103, 104] as well as in a more approximate atomistic modeling [113, 114] that the vacancy formation energy can change dramatically with temperature. For instance, first-principles molecular dynamics (MD) simulations by Smargiassi and Madden [90] showed a decrease of the vacancy formation free energy in Na by a factor of two from 0 K to close to the melting point. In contrast to this finding, Mattsson *et al.* [103] obtained a significant increase of the vacancy formation energy with temperature for Mo in first-principles MD simulations.

A similar increase has been obtained in Ref. [104] for Al, while the more recent calculations by Glensk *et al.* [112] have demonstrated that the overall vacancy formation free energy substantially decreases if anharmonic contributions are taken into consideration, similar to the results by Smargiassi and Madden [90]. In summary, this means that neither the vacancy formation energy nor the vacancy formation entropy can be considered to be temperature independent. The work by Glensk *et al.* [112] also demonstrates that the quasi-harmonic approximation substantially overestimates the vacancy formation free energy at high temperatures. Thus, in order to accurately reproduce the temperature dependence of the vacancy formation energy at high temperatures, one should account for anharmonic vibrations of the atoms next to the vacancy.

In this work, we establish a thermodynamically consistent approach which is based on quasi-harmonic calculations using one fixed equilibrium volume of a defect-free supercell. Being able to eliminate calculations of the equilibrium volume of the defected cell presents an important simplification in the computational

algorithm, which allows one to study the temperature dependence of the vacancy formation energy by more elaborate methods such as *ab initio* molecular dynamics. We demonstrate our method for vacancies in fcc Al, Cu, Ag, Pd, and bcc Mo using PBEsol functional [54], which has been chosen as to minimise the error for the exchange-correlation energy near the vacancy. The numerical results support our single-volume approach. It should be noted that when comparing the so-obtained results to available experimental data, anharmonic effects beyond the quasi-harmonic approximation should be considered.

## 5.2 Thermodynamic Properties of Vacancies

In pure metals, the free energy (per atom) related to the thermally induced vacancies can be defined as follows

$$G_{\text{vac}} = cG_f - TS_{\text{conf}} \equiv c[H_f - TS_f] - TS_{\text{conf}}. \quad (5.1)$$

Here,  $c$  is the concentration of vacancies,  $G_f$  is the vacancy formation free energy associated with a single vacancy,  $H_f$  is the vacancy formation energy (enthalpy),  $S_f$  the vacancy formation entropy, and  $S_{\text{conf}}$  the configurational entropy related to the vacancies. Using the thermodynamic relation

$$\left(\frac{\partial G_{\text{vac}}}{\partial T}\right)_P = -S, \quad (5.2)$$

where  $S = cS_f + S_{\text{conf}}$  is the total entropy of the system related to vacancy formation, assuming no interaction between vacancies one finds

$$c \left[ \frac{\partial H_f}{\partial T} - T \frac{\partial S_f}{\partial T} \right] + \frac{\partial c}{\partial T} \left[ H_f - TS_f - T \frac{\partial S_{\text{conf}}}{\partial c} \right] = 0. \quad (5.3)$$

If both  $H_f$  and  $S_f$  are temperature independent, one immediately finds the concentration of *noninteracting* vacancies using the entropy of an ideal solution,  $S_{\text{conf}} = -k_B[c \ln c + (1 - c) \ln(1 - c)]$ , which is a well-known result:

$$c \approx \exp(S_f/k_B) \exp(-H_f/k_B T). \quad (5.4)$$

In general, the equilibrium concentration of vacancies is obtained from the corresponding minimization of  $G_{\text{vac}}$  at a fixed temperature, which leads to the following equation:

$$c \left[ \frac{\partial H_f}{\partial c} - T \frac{\partial S_f}{\partial c} \right] + \left[ H_f - TS_f - T \frac{\partial S_{\text{conf}}}{\partial c} \right] = 0. \quad (5.5)$$

However, as long as there is no interaction between vacancies, the first term in this equation vanishes and the concentration of vacancies is determined from the

## 5.2. Thermodynamic Properties of Vacancies

last term, which again leads to (5.4). Moreover, since in this case, the last term in (5.5) is zero, the first term in (5.3) should be also zero, and thus the following important relation between the vacancy formation enthalpy and entropy should be satisfied:

$$\frac{\partial H_f}{\partial T} = T \frac{\partial S_f}{\partial T}. \quad (5.6)$$

This means that if the vacancy formation enthalpy is temperature dependent, so should be the formation entropy, and they are connected via Eq. (5.6).

Vacancy formation energy calculations require, in general, finding the equilibrium volume corresponding to the minimum of the Gibbs free energy of systems (supercells) without and with a vacancy denoted as  $G_0$  and  $G_v$ , respectively. The difference in equilibrium volumes of those supercells with and without and with a vacancy,  $\Omega_0(T)$  and  $\Omega_v(c, T)$ , (normalized by the number of sites) is related to the vacancy formation volume,  $\omega_f$ :

$$\omega_f(T) = \frac{\partial \Omega_v(c, T)}{\partial c}. \quad (5.7)$$

Here, we have neglected the concentration dependence of  $\omega_f$ , which should be insignificant. So, the equilibrium volume of the system with vacancies can be written as

$$\Omega_v(c, T) = \Omega_0(T) + c\omega_f(T). \quad (5.8)$$

In practical applications, however, it would be computationally advantageous to determine the thermodynamic properties of vacancies without the need of finding the equilibrium volume of the supercell with vacancy. In such an approach, one performs all supercell calculations, both, with and without a vacancy for the equilibrium volume of the defect-free system. We refer to this approximation as the single-volume approach. The validity of this simplification arises from the fact that the difference in the equilibrium volume of two systems is usually small. As a consequence, the free energies of the systems with and without a defect exhibit small variations as a function of volume due to the fact that their first derivatives are zero at the equilibrium volume.

This approach can be particularly useful in calculations of the self- or substitutional impurity diffusion coefficients at a certain temperature. Although the directly calculated vacancy formation entropy and enthalpy can be in error in this approach, they still obey relations (5.2) and (5.6). Below we demonstrate this approach in calculations of the vacancy formation free energy, enthalpy and entropy for five metals: Al, Ag, Cu, Mo and Pd. The following notations are used. Quantities corresponding to calculations in which the equilibrium volumes  $\Omega_0(T)$  and  $\Omega_v(c, T)$  are explicitly taken into account are denoted as  $G$ ,  $S$ ,  $H$ . Those numerical results in which a single volume  $\Omega_0(T)$  has been used for both supercells, without and with vacancy, are abbreviated as  $\tilde{G}$ ,  $\tilde{S}$ , and  $\tilde{H}$ , respectively.

### 5.3 Computational Details

In this work, the vacancy formation free energy  $G_f(T)$ , is obtained as a sum of three different contributions:

$$G_f(T) = H_f(T) + G_f^{el}(T) + G_f^{vib}(T). \quad (5.9)$$

Here,  $H_f(T)$  is the vacancy formation energy (we consider the case of zero pressure) at the corresponding temperature  $T$ .  $G_f^{vib}(T)$  and  $G_f^{el}(T)$  are the contributions to the vacancy formation free energy from lattice vibrations and thermal one-electron excitations, respectively. In particular, the vacancy formation energy,  $H_f$ , is obtained as

$$H_f(T) = E_v(T) - \frac{N-1}{N}E_0(T), \quad (5.10)$$

where  $E_v(T)$  and  $E_0(T)$  are the total energies of the supercells with and without vacancy, respectively, and  $N$  is the number of atoms in the supercell without vacancy.

The contribution from the thermal one-electron excitations to the total energy,  $E_{el}$ , and free energy,  $G_{el}$ , has been determined as

$$E_{el}(T) = \frac{\pi^2}{3}N(E_F)k_B^2T^2 \quad (5.11)$$

$$G_{el}(T) = -\frac{\pi^2}{3}N(E_F)k_B^2T^2, \quad (5.12)$$

where  $N(E_F)$  is the density of states at the Fermi energy,  $E_F$ , per supercell. We have neglected this contribution for Al, Cu and Ag due to its insignificant contribution to the total free energy of vacancy formation in these cases.

All *ab initio* calculations in this paper are performed by the frozen-core full-potential projector augmented wave (PAW) method [115, 116] as implemented in the Vienna *ab initio* simulation package (VASP) [117–119]. The PBEsol generalized gradient approximation [54] has been utilized, which minimizes the error for open systems like surfaces and vacancies. Besides, this functional reproduces quite well the lattice constants of 4d metals (Ag, Pd, Mo), which is important for description of the first-principles thermodynamics of defect properties.

The size of the supercell for fcc Al, Ag, Cu and Pd was  $2 \times 2 \times 2 (\times 4)$  containing 32 atoms in the defect-free cell, and for bcc Mo the size of the supercell used was  $3 \times 3 \times 3 (\times 2)$  containing 54 atoms in the defect-free supercell. We have checked the convergence of the vacancy formation energy in the case of copper with respect to the supercell size and found that the difference between the 0 K vacancy formation energies for supercells containing 32 and 108 atoms was less than 0.01 eV. Therefore, we conclude that the size of the supercell used in the present

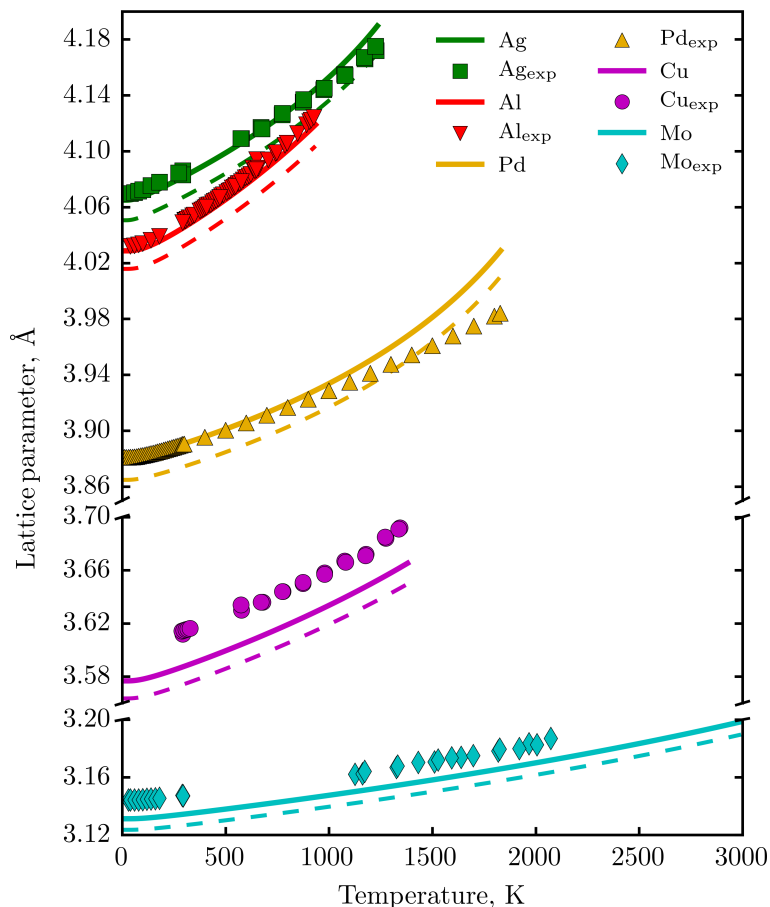


**Figure 5.2:** (Color online) Calculated equilibrium lattice parameters of Ag, Al, Pd, Cu, and Mo obtained in the quasi-harmonic approximation as a function of temperature (full lines) compared to the experimental data (symbols) for Al [121–123], Ag [123, 124], Cu [124, 125], Pd [126], Mo [123, 127, 128]. Dashed lines show the equilibrium lattice parameters obtained for supercells with vacancy.

study is sufficient for obtaining reasonably accurate vacancy formation energies. All atoms were allowed to relax during calculations of the defected supercells. The plane wave energy cutoff was 500 eV. The integration over the Brillouin zone has been done using a  $10 \times 10 \times 10$  grid of the Monkhorst-Pack (MP) mesh [120] in the case of Cu, Pd, Mo,  $12 \times 12 \times 12$  in the case of Al and  $14 \times 14 \times 14$  for Ag. The convergence tolerance for the total energy was  $10^{-8}$  eV/atom, while  $10^{-3}$  eV/Å for forces on atoms during local lattice relaxations.

The free energy of lattice vibrations is calculated in the quasi-harmonic approximation using the phonopy code [129] where the dynamical matrix has been obtained by the small displacement method [130]. The unit cell was taken to be identical to the supercell while calculating phonon dispersion. Symmetry was

considered while performing displacements reducing the number of displacements to one for defectless supercells and to 7 and 13 for supercells with a vacancy in the case of fcc and bcc materials respectively. The amplitude of displacements was 0.005 Å in the case of Al and 0.01 Å for the other metals. The linear dependence of the force with respect to the displacement amplitude was checked in the case of Cu. The linear regime preserves at least up to displacements of 0.07 Å.

## 5.4 Results

As a first step, we have calculated the temperature dependence of the equilibrium lattice parameters of the five investigated metals for the defect-free supercells within the quasi-harmonic approximation. As can be seen from Fig. 5.2, the calculated lattice parameters for Al, Ag and Pd are in very good agreement with the experimental data, especially at low temperatures. Somewhat worse agreement is observed for Cu and Mo which is attributed to a deficiency of PBEsol for these elements. Nevertheless, the character of the temperature dependence is still well described within the quasi-harmonic *ab initio* calculations. We have also performed quasi-harmonic calculations for supercells with a vacancy in order to find the respective equilibrium volumes. The obtained data is shown in Fig. 5.2 as dashed lines.

Based on these results, we are able to compute all thermodynamic properties describing the vacancy formation as a function of temperature. We illustrate the effectiveness of the single-volume approach in Fig. 5.3 using Al as an example. Here, we show the properly calculated values of the vacancy thermodynamic properties,  $G$ ,  $S$  and  $H$  for Al, obtained in calculations with the corresponding equilibrium volumes together with their counterparts,  $\tilde{G}$ ,  $\tilde{S}$ ,  $\tilde{H}$  obtained for the single equilibrium volume of the defect-free supercells. First of all, one can see that  $G$  and  $\tilde{G}$  are very close to each other. This is to be expected since the variation of the free energy of the supercells is small close to their equilibrium volume. Moreover, the close agreement of  $G$  and  $\tilde{G}$  provides the basis for using the thermodynamic relation (5.2) in order to determine formation enthalpies and entropies. The resulting entropy and enthalpy terms are shown in panels (b) and (c) of Fig. 5.3 and are denoted as  $S'$  and  $H'$ , respectively.

One can see that  $S'$  and  $H'$  are very close to the directly calculated values,  $S$  and  $H$ . On the other hand, the difference between  $S$  and  $\tilde{S}$  as well as between  $H$  and  $\tilde{H}$  is significant. This implies that using the entropy and enthalpy of vacancy formation directly obtained for a single-volume of both supercells, one introduces a substantial error. It is interesting that the huge errors in  $\tilde{S}$  and  $\tilde{H}$  compensate each other and produce accurate result for the Gibbs free energy when summed up.

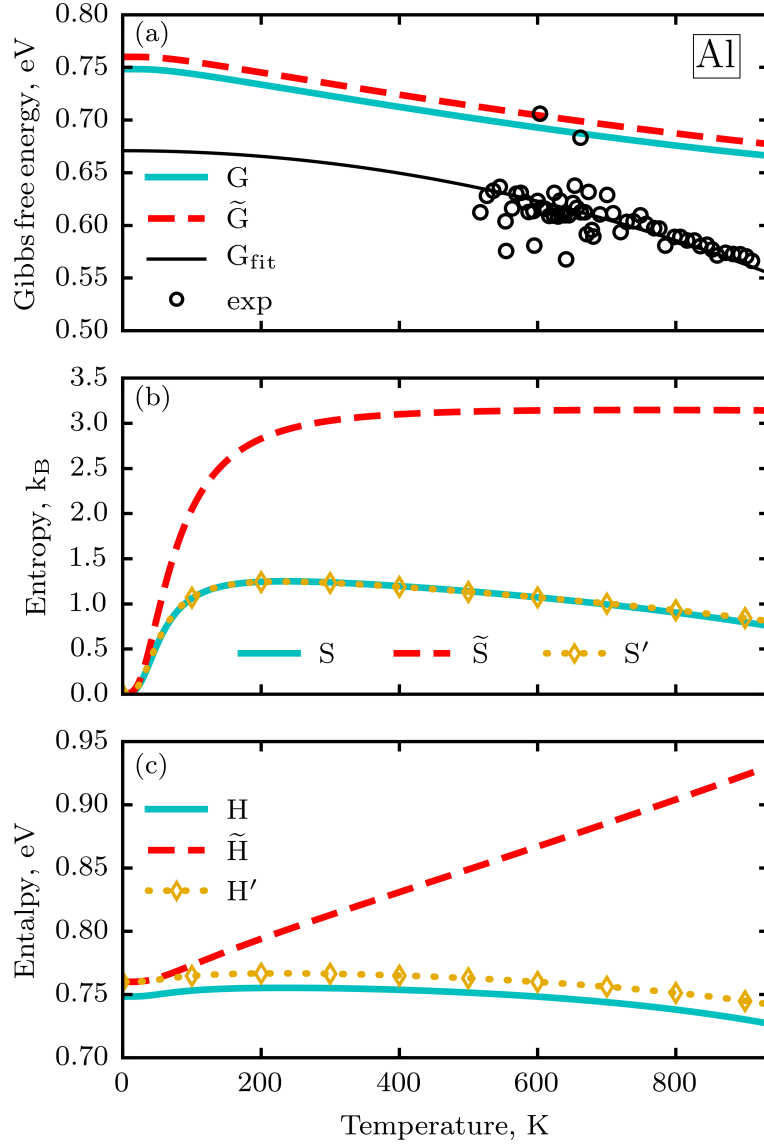


**Figure 5.3:** (Color online) (a) The vacancy formation Gibbs free energy, (b) vacancy formation entropy and (c) vacancy formation enthalpy in Al.  $G$ ,  $S$ ,  $H$  correspond to the calculations done at the equilibrium volumes of supercells with and they are plotted by solid lines.  $\tilde{G}$ ,  $\tilde{S}$ ,  $\tilde{H}$  are the vacancy formation free energy, enthalpy and entropy determined in the single-volume approach and plotted by dashed lines with diamonds. The vacancy formation entropy,  $S'$ , and enthalpy,  $H'$ , are obtained from  $\tilde{G}$  using relation (5.2). Black dots show available experimental data [131].  $G_{\text{fit}}$  is the quadratic fit of the experimental temperature dependent vacancy formation free energy shown by black solid line.

## Chapter 5. A Single-Volume Approach for Vacancy Formation Thermodynamics Calculations

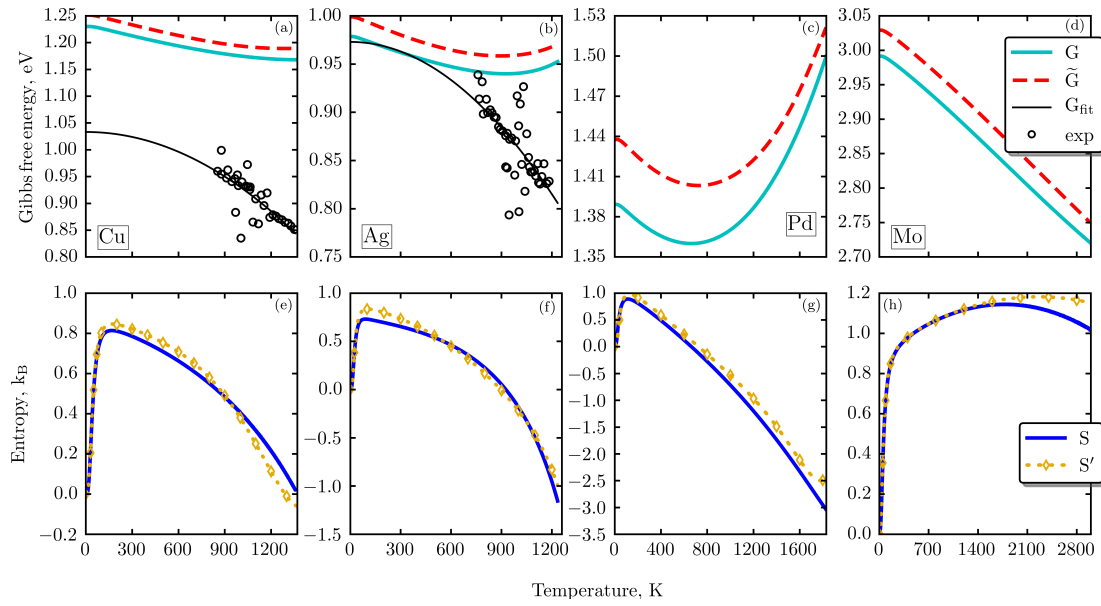


**Figure 5.4:** (Color online) (a,b,c,d) The vacancy formation Gibbs free energy; (e,f,g,h) the vacancy formation entropy in Cu, Ag, Pd and Mo, respectively. For notations see Fig 5.3.

In Fig. 5.4, we show analogous results for four other metals: fcc Cu, Ag, and Pd as well as for bcc Mo. Overall, the differences between the numerical values for  $G$  and  $\tilde{G}$  are reasonable small. In the case of Cu, it is negligible, while it is somewhat larger in the case of Ag, and is about 0.04–0.05 eV for Mo and Pd. However, it is mostly a constant shift. Moreover, the energy differences can be regarded as minor when taking into consideration typical errors related to various approximations for the exchange-correlation potential. At the same time, the agreement of formation entropies,  $S$  and  $S'$ , is very good in all the cases showing that the single-volume approach is reasonably accurate for different metals. Regarding the temperature dependence of  $G$ , we notice a pronounced influence of the electronic free energy for Pd and Mo. In the case of Pd,  $G$  first decreases and then rises with the temperature, for Mo the decrease of  $G$  is much more pronounced than for all other metals. This is because a vacant site differently affects the density of states at the Fermi energy in these metals, increasing it in Mo and decreasing in Pd, leading according to (5.11) to the respectively negative and positive contributions to the vacancy formation free energy.

Figs. 5.3 and 5.4 also include available experimental data [131] obtained by a conversion of the experimental vacancy concentrations to the vacancy formation free energies. In all the cases considered here, the experimental formation energies are smaller than the corresponding theoretical results. One obvious problem with

such a comparison is the fact that experimental data are available only for rather high temperatures, while the theoretical results obtained in the quasiharmonic approximation are expected to be accurate for low temperatures. Indeed, the experimentally observed character of the temperature dependence of the vacancy formation free energy at high temperatures can most probably be attributed to anharmonic effects as discussed in detail by Glensk *et al.* [112].

Using a quadratic fit as proposed in that work [112], one can get a qualitative picture of the expected temperature dependence of the vacancy formation free energy in the real systems,  $G_{\text{fit}}$ . Such fits to the experimental data are shown in Fig. 5.3 and 5.4, respectively, as the black lines. As one can see, in the case of Al and Ag, quasi-harmonic PBEsol calculations provide a very good description of the vacancy formation free energy at lower temperatures, while for Cu, the calculations considerably overestimate the low-temperature extrapolation of experimental data by about 0.2 eV. We note that Glensk *et al.* [112] have found similar result for Cu when using the local density approximation (LDA) or the AM05 [109, 110] exchange-correlation functional. Since the latter produces results very close to the PBEsol functional used in this work, our large error for Cu could be attributed to the failure of PBEsol in this particular case. However, we think that the most possible source of discrepancy is the PBEsol error for the equilibrium lattice parameter of Cu, which effectively leads to overbinding and, as a consequence, to the large values of the vacancy formation energy. In the case of Ag and Al, the PBEsol error for lattice constant is very small, and the low temperature vacancy formation free energy in reasonable agreement with the extrapolated experimental data.

## 5.5 Summary

The quasi-harmonic approximation provides an accurate thermodynamic framework for vacancy formation calculations. We demonstrate that a single-volume approach can be applied for the calculations of thermodynamic properties of vacancies. In this case, however, the enthalpy and entropy should be calculated from the Gibbs free energy using proper thermodynamic relations. These insight can be used in order to simplify the description of thermodynamic properties of defects including vacancies. At temperatures close to the melting point, the inclusion of anharmonic effects due to vibrations of the vacancy should be considered.

### Acknowledgments

Financial support by the Austrian Federal Government (in particular from Bundesministerium für Verkehr, Innovation und Technologie and Bundesministerium

## Chapter 5. A Single-Volume Approach for Vacancy Formation Thermodynamics Calculations

für Wissenschaft, Forschung und Wirtschaft) represented by Österreichische Forschungsförderungsgesellschaft mbH and the Styrian and the Tyrolean Provincial Government, represented by Steirische Wirtschaftsförderungsgesellschaft mbH and Standortagentur Tirol, within the framework of the COMET Funding Programme is gratefully acknowledged. This work is partially supported by Ministry of Education and Science of Ukraine (Grant №2811f). S.O.Z. thanks the Swedish Institute (SI) for providing a scholarship for his research at the Royal Institute of Technology (KTH). AVR acknowledges the support of the Swedish Research Council (VR project 2015-05538), the European Research Council grant, the VINNEX center Hero-m, financed by the Swedish Governmental Agency for Innovation Systems (VINNOVA), Swedish industry, and the Royal Institute of Technology (KTH). Calculations have been done using NSC (Linköping) and PDC (Stockholm) resources provided by the Swedish National Infrastructure for Computing (SNIC).

## Chapter 6

# Cu Diffusion in Single-crystal and Polycrystalline TiN Barrier Layers: A High-Resolution Experimental Study Supported by First-principles Calculations

In this chapter, we study the diffusion properties of TiN, where the the chapter essentially consists of two parts. The first and the main part is devoted to the experimental preparation of the high quality TiN films and to the testing of their performance against Cu diffusion. Two types of the films were studied, namely a single-crystalline and a polycrystalline TiN. The second part of the chapter presents the *ab initio* study of Cu impurity diffusion mechanisms in the single-crystal TiN. Here, we study several diffusion mechanisms by calculating respective migration barriers for Cu diffusion. The influence of the stoichiometry of TiN is considered and for certain compositions, N-deficient or perfectly stoichiometric TiN, the activation energies for diffusion are estimated. Note that the effect of temperature was included only via the thermal lattice expansion for which the data was taken from experiment [132]. The work has been published in the Journal of Applied Physics. This publication [133] is reproduced here and its header is shown in Fig. 6.1.

### Author contributions

The experimental work has been done by Marlene Mühlbacher and co-workers in the group of Christian Mitterer at the Montanuniversität Leoben and in the group of Lars Hultman at Linköping University. Marlene Mühlbacher has written



**Cu diffusion in single-crystal and polycrystalline TiN barrier layers: A high-resolution experimental study supported by first-principles calculations**

Marlene Mühlbacher,<sup>1,2,a)</sup> Anton S. Bochkarev,<sup>3,4</sup> Francisca Mendez-Martin,<sup>1</sup> Bernhard Sartory,<sup>3</sup> Livia Chitu,<sup>3</sup> Maxim N. Popov,<sup>3</sup> Peter Puschnig,<sup>4</sup> Jürgen Spitaler,<sup>3</sup> Hong Ding,<sup>5</sup> Nina Schalk,<sup>1</sup> Jun Lu,<sup>2</sup> Lars Hultman,<sup>2</sup> and Christian Mitterer<sup>1</sup>

<sup>1</sup>Department of Physical Metallurgy and Materials Testing, Montanuniversität Leoben, Franz-Josef-Strasse 18, A-8700 Leoben, Austria

<sup>2</sup>Thin Film Physics Division, Department of Physics, Chemistry and Biology (IFM), Linköping University, S-581 83 Linköping, Sweden

<sup>3</sup>Materials Center Leoben Forschung GmbH, Roseggerstrasse 12, A-8700 Leoben, Austria

<sup>4</sup>Institute of Physics, University of Graz, NAWI Graz, Universitätsplatz 5, A-8010 Graz, Austria

<sup>5</sup>Environmental Energy Technologies Division, Lawrence Berkeley National Laboratory, Cyclotron Road 1, Berkeley, California 94720, USA

**Figure 6.1:** Header of the article [133], which was published in the Journal of Applied Physics. It shows the reference, title and all contributing authors with their affiliations. This chapter reproduces this article.

the part of the manuscript related to the experiments and also prepared all the figures for the publication. Planning of the theoretical part has been done mostly by me, Maxim Popov, and Peter Puschnig. I have performed all the DFT calculations in this work and have also written a major part of the theoretical section. The dilute solution model code and expertise on this method was kindly provided by Hong Ding. The results and the structure of the manuscript have been discussed by all authors of the manuscript.

## Abstract

Dense single-crystal and polycrystalline TiN/Cu stacks were prepared by unbalanced DC magnetron sputter deposition at a substrate temperature of 700°C and a pulsed bias potential of -100 V. The microstructural variation was achieved by using two different substrate materials, MgO(001) and thermally oxidized Si(001), respectively. Subsequently, the stacks were subjected to isothermal annealing treatments at 900°C for 1 h in high vacuum to induce the diffusion of Cu into the TiN. The performance of the TiN diffusion barrier layers was evaluated by cross-sectional transmission electron microscopy in combination with energy-dispersive X-ray spectrometry mapping and atom probe tomography. No Cu penetration was evident in the single-crystal stack up to annealing temperatures of 900°C, due to the low density of line and planar defects in single-crystal TiN. However, at higher annealing temperatures when diffusion becomes more prominent, density-functional theory calculations predict a stoichiometry-dependent atomic diffusion mechanism of Cu in bulk TiN, with Cu diffusing on the N sublattice for the experimental N/Ti ratio. In comparison, localized diffusion of Cu along grain boundaries in the columnar polycrystalline TiN barriers was detected

after the annealing treatment. The maximum observed diffusion length was approximately 30nm, yielding a grain boundary diffusion coefficient of the order of  $1016\text{cm}^2\text{s}^{-1}$  at  $900^\circ\text{C}$ . This is 10 to 100 times less than for comparable underdense polycrystalline TiN coatings deposited without external substrate heating or bias potential. The combined numerical and experimental approach presented in this paper enables the contrasting juxtaposition of diffusion phenomena and mechanisms in two TiN coatings, which differ from each other only in the presence of grain boundaries.

## 6.1 Introduction

Since its implementation in the 1970s, TiN has become one of the commercially most successful thin film materials [9, 134]. Its applications range from hard protective films [135], decorative purposes [136], and coatings on medical implants [137], to diffusion barriers in microelectronics [138]. Such barrier layers are employed to separate the conducting Cu or Al metallization from the Si substrate and surrounding dielectric materials in integrated circuits. Refractory transition metal nitrides in general and TiN in particular are well suited as diffusion barrier materials, due to their high melting points, high thermal stability and good electrical conductivity [28]. Numerous studies are available concerning the barrier performance of TiN and putting forward ways of improving its efficiency. One of the earliest investigations by Chamberlain [25] showed that interdiffusion between r.f. sputtered polycrystalline Cu and TiN layers at temperatures up to  $600\text{-}700^\circ\text{C}$  was very limited and presumably occurring via grain boundary or dislocation mechanisms. As a consequence, a widely applied approach to improve the TiN barrier performance is densification by rapid thermal processing or a plasma treatment in  $\text{NH}_3$  atmosphere [14, 15, 23], or by facilitating the formation of Al-oxides to stuff grain boundaries [19, 21, 139, 140]. However, the second effect is limited to Al metallization, since the formation of Cu-oxides at the TiN grain boundaries is thermodynamically not favorable [11, 19]. A more promising strategy for Cu metallization might therefore be to tune the microstructure of the TiN barrier layer by adjusting the deposition parameters [11]. For example, Gupta et al. [141] grew TiN layers with different microstructures by varying the substrate temperature TS in a pulsed laser deposition process. Temperatures around  $600^\circ\text{C}$  led to domain matching epitaxial growth of TiN on Si(100), while lower substrate temperatures resulted in polycrystalline ( $\text{TS} \sim 450^\circ\text{C}$ ) and nanocrystalline ( $\text{TS} \sim 25^\circ\text{C}$ ) TiN films. Polycrystalline barriers were least resistant against Cu diffusion, with the boundaries between columnar grains providing direct diffusion paths. In the highly textured epitaxial TiN films, the Cu diffusion presumably occurred along low angle grain boundaries. Additionally, the TiN-Si interface with its high dislocation density could have acted as a segregation sink for Cu atoms. Nanocrystalline TiN performed best, which was attributed to the

## Chapter 6. Cu Diffusion in Single-crystal and Polycrystalline TiN Barrier Layers: A High-Resolution Experimental Study Supported by First-principles Calculations

effectively much longer diffusion paths along grain boundaries between nanosized, equiaxial grains. The diffusivity of Cu in TiN could also be influenced by the relative orientation of adjacent grains, as proposed by Moriyama et al. [27], who found that in fiber structured TiN layers the Cu diffusivity decreased with decreasing the mosaic spread angle of the grains by depositing at higher substrate temperatures. However, it has to be considered that a variation in the deposition temperature will not only lead to the formation of different microstructures, but will also influence the overall film density. In general, deposition at higher temperatures results in the growth of denser films, due to enhanced surface diffusion of ad-atoms to equilibrium sites, promotion of island coalescence and stimulated desorption of impurities [142]. The application of a negative bias potential to the substrate has similar effects. Bombardment of the growing film with energetic particles will lead to the elimination of interfacial voids and subsurface porosity, and therefore increases film density [143]. Studies by Lee et al. [20] showed that for TiN films of comparable stoichiometry and microstructure, the film density was the decisive factor determining the failure temperature of the barrier. An evaluation of Cu diffusion in TiN films of different microstructures should therefore ideally be carried out by studying barrier layers grown at the same substrate temperature and with the same bias voltage, to ensure comparable conditions during film formation and growth.

In the present paper, we compare the diffusion of Cu in single- and polycrystalline TiN barrier layers deposited at a substrate temperature of 700°C under a bias voltage of -100 V, sufficient to obtain dense films. The microstructural variation is achieved by using different substrate materials. Single-crystal (001)-oriented TiN can be readily grown on MgO(001), since both materials have the same crystal structure and a lattice mismatch of only -0.7 % [144–147]. Similarly, the growth of columnar polycrystalline TiN on Si and SiO<sub>2</sub> is widely reported [9, 148, 149]. Pristine and annealed TiN/Cu stacks are investigated by high-resolution transmission electron microscopy (TEM) techniques and atom probe tomography (APT). TEM is used to gain insight into the microstructures of the TiN layers, while APT provides three-dimensional maps of the chemical composition in the interface and diffusion regions. Additionally, possible atomic Cu diffusion mechanisms in the single-crystal TiN barrier are examined by density-functional theory (DFT) calculations.

This combined approach of state-of-the-art experimental techniques and first-principles calculations allows us to draw a direct comparison between diffusion of Cu in films with different microstructures but deposited under the same conditions. It is thus possible to pinpoint diffusion phenomena and mechanisms in the bulk (supported by DFT calculations) as well as along distinct grain boundaries (by site-specific APT measurements) in a technologically relevant material for diffusion barriers.

## 6.2 Experimental and Computational Details

TiN/Cu bilayer stacks were deposited in a laboratory-scale magnetron sputtering system on polished single-crystal (001)-oriented MgO substrates ( $10 \times 10 \times 0.5$  mm<sup>3</sup>) and polished (001)-oriented Si wafers ( $20 \times 6 \times 0.5$  mm<sup>3</sup>) with a 5 nm thick thermal SiO<sub>2</sub> layer. This amorphous SiO<sub>2</sub> layer prevented the diffusion of Si from the substrate into the TiN layer at elevated temperatures during the deposition process. The substrates were cleaned by successive rinses in ultrasonic baths of acetone and ethanol before being mounted on a rotating substrate holder in the deposition chamber, which has a base pressure below 105mbar. The deposition system was equipped with three independent magnetron sputtering sources. The target-to-substrate distance was 80mm and the targets were tilted at an angle of 13° with respect to the substrate normal. All targets were sputter-cleaned in pure Ar for 5 min, with a shutter shielding the substrates. Additionally, the substrates were etched for 5min in an Ar plasma immediately prior to deposition by applying a bias voltage of 500V to activate and clean the surface.

TiN layers were grown reactively in mixed Ar/N<sub>2</sub> atmosphere (35 sccm Ar, 5 sccm N<sub>2</sub>) at a substrate temperature of 700°C and a pressure of  $4.5 \times 10^{-3}$  mbar. During deposition, two 2 inch diameter Ti (99.995 % pure) targets were operated in magnetically unbalanced direct current mode with a power density of 6.2 W cm<sup>-2</sup>. Using these conditions, a deposition rate of 11 nm min<sup>-1</sup> was achieved for TiN grown onto substrates at an asymmetrically pulsed bias potential of -100 V. Subsequently, the samples cooled down for 1h inside the vacuum chamber until a substrate temperature of 50°C was reached. To remove possible impurities that might have adsorbed during this cooling step, the TiN surface was cleaned again for 1 min by Ar ion etching with a bias voltage of -500 V. The Cu toplayer was then deposited in a pure Ar discharge at a pressure of  $4.6 \times 10^{-3}$  mbar. The power density at the single 2 inch diameter Cu (99.99 % pure) target operated in magnetically unbalanced direct current mode was set to 2.1 W cm<sup>-2</sup>. The Cu deposition was carried out at floating potential with a film growth rate of 13 nm min<sup>-1</sup>.

Two batches of TiN/Cu stacks with different layer thicknesses were studied: TiN (100 nm) / Cu (130 nm) and TiN (180 nm) / Cu (130 nm). To obtain distinct diffusion profiles of Cu in TiN, the samples with the thicker TiN layer were subjected to isothermal annealing treatments at 900°C for 1h in a vacuum furnace at a pressure below 10<sup>-6</sup> mbar. The annealing program comprised a ramp-up step with a heating rate of 30 K/min, an isothermal annealing step lasting 1 h, and a cooling step at a system dependent cooling rate.

Crystal structures of the pristine samples were characterized by X-ray diffraction (XRD) measurements with a Bruker-AXS D8 Advance diffractometer. The used Cu-K radiation was parallelized in a Goebbel mirror and recorded with an energy-dispersive SolX detector with a 0.12° slit via scans in BraggBrentano and grazing

## Chapter 6. Cu Diffusion in Single-crystal and Polycrystalline TiN Barrier Layers: A High-Resolution Experimental Study Supported by First-principles Calculations

incidence ( $2^\circ$  incidence angle) mode. The density of the deposited TiN films was determined by X-ray reflectivity (XRR) measurements in a Rigaku SmartLab 5-axis diffractometer equipped with Cu-K $\alpha$  radiation, a parabolic multilayer mirror in the primary beam and a secondary graphite monochromator. For the fitting of the measured data, the Leptos Bruker software was used. Values for the density and surface roughness of the TiN layer were obtained by fitting the critical angle and the intensity slope according to the NevotCroce interface model with a genetic algorithm fit [150, 151].

To investigate the TiN/Cu interface region in pristine and annealed samples with APT and cross-sectional TEM, samples were prepared site-specifically [152] using a Zeiss Auriga SMT scanning electron microscope equipped with an Orsay Physics Cobra Z-05 focused ion beam (FIB) unit with Ga $^+$  ion source. All samples were fine-polished with a 5 kV Ga $^+$  beam to remove surface defects due to Ga $^+$  implantation before further analysis.

The microstructural and analytical TEM investigations were performed with a FEI Tecnai G $^2$  TF20 UT TEM equipped with a field emission gun operated at 200kV yielding a point-to-point resolution of 0.19 nm. An energy-dispersive X-ray (EDX) detector was used to obtain elemental composition maps in combination with atomic number-contrast STEM imaging with a high-angle annular dark field (HAADF) detector.

Atom probe data collection was executed in an Imago LEAP 3000X HR local electrode atom probe operated in laser (532 nm wavelength) pulsing mode. The base pressure in the analysis chamber was below  $5 \times 10^{-11}$  mbar. While all investigated specimens had a similar geometry with a tip radius smaller than 50 nm and a shank angle around  $10^\circ$ , we found that two different parameter sets were needed for measurements for the two substrate materials, MgO and Si/SiO $_2$ . The parameters were chosen to maximize the signal-to-noise ratio and avoid pronounced thermal tails in the recorded mass spectra. In case of bilayers grown on MgO, a pulse rate of 200 kHz and pulse energy of 0.2 nJ at a specimen base temperature of 60 K yielded the highest spectral quality. Samples deposited on Si/SiO $_2$  were analyzed with pulse energy of 0.1 nJ and a repetition rate of 200 kHz at 40 K. The three-dimensional reconstruction of the tips was performed with the Cameca IVAS 3.6.6 software based on the tip radius evolution with increasing evaporation voltage. Input parameters were an evaporation field of 30 V nm $^{-1}$ , image compression factor of 1.65 and field factor of 3.3.

First-principles calculations based on DFT employing the generalized-gradient approximation with the PBEsol exchange-correlation functional [54] were performed with the Vienna *ab initio* simulation package [119, 153]. Ion-electron interactions were described by means of the projector augmented wave method [115], with a plane-wave energy cutoff of 400 eV. For all calculations, a  $3 \times 3 \times 3$  supercell of TiN was used, consisting of 216 atoms for a defect-free cell. A Monkhorst-Pack k-point mesh [120] of  $4 \times 4 \times 4$  was used for Brillouin zone sampling with a

## 6.3. Experimental Results and Discussion

Methfessel-Paxton [154] smearing of 0.2 eV. This k-point mesh ensures the convergence of the migration barriers within 10 meV. The calculations were performed with two different lattice constants: i) 4.212 Å (corresponding to the equilibrium lattice parameter at 0 K) and ii) 4.278 Å (corresponding to the experimental value at 1273K [132]). Migration barriers were calculated using the nudged elastic band method [155] (NEB) with three intermediate images. For selected cases, the convergence of the minimum-energy pathway was tested by comparing NEB calculations with three and seven intermediate images. The resulting heights of the migration barriers were found to agree within our numerical accuracy, suggesting that three intermediate images are sufficient for the present investigations. The equilibrium defect concentrations were predicted by the dilute-solution model [76, 156] (DSM) as a function of the TiN composition.

## 6.3 Experimental Results and Discussion

### 6.3.1 Structure of Pristine TiN/Cu Stacks

Figure 6.2 shows X-ray diffractograms comparing patterns of as-deposited TiN/Cu bilayers grown on (001)-oriented MgO and Si/SiO<sub>2</sub> substrates. Both samples were measured in grazing incidence and Bragg-Brentano geometry. In Bragg-Brentano mode the scattering vector is always oriented normal to the substrate surface and thus only reflections from crystallographic planes parallel to the substrate plane are observable. However, in grazing incidence configuration the Bragg reflections are caused by sets of crystallographic planes that are not parallel to the substrate surface nor to each other [157]. This fact can be utilized when comparing data from single- and polycrystalline films measured in both configurations. Figure 6.2(a) shows the grazing incidence diffractogram of the TiN/Cu stack grown on Si/SiO<sub>2</sub>. All peaks are consistent with (111), (200), and (220) reflections of fcc TiN [158] or fcc Cu [159], indicating that both layers are polycrystalline when grown on Si/SiO<sub>2</sub>. Due to the small incidence angle of 2° no Si substrate peak is observable. The measurement in Bragg-Brentano mode (not shown) yields an identical diffraction pattern apart from an additional Si substrate peak at 69.1°. On the other hand, the TiN/Cu bilayer assembly deposited on a MgO substrate (Figure 6.2(b)) exhibits no peaks in grazing incidence geometry, suggesting that the TiN as well as the Cu layer grow with their (001) planes oriented parallel with the substrate surface.

This can be verified by repeating the measurement in Bragg-Brentano mode. In this configuration, a pronounced double peak is observable, related to the (200) planes of the TiN film and the MgO substrate [158, 160]. Additionally, a reflection consistent with the (001)-oriented Cu toplayer [159] appears at a diffraction angle of 50.4°, indicating that both the TiN and the Cu layer grow

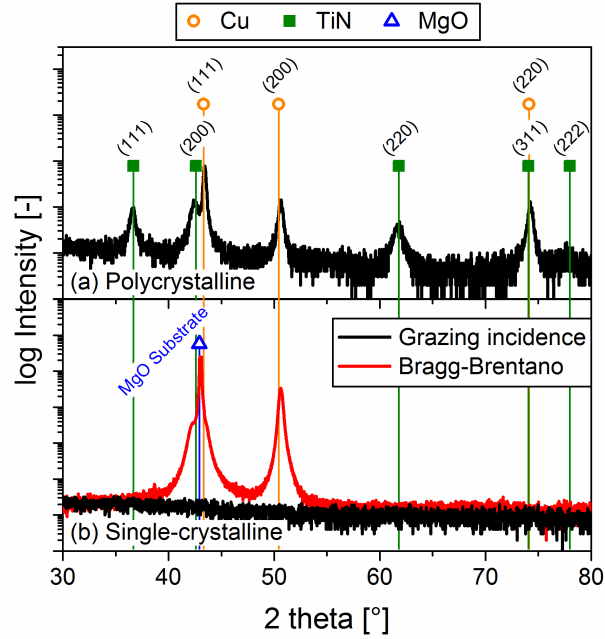


**Figure 6.2:** X-ray diffractograms of pristine TiN/Cu stacks grown on (a) Si(001)/SiO<sub>2</sub> and (b) MgO(001) measured in grazing incidence and Bragg-Brentano geometry.

epitaxially on (001)-oriented MgO. Since the lattice parameters of fcc TiN and fcc MgO are almost identical (4.24 and 4.21 Å, respectively), which is also evident in the peak overlap in the diffractogram, epitaxial TiN of high single-crystalline quality can be grown readily on MgO substrates, given enough energy is provided during film nucleation and growth. In case of the epitaxial Cu toplayer misfit dislocations will relieve some of the strain between the TiN and Cu lattices. This is confirmed by high-resolution TEM investigations (Figure 6.3) of the pristine TiN/Cu bilayer deposited on MgO (001). Figure 6.3(a) provides a cross-sectional overview image of the layer arrangement obtained with a HAADF detector in STEM mode. Both layers appear single-crystalline and free of grain boundaries within the observed area. Furthermore, the interfaces are smooth and without any evident interdiffusion. Information about the atomic arrangement directly at the Cu-TiN interface can be gained from a high-resolution bright-field micrograph recorded along the [100] zone axis (Figure 6.3(b)). The measured lattice spacing of the (020) planes in Cu is 0.182 nm. Compared to the bulk value of 0.181 nm for fcc Cu [159], the Cu layer is minimally strained along the [010] direction. Since the lattice mismatch between Cu and TiN is -17 %, fully strained epitaxial growth of Cu would result in a larger lattice strain. The excessive strain is thus relaxed by misfit dislocations at the Cu-TiN interface as also found in Refs. [161, 162]. A similar mechanism has also been observed for the growth of epitaxial Cu on MgO(001) [163]. As an example, one misfit dislocation represented by an extra half plane in the Cu layer terminating at the interface is marked with

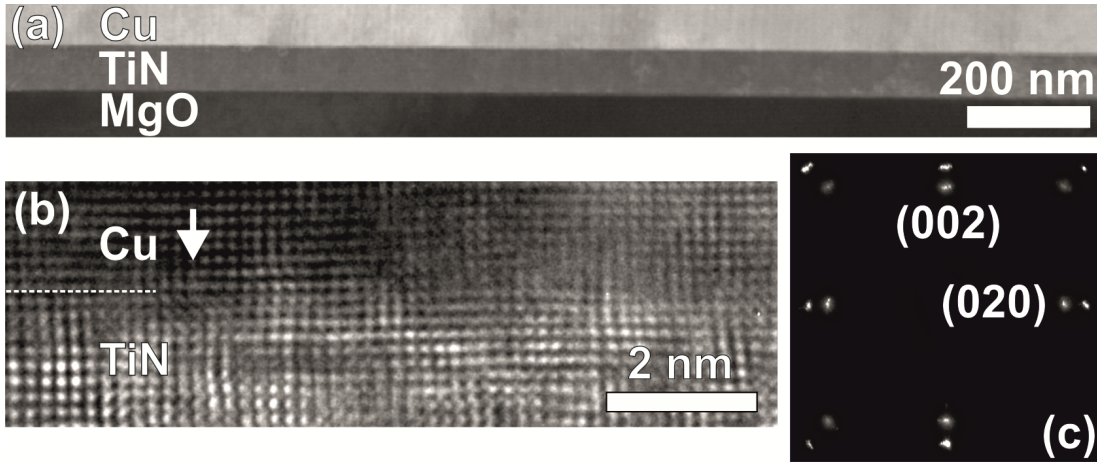


**Figure 6.3:** TEM images of the pristine single-crystal TiN/Cu stack grown on MgO(001): (a) cross-sectional dark field image giving an overview of the layer arrangement, (b) high-resolution bright field micrograph of the Cu-TiN interface with a misfit dislocation marked by an arrow, and (c) the corresponding SAED pattern showing an epitaxial cube-on-cube orientation relationship between the Cu and the TiN layer.

an arrow in Figure 6.3(b). The (020) lattice spacing in the TiN layer is 0.202 nm. With respect to the bulk value of 0.212 nm, TiN is compressed along the [010] direction. In addition to the complex strain state resulting from the lattice mismatch between the layers and the substrate, and the differential contraction of the materials during cooling-down from deposition temperature [164], another possible reason for these compressive lattice strains could be the incorporation of Ar as well as the interplay of point defects (interstitials and vacancies) often observed in sputtered TiN [9, 165, 166]. To confirm epitaxial growth of the TiN/Cu stack, selected area electron diffraction (SAED) patterns were recorded along the Cu-TiN interface. A representative SAED pattern (Figure 6.3(c)) shows spots consistent with single-crystal Cu (appearing farther outside due to the smaller lattice parameter) and single-crystal TiN with a cube-on-cube alignment between the two layers.

In contrast, the TiN film grown on the Si/SiO<sub>2</sub> substrate exhibits a fine grained nucleation layer close to the TiN-Si/SiO<sub>2</sub> interface, morphing into a typical polycrystalline zone T microstructure [167] with a dense array of cone-shaped columnar grains, as displayed in the cross-sectional bright-field TEM image in Figure 6.4(a). The Cu toplayer consists of comparably large grains without a discernible orientation relationship to the underlying TiN. While the TiN-Cu interface is smooth and well-defined, the Cu surface is wavy. A bright surface layer visible on top of the Cu film can be related to the formation of a native CuO<sub>2</sub> layer in ambient atmosphere. Similarly, the amorphous SiO<sub>2</sub> grown to prevent Si diffusion into the TiN film is visible in Figure 6.4(a) as a bright 5 nm

## Chapter 6. Cu Diffusion in Single-crystal and Polycrystalline TiN Barrier Layers: A High-Resolution Experimental Study Supported by First-principles Calculations

thick interlayer at the TiN-Si interface. To rule out the possibility of Cu diffusion occurring already during the deposition process, micrographs as shown in Figure 6.4(b) were recorded with a HAADF detector, where the contrast scales with  $Z^2$  (atomic number squared) [168, 169]. No inter-diffusion layers of different contrast were detected across either of the two interfaces, nor along the grain boundaries in TiN. A SAED pattern obtained along the [110] zone axis at the TiN-Si interface (Figure 6.4(c)) shows diffraction rings for polycrystalline TiN in agreement with the XRD investigations. Brighter sections of the rings are not related to film texture but to the restricted sample area and thus the limited number of grains illuminated within the selected area aperture. Figure 6.4(d) provides a closer look at the Cu-TiN interface in a high-resolution micrograph. As an example, two grain boundaries running almost perpendicular to the interface in the columnar TiN barrier layer are marked by arrows. The boundaries are dense without discernible intercolumnar porosity. In the vicinity of the interface the column width is approximately 10-15 nm. The Cu-TiN interface is flat and the tops of the TiN columns are only marginally rounded, revealing very shallow troughs at the boundaries.

Not only the film structure but also the film density affects the diffusion barrier performance [20]. Therefore, we investigated the development of the density in the TiN/Cu stack by XRR measurements. In our previous study [24], we found that the density of a single-crystal TiN film deposited on MgO(001) with the same parameters as for the TiN barriers presented in this paper was  $5.4 \pm 0.2 \text{ g cm}^{-3}$ , which is in agreement with the bulk value [8] of  $5.39 \text{ g cm}^{-3}$ . Due to the contribution of grain boundaries, sputtered polycrystalline films are generally expected to be less dense. The recorded XRR curve for the polycrystalline barrier is shown in Figure 6.5(a). The best fit was achieved by a model comprised of a 4.8 nm thick  $\text{CuO}_2$  surface layer, a 139.0 nm thick Cu layer, a 214.6 nm thick TiN barrier, and a 4.9 nm thick  $\text{SiO}_2$  layer on the Si substrate. A slight deviation in film thicknesses measured by TEM and obtained from XRR fits can be attributed to variations due to shadowing effects at the outer margins of the samples and the limited area observed in TEM. Figure 6.5(b) displays the resulting density depth profile, where the zero point is defined as the interface between the Si substrate and the thermal  $\text{SiO}_2$ . The density of the polycrystalline TiN layer deposited at  $700^\circ\text{C}$  is  $5.3 \pm 0.2 \text{ g cm}^{-3}$ , which is 98 % of bulk density. Similar observations have been reported by Petrov et al. [149] and Patsalas et al. [170], who found that given enough energy in the form of moderate ion bombardment or substrate heating is provided to the film forming species to promote ad-atom surface diffusion and to fill voids, sputtered polycrystalline TiN films will grow with almost fully dense grain boundaries and a relatively low intragranular defect density. Although the grain boundaries still will be the main diffusion channel in polycrystalline barrier layers, their high internal density is expected to restrict the migration of Cu atoms more severely than in comparable barrier layers deposited

### 6.3. Experimental Results and Discussion

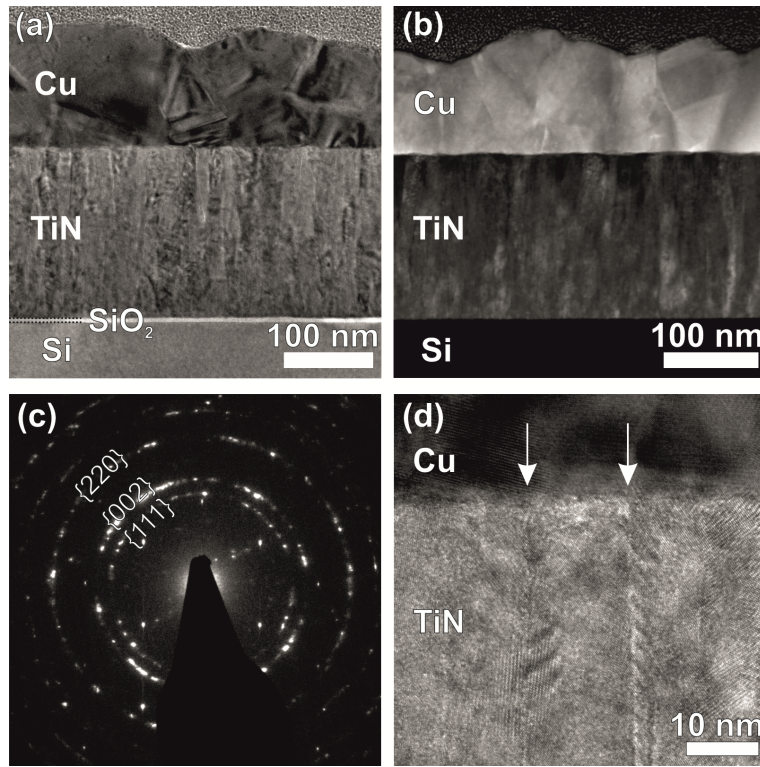


**Figure 6.4:** TEM images of the pristine polycrystalline TiN/Cu stack grown on Si/SiO<sub>2</sub>: (a) cross-sectional bright field image giving an overview of the layer arrangement, (b) dark field micrograph displaying no discernible Cu or Si diffusion along the grain boundaries between columnar TiN grains, (c) corresponding SAED pattern showing (111), (002), and (220) diffraction rings related to TiN, and (d) a high-resolution bright field micrograph of the Cu-TiN interface with two grain boundaries marked by arrows.

at lower substrate temperatures without externally applied bias potential. The density of the Cu toplayer with a value of  $8.6 \pm 0.2 \text{ g cm}^{-3}$  is slightly below bulk density ( $8.9 \text{ g cm}^{-3}$ ), owing to limited atomic mobility during the growth process at  $50^\circ\text{C}$  and floating potential.

#### 6.3.2 Diffusion in Annealed TiN/Cu Stacks

To activate the diffusion of Cu from the toplayer into the TiN films, the samples were subjected to isothermal annealing treatments at  $900^\circ\text{C}$  for 1 h. In case of the single-crystal TiN/Cu stack, de-wetting of the Cu toplayer was evident after the annealing treatment. The reasons for solid state de-wetting of Cu films include strain-induced instabilities due to the lattice mismatch and faceting instabilities (surface energy  $\gamma_{\text{Cu}(111)} < \gamma_{\text{Cu}(001)}$ ) [171]. This behavior was observed previously and can be interpreted as a sign of the efficiency of the employed bar-

Chapter 6. Cu Diffusion in Single-crystal and Polycrystalline TiN Barrier Layers: A High-Resolution Experimental Study Supported by First-principles Calculations

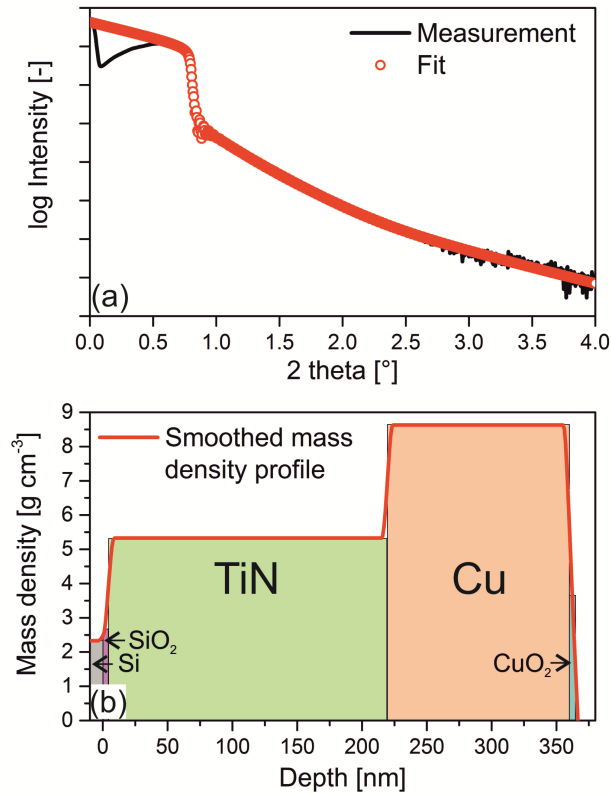


**Figure 6.5:** (a) Experimental and calculated XRR (fitted by a genetic algorithm fit according to the Nevot-Croce interface model) curves and (b) corresponding density depth profile of the polycrystalline TiN/Cu stack grown on Si/SiO<sub>2</sub> at 700°C.

rier layer [172]. Further investigations were performed directly at the center of the formed Cu agglomerates, to ensure that enough Cu was available as a diffusion source. Cross-sectional TEM images of the TiN/Cu stacks after annealing obtained with a HAADF detector are shown in Figure 6.6. The single-crystal TiN/Cu bilayers grown on MgO(001) (Figure 6.6(a)) still exhibit no internal structure, indicating that the epitaxial configuration is stable up to temperatures of 900°C. The Cu toplayer is now discontinuous and has agglomerated to islands with a diameter of up to 4 μm due to solid state de-wetting. A black rectangle at the Cu-TiN interface marks the area where the corresponding qualitative EDX maps, also displayed in Figure 6.6(a), have been recorded with the pixel size set to 1 × 1 nm<sup>2</sup>. The RGB image constructed from the signals of the Cu-K and the Ti-K edges, which are also shown separately for clarity, has an area of 20 × 50 nm<sup>2</sup>. The signal from the N-K edge was too weak to be considered significant and is therefore not plotted. During scanning, the Cu-TiN interface was oriented slightly inclined, to ensure that no sample drift took place influencing the EDX mapping over the otherwise featureless sample. No discernible diffusion of Cu across the interface could be detected by EDX.

### 6.3. Experimental Results and Discussion

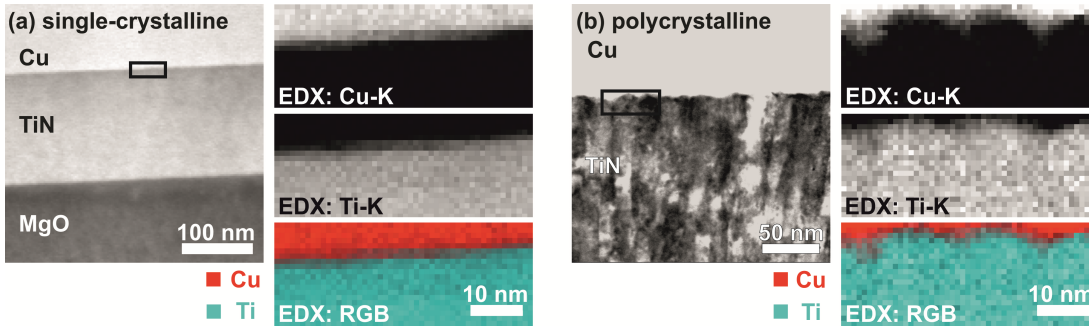


**Figure 6.6:** STEM-HAADF images and corresponding EDX maps (pixel size  $1 \times 1$  nm) of the Cu-K and the Ti-K edges of the (a) single-crystal TiN/Cu stack grown on MgO(001) and (b) polycrystalline TiN/Cu stack grown on Si/SiO<sub>2</sub> after the annealing treatment (900°C, 1 h).

In contrast to the single-crystal bilayers, the onset of grain boundary diffusion is evident in the polycrystalline TiN/Cu stack presented in Figure 6.6(b). While the Cu-TiN interface is smooth with minimal troughs at the column boundaries in the pristine sample (Figure 6.4(a,d)), pronounced Cu accumulation and beginning penetration is observed locally at TiN column boundaries after annealing at 900°C for 1 h, leading to a wavy appearance of the interface. Corresponding elemental maps (pixel size  $1 \times 1$  nm<sup>2</sup>) confirm the preferential diffusion of Cu along grain boundaries in the polycrystalline TiN layer. Because of the uncertainty of the exact location of the interface and limitations in the spatial resolution of the probe, it is however not possible to quantify the diffusion length precisely from the acquired maps. Moreover, according to Ficks second law, the concentration of the diffusing Cu atoms will decrease with increasing diffusion length [173]. In combination with the small excitation volume in the thin TEM foil, the EDX detector might not receive sufficient X-ray counts to resolve the low Cu concentrations further along the grain boundaries [174].

To complement the TEM findings, the annealed single- and polycrystalline TiN/Cu bilayers were also investigated by APT. Three datasets were measured and evaluated in each case with consistent results. A cylindrical region of interest ( $\varnothing 20$  nm  $\times$  100 nm) containing the Cu-TiN interface is shown in Figure 6.7 for both samples after annealing at 900°C. For clarity, only Cu and TiN ions have been plotted. Throughout the TiN layer, Ti and N ions have also been detected in their dissociated forms, but are not shown here. Additionally, significant amounts of Ar ions have been observed as impurities. This is a result of the sputter deposition process, where Ar ions impinge on the growing film and become trapped [175].

Hereafter, the differences in chemical composition and diffusion characteristics in the two samples will be discussed in more detail: Figure 6.7(a) shows the three-dimensional reconstruction of the annealed single-crystal TiN/Cu stack. Each data point in the reconstruction represents one measured Cu or TiN ion. The

## Chapter 6. Cu Diffusion in Single-crystal and Polycrystalline TiN Barrier Layers: A High-Resolution Experimental Study Supported by First-principles Calculations

corresponding volume concentration distribution of Cu ions is plotted alongside to visualize the elemental composition in the vicinity of the interface. The N/Ti ratio in the TiN(001) barrier layer, obtained after performing a decomposition of overlapping peaks in the recorded APT mass spectrum, is 0.92. This ratio is confirmed by elastic recoil detection analysis of a single-layer TiN(001) film deposited with the same parameters as the studied barrier layer, indicating that the peak decomposition algorithm is suitable to accurately describe the chemical composition in the investigated sample volumes. A slightly substoichiometric composition is typical for sputtered TiN films, and N vacancies have been identified as the primary defect in these structures [148, 176]. Ar impurities are evenly distributed in the TiN(001) barrier layers as discrete atoms without any evident clustering. According to APT the overall Ar concentration in TiN is below 1 at. %. The Cu(001) layer is essentially Ar free as a result of the limited ion irradiation during the deposition at floating potential. The Cu-TiN interface appears well-defined in the reconstruction. Only minor intermixing with some Cu atoms positioned in the TiN layer (3 nm into the TiN layer, one out of every 100 atoms is Cu) and vice versa can be observed in the near interface region. In the concentration distribution of Cu, a rapid drop occurs from 100 at. % Cu in the pure Cu film to 0 at. % Cu in the barrier layer. This behavior corroborates the TEM and EDX findings, confirming that single-crystal TiN is effective in preventing Cu diffusion after annealing at 900°C for 1 h. The onset of Cu diffusion into the TiN(001) barrier could only be observed after a 12 h annealing treatment at 1000°C, as reported in our previous study [24]. The good performance of this barrier can be related to the dense, ordered structure of the single-crystal TiN layer and the lack of fast diffusion channels such as grain boundaries.

Figure 6.7(b) displays the reconstruction and Cu distribution profile in a representative annealed polycrystalline APT specimen. All of the three evaluated specimen reconstructions contained at least one TiN grain boundary along which Cu diffusion was observed. The reconstruction shown in Figure 6.7(b) was chosen as a representation because the specimen contained several grain boundaries, and thus offered the most diverse illustration of Cu diffusion profiles. Again the chemical composition of the TiN layer was calculated after analyzing the mass spectrum. The obtained N/Ti ratio of 0.99 is higher than for the single-crystalline case. During the annealing treatment, the grain boundaries can act as sinks for N vacancy annihilation in polycrystalline TiN, giving a possible explanation for this observation [177]. Furthermore, a change in the distribution of Ar impurities is evident when a larger reconstructed region (not shown here) of the TiN layer is investigated. While the Ar is still evenly spread throughout the TiN, some Ar bubbles with a diameter in the range of a few nanometers can be found. Presumably, the formation of these bubbles is energetically more favorable at the boundaries between the columnar grains, because of the relatively large stress associated with the incorporation of Ar in bulk TiN [175, 178]. The overall Ar

### 6.3. Experimental Results and Discussion

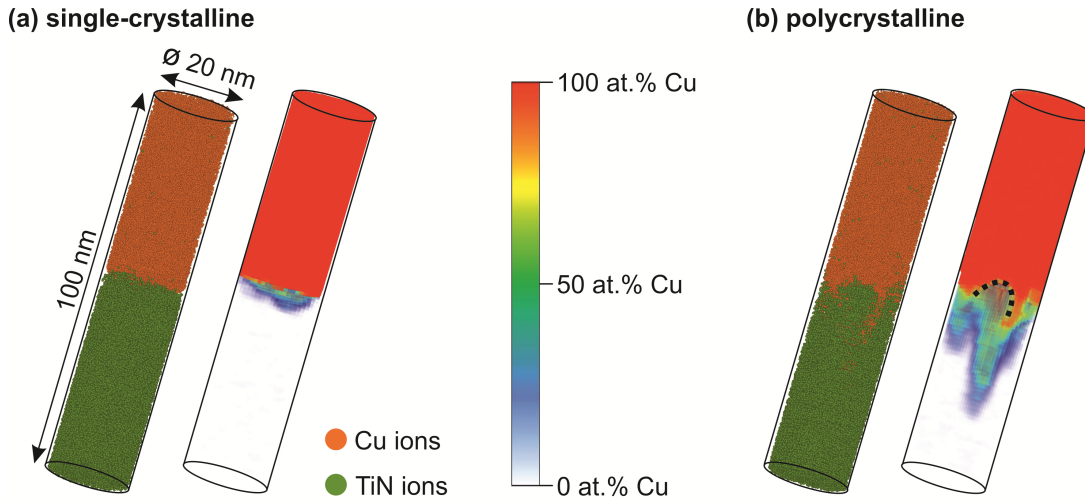


**Figure 6.7:** Three-dimensional APT reconstructions ( $\varnothing 20 \text{ nm} \times 100 \text{ nm}$ ) and corresponding Cu concentration plots of the (a) single-crystal TiN/Cu stack grown on MgO(001) and (b) polycrystalline TiN/Cu stack grown on Si/SiO<sub>2</sub> after the annealing treatment (900°C, 1 h).

concentration in the TiN layer is below 1 at. %, and no Ar impurities could be observed in the Cu layer. To our knowledge, this is the first observation of Ar bubbles in TiN films containing so little as 1 at. % Ar, and corroborates the usefulness of APT for functional ceramics.

In the three-dimensional reconstruction shown in Figure 6.7(b), local migration of Cu across the interface is evident, which is indicative of an active grain boundary diffusion mechanism during the annealing treatment at 900°C. This is even more prominently displayed in the volume concentration plot of Cu. The TiN structure revealed in the TEM images (Figure 6.6(b)) after annealing is reproduced with its characteristic columns (diameter in the range of 10-15 nm) and troughs at the boundaries, as marked by the black dotted line in the APT concentration plot in Figure 6.7(b). Along these boundaries a locally increased Cu concentration can be measured. A grain boundary represents a transition structure between two crystals and thus the incorporation of local defects is required to account for the change in grain orientation and translation. Therefore, the atomic packing in a grain boundary core is less dense than in a perfect crystal. As a result, a grain boundary will always provide a faster diffusion path than a single crystal [179]. Still, the migration of atoms along the boundary may be hindered by tuning its density. In the present study, a high internal density of grain boundaries was achieved by promoting the ad-atom surface diffusion and film densification during deposition of the TiN barrier layer by supplying energy in the form of substrate heating (700°C) and moderate ion bombardment (-100 V bias potential). The longest Cu diffusion path measured in a grain boundary

## Chapter 6. Cu Diffusion in Single-crystal and Polycrystalline TiN Barrier Layers: A High-Resolution Experimental Study Supported by First-principles Calculations

in Figure 6.7(b) is approximately 30nm. In comparison, the diffusion depth in a polycrystalline TiN barrier deposited at room temperature without an externally applied bias potential was already more than 25nm after annealing for 30min at temperatures as low as 750°C, as reported by Moriyama et al. [27]. Figure 6.7(b) also shows that the penetration depth of Cu into the TiN layer is not uniform, which further illustrates the dependence of Cu migration through grain boundaries on their atomic structure. For example, it was found that grain boundaries with small misorientation and mosaic spread angles generally perform better in constricting diffusion, due to their higher atomic packing density [27, 180, 181]. In this context it also has to be noted that because of the nature of TEM and especially APT investigations, only limited areas of the samples could be analyzed. It is therefore possible that for other grain boundary configurations in the same sample, Cu atoms could migrate further into the TiN layer. However, to demonstrate the general good performance of the dense polycrystalline TiN barrier, we assume a maximum diffusion length of 30nm as measured in Figure 6.7(b). Since no significant lattice diffusion is observed in the single-crystal TiN film, it is further assumed that diffusion only occurs along the grain boundaries and diffusion into the grains is negligible. With an infinite source diffusion approximation, the grain boundary diffusion coefficient  $D$  at a given temperature can then be derived from Einsteins formula [60]

$$\bar{x} = 2\sqrt{Dt}, \quad (6.1)$$

where  $t$  is the time for diffusion. This yields a grain boundary diffusion coefficient of  $(6 \pm 2) \times 10^{16} \text{cm}^2 \text{s}^{-1}$  for a temperature of 900°C in dense polycrystalline TiN, which is 1-2 orders of magnitude lower than for comparable TiN coatings deposited without external substrate heating [27, 28].

### 6.4 Theoretical Considerations on Cu Diffusion in Single-crystal TiN(001)

The experiments outlined above suggest that diffusion in polycrystalline TiN occurs via grain boundaries at a rate 2 orders of magnitude higher than bulk diffusion [24]. To explain such a difference, a thorough comparison of the diffusion mechanisms in bulk and along the grain boundaries is required. There are, however, two factors to consider: i) the structure of the grain boundaries involved in the diffusion process is presently unknown; and ii) although the Cu-diffusion in bulk TiN has already been investigated by means of ab initio atomistic calculations [29], the relevant diffusion mechanism and the role of stoichiometry in TiN remains unclear. Thus, in this section the focus is laid on the diffusion mechanisms in single-crystal TiN.

#### 6.4. Theoretical Considerations on Cu Diffusion in Single-crystal TiN(001)

The diffusion process from a macroscopic point of view can be described with an Arrhenius type equation:

$$D = D_0 \exp(-Q/k_B T). \quad (6.2)$$

Here,  $D_0$  is the exponential pre-factor and  $Q$  is the activation energy. The diffusion parameters,  $D_0$  and  $Q$ , are determined by the underlying atomistic mechanism of diffusion and are often used to compare different mechanisms. To predict the most probable diffusion mechanism, the activation energies corresponding to various possible mechanisms described below were calculated, and the mechanism with the lowest activation energy was identified as the most likely one for the diffusion of Cu in bulk-like TiN. In particular, it has to be distinguished between vacancy-mediated impurity diffusion and a diffusion mechanism via interstitial positions. The vacancy-mediated impurity diffusion coefficient for a fcc lattice can be written as follows [73]:

$$D_2 = a^2 f_2 C_v \omega_2. \quad (6.3)$$

Here,  $a$  is the lattice parameter,  $f_2$  is the impurity diffusion correlation factor,  $C_v = \exp(-\frac{G_f + G_b}{k_B T})$  is the vacancy concentration adjacent to the solute atom and  $\omega_2 = \frac{k_B T}{h} \exp(-\frac{G_2^m}{k_B T})$  is the impurity jump rate from transition state theory [63]. The free energies difference  $G$  (symbol  $\Delta$  is omitted for convenience) in the previous equations can be written as  $G = E - TS$  with  $E$  being the energy difference and  $S$  the entropy difference. Thereby, equation 6.3 becomes

$$D_2 = \frac{k_B T}{h} a^2 f_2 \exp\left(\frac{S_f + S_b + S_2^m}{k_B}\right) \exp\left(-\frac{E_f + E_b + E_2^m}{k_B T}\right). \quad (6.4)$$

Here,  $E_f(S_f)$  is the vacancy formation energy (entropy) and  $E_b(S_b)$  is the vacancy-impurity binding energy (entropy). The latter is defined as the difference between vacancy formation energy (entropy) in the vicinity of solute atoms and that in the pure bulk. In the convention adopted here, negative values of  $E_b$  correspond to an attractive interaction between vacancy and solute. Finally,  $E_2^m(S_2^m)$  is the impurity migration energy (entropy). This is the energy (entropy) difference between the system in the initial state and the system in a configuration corresponding to the top of the energy barrier which the impurity atom has to overcome in order to diffuse to the nearest-neighboring vacancy site.

For the interstitial diffusion mechanism, the diffusion coefficient is given by the following expression:

$$D_2 = \frac{k_B T}{h} a^2 \exp\left(\frac{S_{int}^m}{k_B}\right) \exp\left(-\frac{E_{int}^m}{k_B T}\right). \quad (6.5)$$

Chapter 6. Cu Diffusion in Single-crystal and Polycrystalline TiN Barrier Layers: A High-Resolution Experimental Study Supported by First-principles Calculations

**Table 6.1:** Calculated excitation energies of intrinsic point defects in TiN. The ground state energy per formula unit of the stoichiometric TiN is  $E_0 = -19.912$  eV.

Defect	Excitation energy (eV)
$V_N$	10.705
$V_{Ti}$	11.972
$Ti_N$	10.098
$N_{Ti}$	11.957
$Ti_{Int}$	-1.636
$N_{Int}$	-3.918

In the present study the entropic, in particular vibrational, contributions were not taken into account, which prohibits calculating  $D_2$ . However, when comparing equations 6.4 and 6.5 to the Arrhenius form for the diffusion coefficient (equation 6.2), the activation energy can be approximated as  $Q = E_f + E_b + E_2^m + C$  (here  $C$  takes the contribution from the correlation factor into account) for vacancy mediated mechanisms and  $Q = E_{int}^m$  for the interstitial mechanism. In the following, we focus on comparing activation energies obtained for various mechanisms, in order to clarify their relative importance.

### 6.4.1 Defect Concentrations

The simplest point defects considered are vacancies both on the N and Ti sublattices denoted as  $V_N$  and  $V_{Ti}$ , respectively, antisites ( $Ti_N$  and  $N_{Ti}$ ) and interstitials ( $Ti_{Int}$  and  $N_{Int}$ ). In order to compute concentrations of those defects within the DSM, the associated excitation energies are calculated. They are defined as the energy difference between the defective and the perfect supercell.

Defect excitation energies are shown in Table 6.1. Here, the effect of temperature was taken into account by using the supercell calculations with the experimentally measured lattice parameter at 1273 K [132], but no entropy contribution was considered. It has to be noted that the values of the excitation energies themselves do not have a direct physical meaning, since they are governed by the number and kind of atoms in the supercells, which are different for each considered defect.

Solving the DSM, concentrations of defects ( $c_d$ ) as well as chemical potentials of Ti and N ( $\mu_{Ti}$  and  $\mu_N$ ) are obtained as a function of the TiN composition. The concentrations of defects are converted to the effective formation energies ( $E_f$ ) using the relation  $E_f = -k_B T \ln(c_d)$ , where  $k_B$  denotes the Boltzmann constant and  $T$  is the temperature. These energies are shown in Figure 6.8 as a function of the N concentration in TiN.  $V_N$  and  $V_{Ti}$  have the lowest defect formation energies in the N-deficient and Ti-deficient region respectively, and consequently they are the dominant defects in the corresponding concentration regions. Therefore, it

#### 6.4. Theoretical Considerations on Cu Diffusion in Single-crystal TiN(001)

can be concluded that the only defects which can significantly influence the Cu diffusion process are vacancies, while contributions from other types of defects are negligible.

Furthermore, the formation energies  $E_f(\text{Cu}_X)$  of a Cu impurity on the corresponding sublattices X (Ti, N or Int) in TiN are calculated. The following relations were used for calculating  $E_f(\text{Cu}_X)$  for a dilute concentration of Cu:

$$\begin{aligned} E_f(\text{Cu}_{\text{Ti}}) &= E(\text{Cu}_{\text{Ti}}) - E(\text{TiN}) + \mu_{\text{Ti}} - \mu_{\text{Cu}}, \\ E_f(\text{Cu}_{\text{N}}) &= E(\text{Cu}_{\text{N}}) - E(\text{TiN}) + \mu_{\text{N}} - \mu_{\text{Cu}}, \\ E_f(\text{Cu}_{\text{Int}}) &= E(\text{Cu}_{\text{Int}}) - E(\text{TiN}) - \mu_{\text{Cu}}. \end{aligned} \quad (6.6)$$

Here,  $E(\text{TiN})$  is the total energy of the bulk TiN supercell,  $E(\text{Cu}_X)$  is the total energy of the TiN supercell with Cu on site X, and  $\mu_{\text{Cu}}$  is the chemical potential of Cu corresponding to the energy per atom in fcc Cu. The calculated values of  $E_f(\text{Cu}_X)$  are plotted in Figure 6.9. In the N-deficient region of TiN, the Cu impurities reside mostly on the N sublattice, while they occupy the Ti sublattice in stoichiometric TiN. The formation energy on the interstitial sublattice is significantly higher compared to the other two sublattices, which implies that the fraction of interstitial Cu impurity atoms is nearly vanishing in the whole considered composition range.

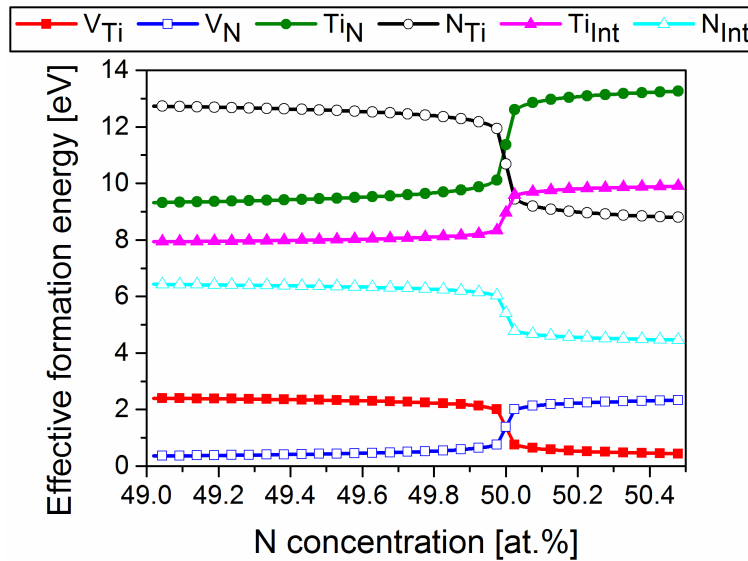


**Figure 6.8:** Effective formation energy of point defects in TiN as a function of composition obtained from the DSM at a temperature of 1273 K.

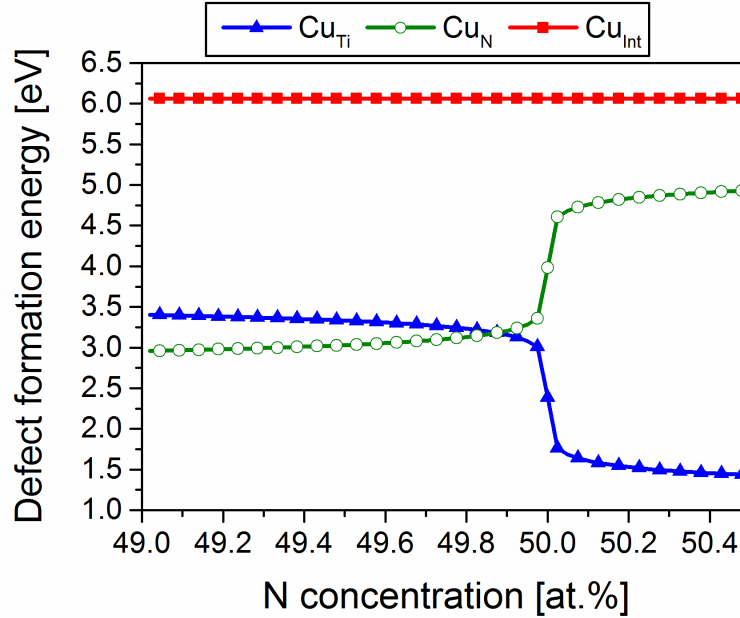


**Figure 6.9:** Formation energy  $E_f(\text{Cu}_x)$  of a Cu impurity on different sites in TiN as a function of composition at 1273 K.

## 6.4.2 Migration Barriers and Activation Energies

Considering the two types of diffusion mechanisms discussed above, the respective migration barriers and the total diffusion activation energies have been calculated. The simplest possible diffusion mechanism for a Cu impurity in the TiN single crystal is diffusion via interstitial sites as described by equation 6.5. The most stable interstitial configuration for a Cu atom is found to be in the center of a TiN cell. Migration of a Cu impurity between stable positions is calculated using the NEB method and occurs with the energy barrier  $E_{Int}^m$  of 1.39 eV at 0 K and at the slightly lower value of 1.23 eV at high temperature, owing to the larger lattice spacing at elevated temperatures. The energy barrier of 1.39 eV at 0 K is in good agreement with the previously calculated value of 1.4 eV (Table 6.2).

The second possible mechanism for Cu impurity diffusion is via vacancies as described by equation 6.4. In this case, diffusion takes place via solute-vacancy exchange jumps. Both possibilities of Cu atom diffusion either via the Ti sublattice or via the N sublattice are considered: The five-frequency model [73] is applied to analyze these processes. This model is commonly used to describe the impurity diffusion correlation factor, which depends on the vacancy-jump frequencies near the impurity. Taking into account vacancy-impurity interactions only up to the second-nearest neighbor, in this model the correlation factor  $f_2$  from equation 6.3 for the diffusion coefficient in the fcc lattice can be written as [74]

#### 6.4. Theoretical Considerations on Cu Diffusion in Single-crystal TiN(001)

$$f_2 = \frac{2\omega_1 + 7F\omega_3}{2\omega_2 + 2\omega_1 + 7F\omega_3}, \quad (6.7)$$

where

$$7F = 7 - \frac{10\alpha^4 + 180.5\alpha^3 + 927\alpha^2 + 1341\alpha}{2\alpha^4 + 40.2\alpha^3 + 254\alpha^2 + 597\alpha + 436}. \quad (6.8)$$

Here,  $\alpha = \omega_4/\omega_0$ , and  $\omega_i = \frac{k_B T}{h} \exp\left(-\frac{E_i^m}{k_B T}\right)$  are the rates of different types of vacancy jumps in the vicinity of a solute atom with being equal to the migration barrier of the corresponding jump (entropic contribution is not included).  $\omega_2$  corresponds to the solute-vacancy exchange jumps,  $\omega_1$  is the rate of vacancy-solvent jumps in the first coordination shell of the solute atom,  $\omega_3$  is the rate of vacancy jumps from the first-nearest neighbor positions to solute atoms at more distant sites, and  $\omega_4$  is the rate of reverse jumps. All other vacancy-solvent jumps are assumed to occur at a rate of  $\omega_0$ , which corresponds to the solvent-vacancy exchange jump in the pure solvent.

The migration barriers  $E_i^m$  corresponding to all  $\omega_i$  for Cu diffusion are calculated both via the Ti and N sublattice and are presented together with the value for the barrier for migration via interstitial sites  $E_{Int}^m$  in Table 6.2. For the numerator in equation 6.7 it has been found that  $2\omega_1 \gg 7F\omega_3$ , and  $2\omega_2 \gg (2\omega_1 + 7F\omega_3)$  for the denominator. Therefore, equation 6.7 can be approximated as  $f_2 \approx \omega_1/\omega_2$ . Substituting equation 6.7 into equation 6.3 for the diffusion coefficient results in

$$D_2 = a^2 C_v \omega_1. \quad (6.9)$$

**Table 6.2:** Migration barriers  $E_i^m$  [eV] corresponding to the different vacancy exchange jumps ( $\omega_i$ ) in the vicinity of the impurity atom and for migration via interstitial sites calculated with the lattice parameters at 0 K and 1273 K.

		$E_0^m$	$E_1^m$	$E_2^m$	$E_3^m$	$E_4^m$	$E_{Int}^m$
Ti sublattice	0 K	4.08	2.96	0.27	4.18	4.16	
	1273 K	3.69	2.54	0.08	3.74	3.74	
N sublattice	0 K	3.75	2.62	1.90	4.14	4.20	
			(2.8 <sup>a</sup> )	(2.0 <sup>a</sup> )			
	1273 K	3.32	2.20	1.70	3.67	3.63	
Interstitial	0 K						1.39
							(1.4 <sup>a</sup> )
	1273 K						1.23

<sup>a</sup>Reference [29] (values in parentheses)

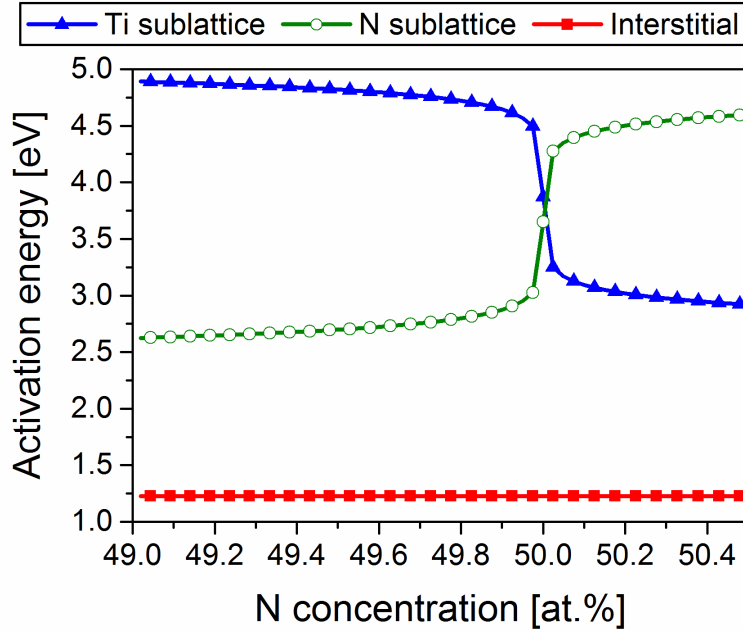


**Figure 6.10:** Activation energy of Cu impurity diffusion in TiN at 1237 K.

This means that the diffusion process of a Cu impurity via a vacancy is limited by the vacancy exchange with a solvent atom in the vicinity of the solute atom. As a consequence, the activation energy for vacancy mediated diffusion transforms into  $Q = E_f + E_b + E_1^m$ .

Combining the results for (i) the vacancy formation energies derived from the DSM calculation, (ii) the binding energy  $E_b$  of a vacancy with a Cu impurity, which is found to be weak and repulsive (0.07 eV) for a  $\text{Cu}_\text{N}-\text{V}_\text{N}$  pair, and attractive (-0.05 eV) for a  $\text{Cu}_\text{Ti}-\text{V}_\text{Ti}$  pair, and (iii) the migration barriers from the NEB, the composition dependent activation energy of Cu impurity diffusion in TiN is obtained as presented in Figure 6.10. It is found that among all possible investigated diffusion mechanisms, the interstitial diffusion mechanism has the lowest activation energy. In the N-deficient region, the mechanism with the second lowest activation energy is Cu impurity diffusion via the N sublattice, while in the N-rich region the diffusion via the Ti sublattice is more favored.

In summary, the calculations show that the diffusion of Cu via interstitial sites has the lowest activation energy as compared to the vacancy-mediated diffusion mechanisms. However, this diffusion mechanism is highly unlikely because of the high formation energy associated with a Cu atom on the interstitial site. Therefore, we propose the diffusion of Cu in TiN to occur via a vacancy mechanism. From the DSM model we conclude that in N-deficient TiN, the Cu diffusion occurs via the N sublattice due to the elevated concentration of N vacancies. This results in a relatively small activation energy of about 2.6 eV for a N concentration of 49 at. % at 1273 K. This theoretical prediction is in good agreement

with the activation energy of 2.7eV obtained experimentally by Moriyama et al. for bulk diffusion of Cu in TiN, although it has to be noted that the TiN films investigated by Moriyama et al. were N-rich [27]. In stoichiometric TiN, however, the formation energy of Cu on the Ti sublattice is significantly lower compared to the N sublattice. For this reason, we expect Cu to diffuse via the Ti sublattice, with a considerably larger activation energy of 3.87 eV, while diffusion on the N sublattice is unlikely to take place, in spite of the slightly lower activation energy of 3.65 eV.

## 6.5 Conclusions

A combination of high-resolution techniques for structural and chemical characterization was used to compare the diffusion of Cu in single- and polycrystalline TiN layers grown by reactive magnetron sputtering under the same deposition conditions. No Cu penetration into the single-crystal barrier could be observed either by TEM or APT after an annealing treatment at 900°C for 1 h. Theoretical studies suggest that at higher temperatures, when diffusion becomes more prominent, the stoichiometry of the TiN film will determine the prevailing atomic diffusion mechanism. This implicates a strong dependence of Cu diffusion properties on the main type of defects in the TiN(001) structure. In the slightly substoichiometric films studied in the present paper, Cu diffusion is therefore expected to occur eventually via vacancy sites on the N sublattice.

In comparison, localized diffusion of Cu occurring along TiN columnar grain boundaries can be observed after the 900°C annealing treatment in the polycrystalline TiN barrier. The penetration depth is non-uniform and is presumably related to the internal structure and density of the respective grain boundaries. Still, the maximum measured diffusion length is only approximately 30 nm, which is considerably smaller than in underdense polycrystalline TiN deposited at low substrate temperatures.

These results for single- and polycrystalline TiN layers highlight the importance of maintaining a dense and, as far as possible, defect-free microstructure to design reliable and efficient diffusion barriers. This can be achieved by epitaxial growth of the TiN and Cu layers on lattice-matched substrates.

### Acknowledgements

The authors are grateful to Jozef Keckes (Department of Materials Physics, Montanuniversität Leoben and Erich Schmid Institute for Materials Science, Austrian Academy of Sciences) for providing the Rigaku system for XRR measurements. Katharina Taferner (Materials Center Leoben Forschung GmbH, Austria) is acknowledged for experimental work. Financial support by the Austrian

Chapter 6. Cu Diffusion in Single-crystal and Polycrystalline TiN Barrier Layers: A High-Resolution Experimental Study Supported by First-principles Calculations

Federal Government (in particular from Bundesministerium für Verkehr, Innovation und Technologie and Bundesministerium für Wirtschaft, Familie und Jugend) represented by Österreichische Forschungsförderungsgesellschaft mbH and the Styrian and the Tyrolean Provincial Government, represented by Steirische Wirtschaftsförderungsgesellschaft mbH and Standortagentur Tirol, within the framework of the COMET Funding Program is gratefully acknowledged. LH acknowledges support from the Swedish Research Council Project Grant #20134018 and the Knut and Alice Wallenberg Foundation for the Electron Microscopy Laboratory at Linköping University operated by the Thin Film Physics Division.

# Chapter 7

## *Ab initio* Study of Cu Impurity Diffusion in Bulk TiN

This chapter provides an extensive DFT study of Cu impurity diffusion in TiN. By studying the vibrational contributions to the free energy, we explicitly calculate the diffusion coefficients for the mechanisms, which were considered in the previous chapter. The temperature dependence of the thermodynamic properties of TiN as well as the thermodynamics of defects was calculated fully from first principles. We identify that the mechanisms of Cu impurity diffusion depend on the TiN stoichiometry and directly compare *ab initio* diffusion coefficients for known mechanism to experimental data. On this basis, we are able to interpret various experimental results in terms of the atomistic mechanisms of diffusion. The results of this work have been published in Physical Review B. This publication [182] is reproduced here and its header is shown in Fig. 7.1.

### Author contributions

This publication is the continuation of the work on theoretical description of the Cu impurity diffusion mechanism in TiN, which has been started in the previous chapter. The core idea of this paper has been developed together by all authors. I have performed and analyzed all DFT calculations presented in this work. Also, I have prepared the figures and written the initial draft of the manuscript. Furthermore, I have participated in the meetings where all authors were discussing the possible interpretations of the experimental measurements based on the diffusion coefficients obtained in this work. Together with all the co-authors of this work, I have iterated the manuscript until its final version.

## ***Ab initio* study of Cu impurity diffusion in bulk TiN**

Anton S. Bochkarev<sup>\*</sup>

*Materials Center Leoben Forschung GmbH (MCL), Roseggerstraße 12, A-8700 Leoben, Austria<sup>†</sup>  
and University of Graz, Institute of Physics, NAWI Graz, Universitätsplatz 5, A-8010 Graz, Austria*

Maxim N. Popov, Vsevolod I. Razumovskiy, and Jürgen Spitaler

*Materials Center Leoben Forschung GmbH (MCL), Roseggerstraße 12, A-8700 Leoben, Austria<sup>†</sup>*

Peter Puschnig

*University of Graz, Institute of Physics, NAWI Graz, Universitätsplatz 5, A-8010 Graz, Austria*

**Figure 7.1:** Header of the article [182], which was published in Physical Review B. It shows the reference, title and all contributing authors with their affiliations. This chapter reproduces this article apart from some possible changes.

### **Abstract**

TiN is an important material used as a diffusion barrier in microelectronic devices to prevent copper from contacting silicon. There is, however, little known about the elementary atomistic processes underlying the excellent performance of TiN. In this work, we perform a density functional theory (DFT) study of the copper impurity diffusion coefficient in bulk TiN. Several diffusion mechanisms are considered. For each mechanism, the temperature effect is taken into account within the quasi-harmonic approximation. Moreover, the influence of the TiN stoichiometry on its diffusion properties is taken into account through the change in the concentrations of the intrinsic point defects as a function of composition. These concentrations are obtained via a thermodynamic formalism based on the dilute solution model. We find that in stoichiometric TiN the copper impurity diffusion proceeds via the vacancy mechanism on the Ti sublattice. In the off-stoichiometric  $\text{TiN}_{0.96}$ , the dominant diffusion mechanism switches to the vacancy-mediated diffusion on the N sublattice. The Arrhenius equation for the diffusion coefficient is  $D = 3.8 \cdot 10^{-4} \exp(-4.5 \text{ eV}/k_B T) \text{ m}^2 \text{ s}^{-1}$  for the stoichiometric TiN and  $D = 6.7 \cdot 10^{-8} \exp(-2.7 \text{ eV}/k_B T) \text{ m}^2 \text{ s}^{-1}$  for the substoichiometric TiN. Our calculations provide the basis for a better interpretation of the experimental measurements.

## **7.1 Introduction**

Owing to their superior properties such as high hardness [135, 183–185], thermal stability [166, 186] and corrosion resistance, transition-metal nitrides have found

wide technological applications in various fields [16, 166, 185–187]. One important application area for transition-metal nitrides is microelectronics, where these materials are often used as diffusion barriers between semiconducting and conducting layers [7, 188]. For instance, TiN is frequently employed as a diffusion barrier to prevent interaction of Cu with Si causing formation of  $\text{Cu}_3\text{Si}$ , which leads to deterioration of the device’s performance [13, 18].

Although there are a great number of experimental works devoted to the study of the TiN diffusion barriers and to finding ways on how to further improve them [12, 14, 16, 20], only a few of them attempt to clarify the underlying diffusion mechanisms. In the earliest work of Chamberlain [25], Cu diffusion in polycrystalline TiN layers was studied in the temperature range between 600 and 700 °C. Chamberlain obtained a value of 4.4 eV for the diffusion activation energy and grain boundary (GB) diffusion was suggested as a mechanism of Cu diffusion in TiN. In contrast, much faster Cu diffusion in polycrystalline TiN films with an activation energy of 0.29 eV in the temperature interval between 400 and 650 °C was observed in the work of Lim et al. [26]. The authors also suggested that GBs are responsible for Cu diffusion. Moriyama et al. [27] observed two different diffusion regimes of Cu diffusion in TiN at temperatures ranging from 600 to 900 °C and suggested two diffusion mechanisms for two temperature intervals: i) a GB diffusion mechanism with the activation energy of 1.4 eV in the “low-temperature” interval between 600 and 800 °C and ii) a bulk diffusion mechanism with the activation energy of 2.7 eV in the “high-temperature” interval between 800 and 900 °C. Similar results, with two different diffusion regimes in two different temperature intervals, were obtained by Lee and Kuo [28] but no suggestions regarding diffusion mechanisms were made. This type of temperature dependence of the diffusion coefficient was also observed for Cu diffusion in other transition-metal nitrides films [28, 189, 190]. In the recent studies of Mühlbacher et al. [24, 133], two estimates for the diffusion coefficients were given. The first one is the diffusion coefficient of Cu in the single-crystalline TiN at 1000 °C, which is significantly lower than the previously reported values. The second one is for the polycrystalline TiN at 900 °C, which is related to the GB diffusion mechanisms, and is close to the data of Lee and Kuo and Moriyama et al.

Taking into account this significant scatter of experimental data on copper diffusion in TiN, a detailed *ab initio* study of the underlying atomic diffusion mechanism is required for a comprehensive understanding of the diffusion properties of TiN. The first steps in this direction have been done in two recent *ab initio* works which have examined several atomic mechanisms of Cu impurity diffusion in TiN and estimated the corresponding migration barriers [29, 133]. However, the results of these studies can only be used for estimates of the relative importance of the various mechanisms and a complete temperature-dependent description of Cu impurity diffusion in TiN is still lacking.

In this work, we have conducted a comprehensive study of the most probable

diffusion mechanisms of Cu in stoichiometric and sub-stoichiometric TiN and obtained absolute values of the corresponding diffusion coefficients as a function of temperature in the interval from 650 to 1250 K. The accuracy of the applied computational approach has been verified by direct comparison to experimental data as well as by calculating a list of selected thermodynamic properties of TiN and comparing them to available literature data. The present study sheds light on the atomistic nature TiN acting as a diffusion barrier and may assist with an interpretation of the experimental observations.

## 7.2 Methodology

In the present study, we consider two types of mechanisms for copper impurity diffusion: a vacancy-mediated and an interstitial diffusion mechanism.

### Vacancy-mediated Diffusion

Vacancy-mediated diffusion can occur either on the titanium or on the nitrogen sublattice. When considering a specific diffusion mechanism, we expect that the impurity atom moves only on one of the two sublattices and does not jump to a different sublattice during the diffusion process. This assumption is based on the comparison between the formation energies of the copper impurity on different sublattices as will be discussed in more detail in Sec. 7.4.2.

Under the above mentioned assumption and given that both titanium and nitrogen sublattices represent ideal fcc lattices, we are able to describe a vacancy-mediated diffusion process in TiN using an apparatus developed for fcc lattices. In this case, the impurity diffusion coefficient  $D$  on either sublattice can be written as [73]:

$$D = a^2 f_2 \omega_2 C_v \exp\left(-\frac{G^b}{k_B T}\right). \quad (7.1)$$

Here,  $a$  is the lattice parameter,  $f_2$  is the impurity diffusion correlation factor,  $C_v$  is the vacancy concentration, and  $\omega_2 = \frac{k_B T}{h} \exp\left(-\frac{G_2^m}{k_B T}\right)$  is the impurity jump rate from transition state theory [63] with  $G_2^m$  being the impurity migration free energy. Finally,  $G^b$  is the binding free energy of the impurity atom with a vacancy. The binding free energy in the dilute limit, in turn, is determined as the difference between the vacancy formation energy in the vicinity of the impurity atom and in the pure bulk and can be calculated as [191–193]:

$$G^b = G_{\text{vac,imp}} - G_{\text{imp}} + G_{\text{bulk}} - G_{\text{vac}}. \quad (7.2)$$

In this equation,  $G_{\text{vac,imp}}$  denotes the free energy of the system containing the impurity atom with a vacancy in its nearest neighbor site,  $G_{\text{imp}}$  is the free energy

## 7.2. Methodology

of the system with the impurity atom,  $G_{\text{bulk}}$  is the free energy of the pure bulk system and  $G_{\text{vac}}$  is the free energy of the system containing a vacancy. In this formulation negative binding energies correspond to attractive interactions between the vacancy and the impurity, whereas positive binding energies correspond to the repulsive interactions.

Within the formalism of the five-frequency model [70, 71], the correlation factor  $f_2$  can be described as follows [74]:

$$f_2 = \frac{2\omega_1 + 7F\omega_3}{2\omega_2 + 2\omega_1 + 7F\omega_3}, \quad (7.3)$$

where  $F$  is given by

$$7F = 7 - \frac{10\alpha^4 + 180.5\alpha^3 + 927\alpha^2 + 1341\alpha}{2\alpha^4 + 40.2\alpha^3 + 254\alpha^2 + 597\alpha + 436}. \quad (7.4)$$

Here,  $\omega_i = \frac{k_B T}{h} \exp\left(-\frac{G_i^m}{k_B T}\right)$  are the rates of the different types of the vacancy jumps in the nearest neighbor sites of an impurity atom, where  $G_i^m$  denotes the migration free energy of the corresponding jump.  $\omega_2$  corresponds to the impurity-vacancy exchange jumps,  $\omega_1$  is the rate of vacancy-solvent jumps in the first coordination sphere of the impurity atom,  $\omega_3$  is the rate of vacancy jumps from the first-nearest neighbor positions of an impurity atom to more distant sites, and  $\omega_4$  is the rate of reverse jumps. All other vacancy-solvent jumps are assumed to occur at a rate of  $\omega_0$ , which corresponds to the solvent-vacancy exchange jump in the pure solvent. Finally,  $\alpha$  is given by the ratio  $\alpha = \omega_4/\omega_0$ . A schematic representation of the various types of processes included in the ‘‘five-frequency’’ model are depicted in Fig. 3.5.

In our previous investigations [133], we have already calculated migration barriers corresponding to all the vacancy jumps. We have found that the correlation factor  $f_2$  (Eq. 7.3) for the copper impurity diffusion in TiN can be approximated as  $f_2 \approx \omega_1/\omega_2$  since the term  $2\omega_1$  in the numerator of Eq. 7.3 is much larger than  $7F\omega_3$  (due to the much lower energy barrier of the respective migration) and  $2\omega_2 \gg (2\omega_1 + 7F\omega_3)$  in the denominator (due to the even lower migration energy). Therefore, the diffusion coefficient of the vacancy-mediated copper impurity diffusion in TiN can be simplified as:

$$D \approx a^2 C_v \omega_1 \exp\left(-\frac{G^b}{k_B T}\right). \quad (7.5)$$

This means that diffusion of a copper impurity in TiN via a vacancy mechanism is limited by the exchange jumps of a vacancy with a solvent atom in the vicinity of an impurity atom.

### Interstitial Diffusion

The interstitial diffusion coefficient can be expressed in the following form [56]:

$$D = \frac{k_B T}{h} \frac{Z}{6} l^2 \exp\left(-\frac{G_I^m}{k_B T}\right). \quad (7.6)$$

Here,  $Z$  is the number of the equivalent directions for diffusion,  $l$  is the length of the diffusion jump and  $G_I^m$  is the free energy of the impurity migration between adjacent interstitial positions. Specifically, for the mechanism considered in this work  $Z = 6$  and  $l$  equals the lattice parameter  $a$ .

## 7.3 Computational Details

All calculations presented in this work are performed within the framework of density functional theory (DFT) as implemented in the Vienna *ab initio* simulation package [119, 153]. For exchange and correlation effects, we employ a generalized-gradient approximation using the PBEsol parametrization [54] which is known to perform well in the description of the properties of solids [48]. Ion-electron interactions are described using the projector augmented wave method [115], with a plane-wave energy cut off of 400 eV. For all calculations we use a  $2 \times 2 \times 2$  supercell of TiN, consisting of 64 atoms in the defect-free cell. For these supercells, a Monkhorst-Pack k-point mesh [120] of  $10 \times 10 \times 10$  is used for Brillouin zone sampling with a Methfessel-Paxton [154] smearing of 0.2 eV. The high k-point mesh density is essential for obtaining accurate forces and, therefore, for calculating phonon properties. In order to understand the impact of defects on the electronic structure, we compare the electronic density of states (DOS) for bulk TiN with the system containing a vacancy on both the Ti and N sublattices. It turned out that the vacancies have only a minor impact on the electronic structure. Especially, they hardly change the DOS at the Fermi level, i.e., the metallic character of the system is not affected.

The procedure of calculating the diffusion coefficient of the copper impurity atom in TiN is based on the methodology described above and consists of the following steps: (i) We calculate the thermal lattice expansion of TiN using the quasi-harmonic approximation (QHA). Based on these results, we choose five lattice parameters corresponding to temperatures of 650, 800, 950, 1100 and 1250 K for which the diffusion coefficient will be calculated. (ii) At each temperature, viz. lattice parameter, the total energy is calculated for the ground state structure both, without defects and with the considered defects, which are vacancies on the two sublattices, an impurity atom, and pairs of an impurity atom and a vacancy. Here we do not take into account the effect of a defect formation volume. This introduces only an insignificant error in the free energy since close to its

minimum changes with volume are of second order. (iii) In order to find the transition state structure and the energy for the diffusive jumps, we apply the nudged elastic band method (NEB) [155]. Here, we checked the influence of the supercell size on the migration barriers. For the nitrogen atom jumps at 1250 K, the migration energy differs only by about 2 % between the supercell calculations containing 64 atoms and 216 atoms. This implies that a 64-atom supercell is already sufficiently large for obtaining accurate migration energies. (iv) We calculate the vibrational free energies for all structures calculated in the previous steps. To this end, the phonon frequencies are obtained using the finite displacement method as realized in the Phonopy program package [129]. (v) At this point the interstitial diffusion coefficient is calculated. To compute the vacancy-mediated diffusion coefficients, the equilibrium defect concentrations as a function of TiN composition close to stoichiometry is calculated with the dilute solution model [76] (DSM) as implemented in the modified PyDII code [156].

## 7.4 Results and Discussion

### 7.4.1 Thermal Properties

We calculate thermal properties of TiN using the quasi-harmonic approximation (QHA). We calculate the free energy of bulk TiN as a function of volume  $V$  and temperature  $T$  as:

$$G(V, T) = E_0(V) + G_{\text{vib}}(T, V), \quad (7.7)$$

where  $E_0(V)$  is the total electron energy and  $G_{\text{vib}}(T, V)$  is the vibrational free energy [194]. Contributions to the free energy from electronic excitations, as well as the  $pV$ -term are neglected.

We use the free energies defined in Eq. 7.7 to determine the temperature dependence of the lattice parameter  $a$ , the linear thermal expansion coefficient  $\alpha$  as well as the heat capacity  $C_p$  of TiN. These results are presented in Fig. 7.2. Panel (a) displays the calculated lattice parameter (full line) as a function of temperature compared to the available experimental data. The resulting thermal expansion coefficient as well as the calculated heat capacity of TiN are compared to the experimental and *ab initio* data from the literature in panels (b) and (c) respectively. All our results agree very well with the literature data apart from a slight offset of the absolute value of  $a$  which is typical for the chosen exchange-correlation functional [49].

Given that the obtained results for  $\alpha$  and  $C_p$  reproduce the experimental data quite well, we use those theoretical lattice constants in all subsequent calculations of defect formation and migration and binding energies, as well as in the calculations of vibrational frequencies at finite temperatures described in the following sections.

### 7.4.2 Point Defects

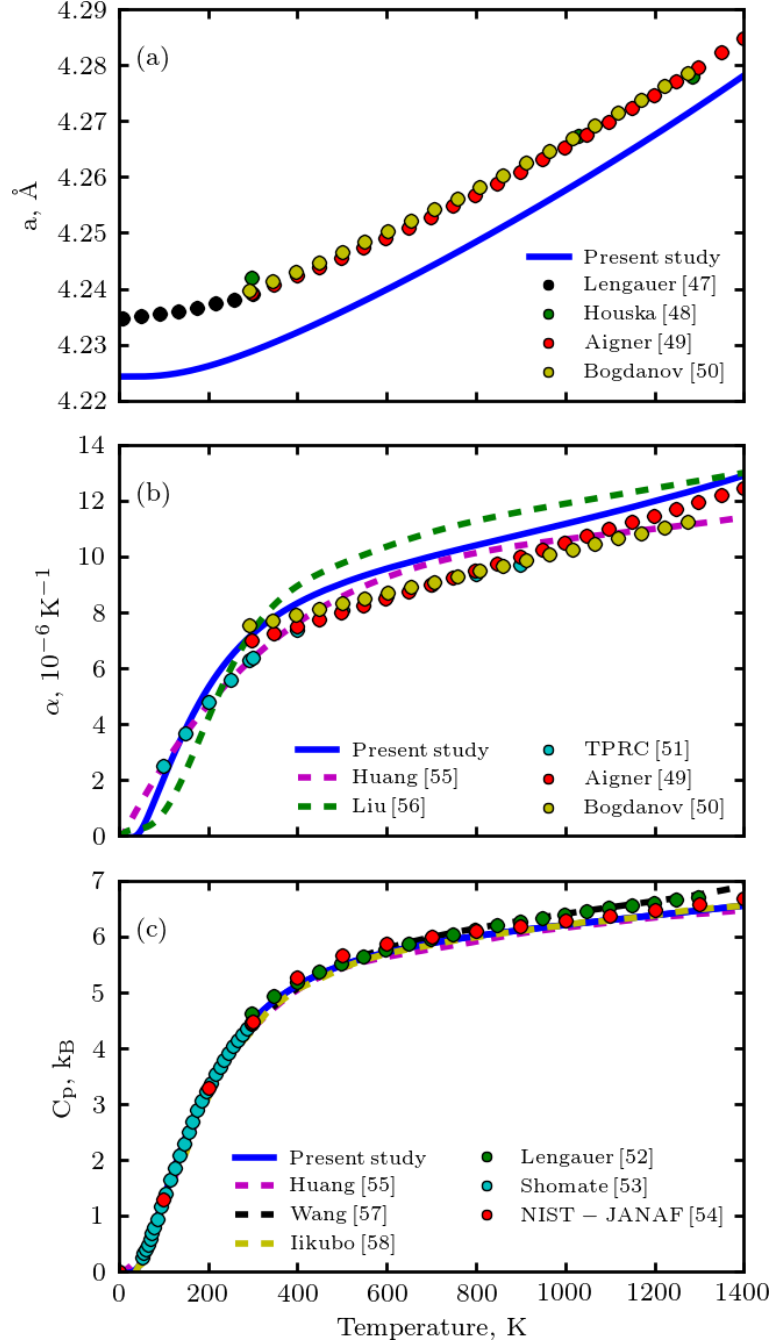
We apply the DSM for calculating the concentration of defects in TiN as a function of composition to investigate how the stoichiometry of TiN affects the diffusion properties. Off-stoichiometry in TiN can be realized via point defects, such as titanium ( $V_{\text{Ti}}$ ) and nitrogen ( $V_{\text{N}}$ ) vacancies, anti-sites ( $\text{Ti}_{\text{N}}$ ,  $\text{N}_{\text{Ti}}$ ), and interstitials ( $\text{I}_{\text{N}}$ ,  $\text{I}_{\text{Ti}}$ ). In our previous investigation [133], we have found that the concentration of vacancies is significantly higher than that for the other defects. Therefore, here we consider only vacancies being responsible for the TiN off-stoichiometry.

Figure 7.3(a) presents the vacancy concentration on Ti- and N- sublattices calculated at a set of selected temperatures ranging from 650 to 1250 K. Here we will mainly focus on the N-deficient side of the plot shaded in red. As we can see from the DSM results, in this case the concentration of N-vacancies is virtually unaffected by temperature, whereas the concentration of Ti-vacancies has a strong dependence: the amount of  $V_{\text{Ti}}$  gradually increases as the temperature grows.

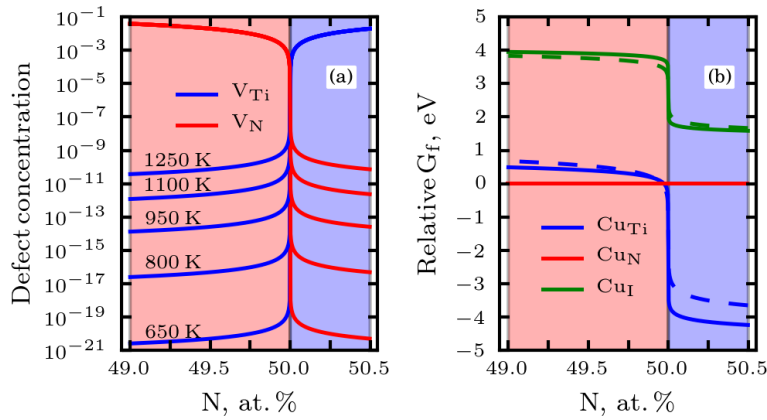
Such a behavior indicates the different character of Ti and N vacancies: While the  $V_{\text{N}}$  have constitutional (structural) character, i.e., they are responsible for the off-stoichiometry, the  $V_{\text{Ti}}$  have thermal nature, i.e. they are excited by temperature. An analogous picture is observed in the Ti-deficient (blue) region in Fig. 7.3(a) for constitutional  $V_{\text{Ti}}$  and thermal  $V_{\text{N}}$  respectively. Since the concentration of vacancies is orders of magnitude higher than that of interstitials or anti-sites (not shown in Fig. 7.3(a)), we can assume the minute role of the diffusion mechanisms involving these defects. For instance, diffusion mechanisms that require nitrogen interstitials can be neglected, which is supported by a molecular dynamics study of the nitrogen self-diffusion in TiN by Sangiovanni et al. [195].

Figure 7.3(b) compares the defect formation energies of Cu atoms on Ti sites, N sites and interstitial sites as a function of nitrogen concentration. Note that these energies are defined in the same way as in our previous study [133], namely relative to the energy required to put a Cu impurity atom on the nitrogen sublattice ( $\text{Cu}_{\text{N}}$ ). Using such a definition, a positive sign corresponds to an energy increase in the system when changing sublattice from the nitrogen one. For N-deficient TiN (red-shaded part in Fig. 7.3(b)), the most favorable position for the Cu impurity is on the nitrogen sublattice, while in the stoichiometric and N-rich TiN copper impurities on the titanium sublattice are favored.

A transition from the sublattice, that corresponds to the lowest formation energy of the Cu impurity at a given stoichiometry, to any other sublattice implies a significant energy penalty. On the one hand, this makes such transitions highly unlikely, which justifies the assumption that the diffusion mechanism proceeds only on one sublattice, i.e., the vacancy-driven diffusion. On the other hand, the



**Figure 7.2:** (a) Lattice parameter  $a$ , (b) thermal expansion coefficient  $\alpha$  and (c) heat capacity  $C_p$  per formula unit of TiN as a function of temperature calculated in this work (full lines), compared to the the available experimental [132, 196–202] (dots) and theoretical [203–206] (dashed lines) data.



**Figure 7.3:** (a) Concentrations of vacancies in TiN as a function of composition calculated for the various temperatures. (b) The formation free energy  $G_f$  of the  $Cu_X$  impurity atom on the different sublattices X (Ti, N, I) in TiN. The energies are shown relative to the one of  $Cu_N$ . The full and the dashed lines correspond to the temperatures of 650 K and 1250 K respectively.

reverse transitions are favored, and this fact renders an assumption on the one-sublattice mechanism less convincing in the case of purely interstitial diffusion. The latter, however, does not alter our conclusions due to the exceedingly high formation energy of Cu interstitials.

### 7.4.3 Migration Barriers

We consider interstitial copper diffusion as the first diffusion mechanism. The most stable configuration for a Cu interstitial is found to be the position in the center of a TiN cage with the coordinates  $(\frac{1}{4}, \frac{1}{4}, \frac{1}{4})$  of the conventional unit cell basis vectors. Copper diffusion via an interstitial mechanism proceeds by migrating a copper impurity between such neighboring interstitial sites. We calculate the minimum energy path including the transition state for this process using the NEB method.

The values of the migration total and free energies are presented in Table 7.1 under the column heading  $Cu_I \rightarrow I$ . The energy barrier at 650 K amounts to 1.52 eV which is only slightly increased by 0.03 eV including vibrational entropy contributions. The total migration energy is gradually reduced as the temperature grows due to the increased space available to the migrating Cu atom. This effect is almost entirely compensated when incorporating vibrational contributions resulting in only a marginal decrease of the free energy barrier  $G_I^m$  for interstitial diffusion as a function of temperature. Note that we have found that only 1 intermediate image in the NEB calculation is sufficient. This finding has been checked by computing the migration barrier at 1250 K with 7 images resulting

## 7.4. Results and Discussion

**Table 7.1:** Calculated values for the total energy ( $E$ ) and the free energy ( $G$ ) difference for the various processes and defects in TiN.  $\text{Cu} - \text{V}_\text{N}$  and  $\text{Cu} - \text{V}_\text{Ti}$  is the binding energy of the copper impurity atom with the nitrogen and the titanium vacancy, respectively (the copper impurity atom is placed on the same sublattice as the vacancy);  $\text{Cu}_\text{I} \rightarrow \text{I}$  is the migration energy of the copper impurity atom on the interstitial sublattice;  $\text{N} \rightarrow \text{V}_\text{N}$  and  $\text{Ti} \rightarrow \text{V}_\text{Ti}$  are the migration energies of the nitrogen and titanium atom, respectively, in the adjacent site of the copper impurity atom sitting on the same sublattice. All energies are given in the units of eV.

T, K	a, Å	$\text{Cu} - \text{V}_\text{N}$		$\text{Cu} - \text{V}_\text{Ti}$		$\text{Cu}_\text{I} \rightarrow \text{I}$		$\text{N} \rightarrow \text{V}_\text{N}$		$\text{Ti} \rightarrow \text{V}_\text{Ti}$	
		$E^b$	$G^b$	$E^b$	$G^b$	$E_\text{I}^m$	$G_\text{I}^m$	$E_1^m$	$G_1^m$	$E_1^m$	$G_1^m$
Present study											
650	4.243	0.015	0.09	-0.12	-0.19	1.52	1.55	2.51	2.72	2.81	2.97
800	4.249	0.016	0.11	-0.14	-0.25	1.50	1.55	2.47	2.74	2.76	2.98
950	4.256	0.016	0.13	-0.15	-0.32	1.48	1.54	2.42	2.76	2.72	2.98
1100	4.263	0.015	0.15	-0.17	-0.40	1.46	1.54	2.38	2.78	2.68	3.00
1250	4.271	0.015	0.17	-0.18	-0.46	1.43	1.54	2.33	2.81	2.63	3.00
Tsetseris et al. [29]											
0	4.237	-0.1				1.4		2.8			

in practically the same transition state and barrier. The minimum energy path for this calculation is presented in Fig. 7.4.

The second diffusion mechanism considered in this work is a vacancy-mediated diffusion. As described in Sec. 7.2, the process which is responsible for the vacancy-mediated copper impurity diffusion in TiN is the exchange of the host atom, titanium or nitrogen, with the vacancy in the vicinity of the impurity atom ( $\omega_1$  in Fig. 3.5). The minimum energy path for the migration on the N and Ti sublattices is presented in Fig. 7.4. As can be seen, the presence of a Cu atom breaks the barrier symmetry. As a consequence, instead of one energy maximum at the center of the migration path, as one may expect, a local minimum is found. Although the energy difference between the local minimum and the surrounding energy maxima (see Fig. 7.4) is only about 0.03 eV for the N sublattice, and about 0.04 eV for the Ti sublattice, this structure is a true local minimum as evidenced by the absence of imaginary eigenvalues of the dynamical matrix. In contrast, the energy maxima correspond to the true transition states exhibiting exactly one imaginary vibrational mode.

Here, we would also like to note that in order to identify the minimum energy path and the transition state for the vacancy-mediated diffusion the NEB calculations with 9 intermediate images have been performed on both Ti and N sublattices for the structures corresponding to 1250 K. Migration barriers at different temperatures are evaluated with 1 intermediate image using the saddle point structure obtained at 1250 K, rescaled to match the lattice parameter at the respective temperature.

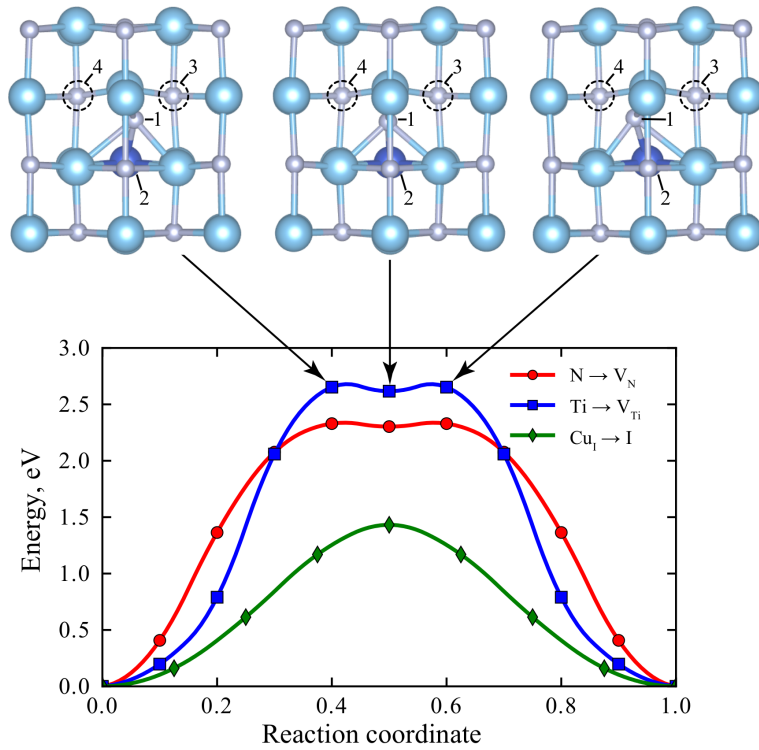


**Figure 7.4:** Minimum energy path during migration of N atom in the vicinity of the copper impurity together with the structures of the intermediate images at 1250 K. 1 denotes the migrating nitrogen atom, 2 is the copper impurity atom, 3 is the initial position of nitrogen atom 1, and 4 is the initial position of the nitrogen vacancy where the atom 1 is migrating to.

The values of the migration total and free energy are presented in Table 7.1, labeled as  $N \rightarrow V_N$  and  $Ti \rightarrow V_{Ti}$  for migration on the N and Ti sublattice, respectively. Similarly to the interstitial mechanism, the migration total energy decreases with the temperature rise due to the lattice expansion. However, in the case of a vacancy mechanism this effect is completely suppressed by the vibrational contributions leading to an increase of the migration free energy with temperature.

Table 7.1 and in Fig. 7.4 illustrate that the lowest migration barrier belongs to the Cu diffusion via the interstitial diffusion mechanism, whereas both vacancy-mediated diffusion mechanisms have almost 1 eV higher barriers. Our results agree with DFT calculations of interstitial Cu diffusion and nitrogen vacancy diffusion data from Ref. [29] (Table 7.1) and suggest that once a Cu interstitial is created, it will be much more mobile than Cu atoms located on either the Ti or Ni sublattice. However, the formation energy of a Cu interstitial is very high; therefore such a defect will be extremely unlikely, compared to  $Cu_N$  and  $Cu_{Ti}$

defects (see Sec. 7.4b). Following Ref. [29] and our data presented in Fig. 7.3(b), it would be reasonable to suggest that copper interstitials will be most likely trapped by nitrogen vacancies and their diffusion will be continued via a vacancy-mediated mechanism.

#### 7.4.4 Diffusion Coefficients

Now, we can use the data from Table 7.1 to calculate the copper impurity diffusion coefficient in TiN. Here, we consider two limiting cases: (i) Cu diffusion in stoichiometric TiN, and (ii) Cu diffusion in substoichiometric  $\text{TiN}_{0.96}$ . The choice of the composition is dictated by two factors. On the one hand, the stoichiometry of experimentally investigated films is commonly nitrogen deficient with the lowest reported value of 0.92 for the N/Ti ratio [24], although, unfortunately, the composition of the TiN films is not always provided. On the other hand, the DSM model is restricted to small deviations from stoichiometry [76] where interactions between defects can be neglected. Therefore, we choose a value of 0.96, which is reasonable for experiments and still within the limitations of the DSM approach. Moreover, it represents a concentration of defects where the off-stoichiometry effect is already fully developed within this approach, as can be seen in Fig. 7.3(a).

For both cases, stoichiometric and N-deficient TiN, we can estimate the total diffusion coefficient as:

$$D_{\text{tot}}(\text{TiN}) = w_{\text{CuN}} D_{V_{\text{N}}} + w_{\text{CuTi}} D_{V_{\text{Ti}}} + w_{\text{ICu}} D_{\text{ICu}}, \quad (7.8)$$

where  $D_{V_{\text{N}}}$ ,  $D_{V_{\text{Ti}}}$  and  $D_{\text{ICu}}$  represent the diffusion coefficients of the N-vacancy-mediated, Ti-vacancy-mediated and Cu interstitial diffusion respectively; and  $w_{\text{CuN}}$ ,  $w_{\text{CuTi}}$  and  $w_{\text{ICu}}$  are the Boltzmann weights related to the probability that a Cu-atom occupies N, Ti or interstitial sites respectively calculated as:

$$w_i = \frac{\exp\left(-\frac{G_i^f}{k_B T}\right)}{\sum_j \exp\left(-\frac{G_j^f}{k_B T}\right)}, \quad (7.9)$$

where  $G_i^f$  is the Cu-atom formation free energy on the  $i$ -th sublattice and the sum in the denominator runs over all considered sublattices  $j$  (Ti and N sublattices as well as the interstitial sites). The result of such a calculation is that for the stoichiometric TiN  $w_{\text{CuTi}} \approx 1 \gg w_{\text{CuN}}$  and  $w_{\text{ICu}}$ , and for the sub-stoichiometric  $\text{TiN}_{0.96}$   $w_{\text{CuN}} \approx 1 \gg w_{\text{CuTi}}$  and  $w_{\text{ICu}}$ . Using these relations we can simplify Eq. 7.8 to:

$$D_{\text{tot}}(\text{TiN}) \approx w_{\text{CuTi}} D_{V_{\text{Ti}}} = D_{V_{\text{Ti}}}, \quad (7.10)$$

$$D_{\text{tot}}(\text{TiN}_{0.96}) \approx w_{\text{CuN}} D_{V_{\text{N}}} = D_{V_{\text{N}}}. \quad (7.11)$$

**Table 7.2:** Calculated values of the effective activation energy  $Q$  and the pre-factor  $D_0$  of the copper impurity diffusion for studied mechanisms and compositions in comparison to the experimental results.

Source	Type	$D_0, m^2 s^{-1}$	$Q, eV$
Present study TiN	$V_{Ti}$ Bulk	$3.8 \cdot 10^{-4}$	4.5
	$V_N$ Bulk	$1.6 \cdot 10^{-7}$	4.1
	I Bulk	$2.9 \cdot 10^{-6}$	1.6
	<i>total</i> Bulk	$3.8 \cdot 10^{-4}$	4.5
Present study TiN <sub>0.96</sub>	$V_{Ti}$ Bulk	$3.9 \cdot 10^{-3}$	5.9
	$V_N$ Bulk	$6.7 \cdot 10^{-8}$	2.7
	I Bulk	$2.9 \cdot 10^{-6}$	1.6
	<i>total</i> Bulk	$6.7 \cdot 10^{-8}$	2.7
M. Moriyama [27]	Bulk	$2.1 \cdot 10^{-7}$	2.7
	GB	$1.2 \cdot 10^{-13}$	1.4
K.Y. Lim [26]	GB	$6.4 \cdot 10^{-15}$	0.29
M.B. Chamberlain [25]	GB	$9 \cdot 10^3$	4.43

To analyze our results and compare them to available experimental data, we use an Arrhenius equation for the diffusion coefficient  $D$  which has the form:

$$D = D_0 \exp(-Q/k_B T). \quad (7.12)$$

Here,  $D_0$  and  $Q$  are the *effective* pre-factor and diffusion activation energy determined from a linear fit of the  $\ln(D)$  as a function of  $1/T$ . Table 7.2 presents the effective parameters  $Q$  and  $D_0$  obtained from the fit for the vacancy-mediated and interstitial impurity diffusion mechanisms considered in this work. Figure 7.5 displays the linear Arrhenius plot of the total diffusion coefficients for TiN and TiN<sub>0.96</sub> along with the available experimental data from the literature [24–28, 133]. One can see that the diffusion coefficient of Cu in stoichiometric TiN is significantly smaller than that in substoichiometric TiN<sub>0.96</sub> in the considered temperature interval. Our data for TiN<sub>0.96</sub> agree well with most of the experimental data in the high temperature region. In particular, agreement with our calculations for the vacancy mechanism on the nitrogen sublattice can be seen for the results of Chamberlain [25] at temperatures 600-635 °C in polycrystalline TiN. However, the author assumed a GB diffusion mechanism. Also, measurement of Mühlbacher et al. [24] for diffusion of Cu in single-crystalline TiN matches our results for stoichiometric TiN although the film of Mühlbacher was not stoichiometric. A probable explanation for these findings is that in both of these experimental works a substantial amount of oxygen was present at the interface between Cu and TiN films. The oxygen atoms might occupy the crystal

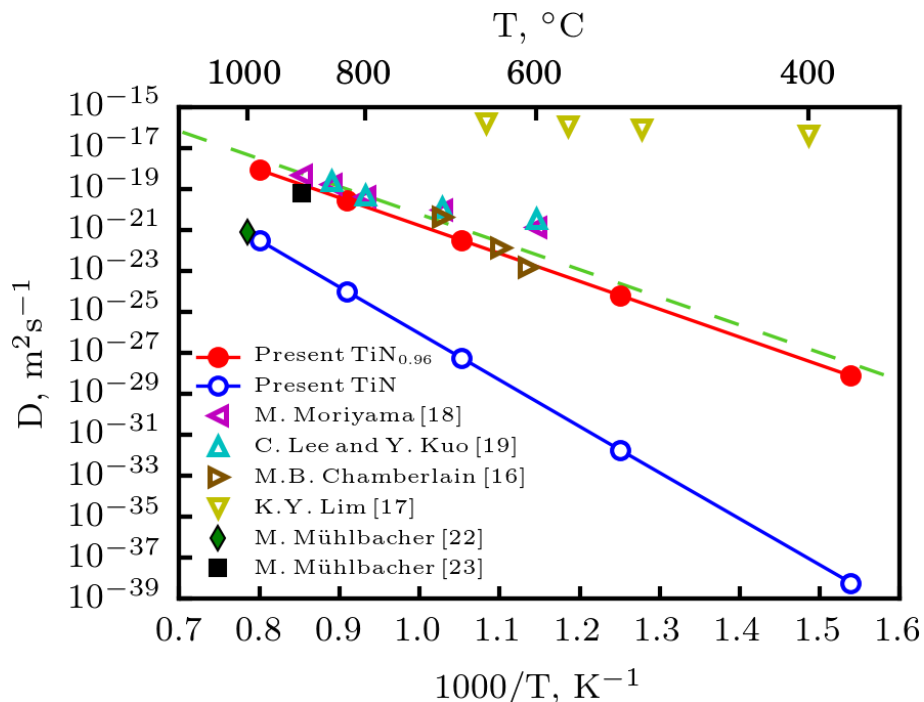


**Figure 7.5:** Arrhenius plot of the calculated diffusion coefficient together with the experimental data. The red line with filled circles corresponds to the calculated diffusion coefficient in N-deficient  $\text{TiN}_{0.96}$ , and the blue one with open circles corresponds to stoichiometric  $\text{TiN}$ . The green diamond represents the measurement for single-crystalline  $\text{TiN}$  [24], while other experimental data are obtained from the measurements in polycrystalline  $\text{TiN}$  [25–28, 133]. An additional dashed green line represents a linear extrapolation of the experimental data [27, 28] obtained at temperatures above 800  $^\circ\text{C}$  which we refer to as “bulk diffusion”, related to the calculated diffusion coefficient in N-deficient  $\text{TiN}_{0.96}$  (shown for illustrative purposes; see the text).

imperfections involved in the fastest diffusion mechanism: GBs in the case of polycrystalline  $\text{TiN}$ , and the nitrogen vacancies in the case of substoichiometric single-crystalline  $\text{TiN}$ . This increases the role of the less prominent mechanisms, such as bulk diffusion on the N sublattice in polycrystalline  $\text{TiN}$ , and the diffusion via  $V_{\text{Ti}}$  in single-crystalline substoichiometric  $\text{TiN}$ .

The measurements of the Cu diffusion coefficient by Lim et al. [26] substantially exceed both the results of our calculations and the other experimental measurements in the corresponding temperature range. Such a fast diffusion could be explained by the presence of the intergranular voids and pores which seem to have been present in the samples investigated by Lim et al. These defects would inevitably increase the diffusion rate, since it would essentially mean that the diffusion process is governed by surface diffusion. The migration energies for Cu on  $\text{TiN}$  surfaces [29] of 0.1–0.36 eV (compared to 0.29 eV of Lim) further support

this assumption.

Moriyama et al. [27] observed a change of the slope in the linear logarithmic Arrhenius plot of the diffusion coefficient at the temperature of 800 °C and a similar behavior of the copper diffusion coefficient in TiN was observed by Lee and Kuo [28]. Moriyama *et al.* suggested that this change originates from the switching of the diffusion mechanism of Cu from the GB diffusion at the temperatures between 600 and 800 °C to the bulk diffusion at higher temperatures. Agreement of the calculated bulk diffusion coefficient of Cu with measurements in the temperature interval of 800-900 °C supports this suggestion (see a linear extrapolation of Moriyamas and Lee and Kuos data at temperatures above 800 °C in Fig. 7.5), and allows us to propose that the mechanism of Cu diffusion in sub-stoichiometric single-crystalline TiN and in polycrystalline TiN at temperatures above 800 °C is the vacancy mediated diffusion on the N sublattice. However, the mechanism of Cu diffusion in polycrystalline TiN at lower temperatures, presumably along the GB, remains unknown and requires additional study.

## 7.5 Summary

To summarize, we have performed an *ab initio* study of the copper impurity diffusion in TiN as a function of composition and temperature. The quasiharmonic approximation (QHA) has been applied to include the effect of the thermal lattice vibrations and the dilute solution model (DSM) to calculate the equilibrium concentrations and effective formation energies of defects. The validity of the chosen methodological approach has been checked by comparison of the obtained theoretical results to experimental and theoretical thermodynamic and kinetic data such as thermal expansion coefficient, heat capacity, and impurity diffusion coefficients. We have considered three possible Cu-impurity diffusion mechanisms in TiN and found that for the stoichiometric TiN the operative diffusion mechanism of the copper impurity is the vacancy-mediated diffusion on the titanium sublattice, while for the N-deficient TiN diffusion occurs via vacancies on the nitrogen sublattice. We have shown that Cu-impurity diffusion in TiN strongly depends on the stoichiometry of the compound providing significantly faster diffusion in the substoichiometric compound accompanied by a change of the dominating diffusion mechanism as the stoichiometry goes from the ideal to N-deficient. Our results confirm the suggestion by Moriyama et al. [27] about the bulk character of high-temperature Cu-impurity diffusion in substoichiometric TiN polycrystalline thin films and reveal the underlying atomic mechanism of diffusion. In order to obtain a complete description of the diffusion processes in polycrystalline TiN, additional studies of the diffusion along the fast diffusion paths, such as grain boundaries, are required.

## **Acknowledgments**

The authors would like to express gratitude to H. Ding for assistance with the DSM calculations. Financial support by the Austrian Federal Government (in particular from Bundesministerium für Verkehr, Innovation und Technologie and Bundesministerium für Wirtschaft, Familie und Jugend) represented by Österreichische Forschungsförderungsgesellschaft mbH and the Styrian and the Tyrolean Provincial Government, represented by Steirische Wirtschaftsförderungsgesellschaft mbH and Standortagentur Tirol, within the framework of the COMET Funding Programme is gratefully acknowledged. The computational results presented have been achieved using the Vienna Scientific Cluster (VSC).



# Chapter 8

## Summary and Conclusions

Here, a summary of the main results of this thesis is given and some conclusions are drawn. After briefly summarizing the basic principles of the density functional theory in Chapter 2, the thesis gives an account of the atomistic theory of diffusion and point defects in solids in Chapters 3 and 4, respectively.

Chapter 5 describes our single-volume approach for point defects thermodynamic calculations. Prior this work it has been known that neglecting the vacancy formation volume leads to errors in the supercell calculations of the vacancy formation free energy, entropy and enthalpy. While an error in the formation free energy is expected to be small, the entropy and enthalpy of formation turn out to be severely wrong. Chapter 5 shows that this issue can be easily overcome by making use of standard thermodynamic relations. Thereby, the proper thermodynamic characteristics of vacancy formation can be obtained ignoring the volume effect due to a vacancy. This approach has been utilized in the following sections for calculating point defect concentrations.

The ultimate goal of this thesis is to obtain the temperature dependent Cu diffusion coefficient in TiN. As a first step, it is important to identify the diffusion mechanism. Hence, Chapter 6 investigates possible mechanisms of Cu diffusion in TiN. Point defects often serve as a diffusion vehicle, so it is important to know the concentration of various defects to suggest a diffusion mechanism. The concentrations of intrinsic point defects depend on the TiN stoichiometry, and since TiN is known to exist over a wide range of compositions, the dilute solution model has been applied to connect the TiN stoichiometry with the concentration of the intrinsic point defects. It was found that the TiN off-stoichiometry is accommodated primarily via vacancies suggesting three diffusion mechanism for Cu: interstitial Cu diffusion (no defects involved), and the vacancy-mediated mechanism on N sublattice and Ti sublattice. In order to calculate the respective migration barriers, the nudged elastic band method has been utilized and the “five-frequency” model has been employed to analyze the correlation effect for

## Chapter 8. Summary and Conclusions

the vacancy-mediated diffusion. According to this model, the limiting factor of Cu diffusion via the vacancy mechanism is the exchange jump of vacancy and the matrix atom. Finally, the diffusion activation energies have been estimated for each of the considered mechanisms. The interstitial mechanism is found to have the lowest activation energy within the whole considered composition range. Nevertheless, it has been argued that this mechanism was unlikely to significantly contribute to the Cu diffusion in TiN due to the high formation energy of the copper interstitial. Thus, it has been concluded that in the N-deficient TiN Cu diffuses via the vacancy mechanism on the N sublattice, while in the stoichiometric TiN it prefers the Ti sublattice.

Chapter 7 aims at obtaining the diffusion coefficients corresponding to the mechanism suggested in the previous chapter. Thereby, a direct comparison between calculations and the experimental data can be made. First, the thermal lattice expansion of TiN is calculated within the quasi-harmonic approximation. Then, for the certain set of temperatures and corresponding lattice parameters, all parameters entering the diffusion equation are calculated, including also the vibrational free energy contributions. In such a way, the coefficients of Cu diffusion in TiN have been obtained corresponding to the various mechanisms and TiN compositions. It is found that in the N-deficient TiN Cu diffusion occurs via a vacancy mechanism on the N sublattice with the Arrhenius equation parameters  $D_0 = 6.7 \cdot 10^{-8} \text{ m}^2\text{s}^{-1}$  and  $Q = -2.7\text{eV}$ . For the stoichiometric TiN, Cu diffusion occurs via a vacancy mechanism on the Ti sublattice with the Arrhenius equation parameters  $D_0 = 3.8 \cdot 10^{-4} \text{ m}^2\text{s}^{-1}$  and  $Q = -4.5\text{eV}$ . A very good agreement has been observed between theory and experiment.

Based on the above-mentioned results, it can be concluded that the main goal of this study has been achieved successfully. The mechanisms of Cu impurity diffusion in TiN have been identified and corresponding diffusion coefficients have been computed entirely from first principles. This work, therefore, illustrates the efficiency of the density functional theory calculations for study the materials diffusion properties and shows that it is particularly useful when there is no prior knowledge regarding the diffusion mechanisms. The knowledge of the atomistic mechanism of diffusion allows one to draw the following conclusions regarding the diffusion process of Cu in TiN films. Firstly, experimental results suggest that there are two main types of Cu diffusion mechanisms in polycrystalline TiN films, namely the grain boundary diffusion and the bulk diffusion. Moreover, it is assumed that there is a transition between these mechanisms from the grain boundary diffusion at low temperatures to the bulk diffusion at higher temperatures. The theoretical results of this thesis confirm this assumption. They also suggest that the temperature at which this crossover occurs depends on the TiN composition. Secondly, the atomistic mechanism of diffusion helps understanding the discrepancy between results of the different experimental diffusion measurements attributed to the same type of the diffusion. Thus, a rather high

concentration of oxygen impurities, which was observed in some experiments at the Cu/TiN interface, prevents Cu diffusion along the fast diffusion paths. This increases the role of less prominent mechanisms, i.e. the vacancy-mediated diffusion on Ti sublattice instead of N sublattice, and the vacancy-mediated diffusion on N sublattice instead of the grain boundary diffusion. However, the exact mechanisms underlying grain boundary diffusion remain unclear. Thus, the examination of the atomic structure of TiN grain boundaries as well as the defects energetics at the grain boundary should be the subject of future studies.



# Acknowledgment

First of all, I would like to thank my colleagues at Materials Center Leoben for their help and for creating a friendly and pleasant work atmosphere. Especially, I want to thank Maxim Popov who is largely responsible for the very existence of this thesis. He was guiding and supporting this work, always was ready to help and answer any of my questions, which often resulted in massive discussions, not necessarily scientific. I am also grateful to Jürgen Spitaler, Vsevolod Razumovskiy and Andrei Ruban for the fruitful collaboration.

I want to express a special gratitude to my supervisor Peter Puschnig for sharing his scientific expertise and providing a constant supply of valuable advices. He spent a great deal of time reviewing all my writings, including this thesis, and it is hard to overestimate his contribution to this work.

I also want to thank my colleagues from Montanuniversität Leoben, namely Christian Mitterer, Marlene Mühlbacher, Nina Schalk and David Holec for collaboration and a number of scientific discussions. I am also thankful to David Holec for reviewing this thesis.

Financial support by the Austrian Federal Government (in particular from Bundesministerium für Verkehr, Innovation und Technologie and Bundesministerium für Wirtschaft, Familie und Jugend) represented by Österreichische Forschungsförderungsgesellschaft mbH and the Styrian and the Tyrolean Provincial Government, represented by Steirische Wirtschaftsförderungsgesellschaft mbH and Standortagentur Tirol, within the framework of the COMET Funding Programme is gratefully acknowledged.

Finally, special recognition goes to all my friends and my family for their support during years of my study.



# List of Figures

3.1	Schematic illustration for a random walk of a particle on a lattice	18
3.2	Atom migration in a crystalline solid from the initial configuration at $x_0$ to the final configuration at $x_1$ passing through the transition state configuration at $x'$ . Circles illustrate the change in atomic configuration during migration while the curve shows the corresponding change in the free energy of the system. . . . .	21
3.3	Schematic illustration of the interstitial diffusion mechanism . . .	26
3.4	Schematic illustration of the vacancy diffusion mechanism . . . . .	27
3.5	Schematic representation of the “five-frequency” model in an fcc lattice. Gray and white balls depict the solvent atoms in the different (100) planes, the black ball is the impurity atom and the squares illustrate the vacancies. . . . .	28
5.1	Header of the article [80], which was published in Europhysics Letters. It shows the reference, title and all contributing authors with their affiliations. This chapter reproduces this article. . . . .	40
5.2	(Color online) Calculated equilibrium lattice parameters of Ag, Al, Pd, Cu, and Mo obtained in the quasi-harmonic approximation as a function of temperature (full lines) compared to the experimental data (symbols) for Al [121–123], Ag [123, 124], Cu [124, 125], Pd [126], Mo [123, 127, 128]. Dashed lines show the equilibrium lattice parameters obtained for supercells with vacancy. . . . .	45
5.3	(Color online) (a) The vacancy formation Gibbs free energy, (b) vacancy formation entropy and (c) vacancy formation enthalpy in Al. $G$ , $S$ , $H$ correspond to the calculations done at the equilibrium volumes of supercells with and they are plotted by solid lines. $\tilde{G}$ , $\tilde{S}$ , $\tilde{H}$ are the vacancy formation free energy, enthalpy and entropy determined in the single-volume approach and plotted by dashed lines with diamonds. The vacancy formation entropy, $S'$ , and enthalpy, $H'$ , are obtained from $\tilde{G}$ using relation (5.2). Black dots show available experimental data [131]. $G_{\text{fit}}$ is the quadratic fit of the experimental temperature dependent vacancy formation free energy shown by black solid line. . . . .	47

## LIST OF FIGURES

5.4	(Color online) (a,b,c,d) The vacancy formation Gibbs free energy; (e,f,g,h) the vacancy formation entropy in Cu, Ag, Pd and Mo, respectively. For notations see Fig 5.3. . . . .	48
6.1	Header of the article [133], which was published in the Journal of Applied Physics. It shows the reference, title and all contributing authors with their affiliations. This chapter reproduces this article.	52
6.2	X-ray diffractograms of pristine TiN/Cu stacks grown on (a) Si(001)/SiO <sub>2</sub> and (b) MgO(001) measured in grazing incidence and Bragg-Brentano geometry. . . . .	58
6.3	TEM images of the pristine single-crystal TiN/Cu stack grown on MgO(001): (a) cross-sectional dark field image giving an overview of the layer arrangement, (b) high-resolution bright field micrograph of the Cu-TiN interface with a misfit dislocation marked by an arrow, and (c) the corresponding SAED pattern showing an epitaxial cube-on-cube orientation relationship between the Cu and the TiN layer. . . . .	59
6.4	TEM images of the pristine polycrystalline TiN/Cu stack grown on Si/SiO <sub>2</sub> : (a) cross-sectional bright field image giving an overview of the layer arrangement, (b) dark field micrograph displaying no discernible Cu or Si diffusion along the grain boundaries between columnar TiN grains, (c) corresponding SAED pattern showing (111), (002), and (220) diffraction rings related to TiN, and (d) a high-resolution bright field micrograph of the Cu-TiN interface with two grain boundaries marked by arrows. . . . .	61
6.5	(a) Experimental and calculated XRR (fitted by a genetic algorithm fit according to the Nevot-Croce interface model) curves and (b) corresponding density depth profile of the polycrystalline TiN/Cu stack grown on Si/SiO <sub>2</sub> at 700°C. . . . .	62
6.6	STEM-HAADF images and corresponding EDX maps (pixel size 1 × 1 nm) of the Cu-K and the Ti-K edges of the (a) single-crystal TiN/Cu stack grown on MgO(001) and (b) polycrystalline TiN/Cu stack grown on Si/SiO <sub>2</sub> after the annealing treatment (900°C, 1 h).	63
6.7	Three-dimensional APT reconstructions (∅ 20 nm × 100 nm) and corresponding Cu concentration plots of the (a) single-crystal TiN/Cu stack grown on MgO(001) and (b) polycrystalline TiN/Cu stack grown on Si/SiO <sub>2</sub> after the annealing treatment (900°C, 1 h).	65
6.8	Effective formation energy of point defects in TiN as a function of composition obtained from the DSM at a temperature of 1273 K.	69
6.9	Formation energy $E_f(\text{Cu}_x)$ of a Cu impurity on different sites in TiN as a function of composition at 1273 K. . . . .	70
6.10	Activation energy of Cu impurity diffusion in TiN at 1237 K. . . .	72

## LIST OF FIGURES

7.1	Header of the article [182], which was published in Physical Review B. It shows the reference, title and all contributing authors with their affiliations. This chapter reproduces this article apart from some possible changes. . . . .	76
7.2	(a) Lattice parameter $a$ , (b) thermal expansion coefficient $\alpha$ and (c) heat capacity $C_p$ per formula unit of TiN as a function of temperature calculated in this work (full lines), compared to the available experimental [132, 196–202] (dots) and theoretical [203–206] (dashed lines) data. . . . .	83
7.3	(a) Concentrations of vacancies in TiN as a function of composition calculated for the various temperatures. (b) The formation free energy $G_f$ of the $Cu_X$ impurity atom on the different sublattices X (Ti, N, I) in TiN. The energies are shown relative to the one of $Cu_N$ . The full and the dashed lines correspond to the temperatures of 650 K and 1250 K respectively. . . . .	84
7.4	Minimum energy path during migration of N atom in the vicinity of the copper impurity together with the structures of the intermediate images at 1250 K. 1 denotes the migrating nitrogen atom, 2 is the copper impurity atom, 3 is the initial position of nitrogen atom 1, and 4 is the initial position of the nitrogen vacancy where the atom 1 is migrating to. . . . .	86
7.5	Arrhenius plot of the calculated diffusion coefficient together with the experimental data. The red line with filled circles corresponds to the calculated diffusion coefficient in N-deficient $TiN_{0.96}$ , and the blue one with open circles corresponds to stoichiometric TiN. The green diamond represents the measurement for single-crystalline TiN [24], while other experimental data are obtained from the measurements in polycrystalline TiN [25–28, 133]. An additional dashed green line represents a linear extrapolation of the experimental data [27, 28] obtained at temperatures above 800 °C which we refer to as “bulk diffusion”, related to the calculated diffusion coefficient in N-deficient $TiN_{0.96}$ (shown for illustrative purposes; see the text). . . . .	89



# List of Tables

6.1	Calculated excitation energies of intrinsic point defects in TiN. The ground state energy per formula unit of the stoichiometric TiN is $E_0 = -19.912$ eV. . . . .	68
6.2	Migration barriers $E_i^m$ [eV] corresponding to the different vacancy exchange jumps ( $\omega_i$ ) in the vicinity of the impurity atom and for migration via interstitial sites calculated with the lattice parameters at 0 K and 1273 K. . . . .	71
7.1	Calculated values for the total energy ( $E$ ) and the free energy ( $G$ ) difference for the various processes and defects in TiN. $\text{Cu} - \text{V}_\text{N}$ and $\text{Cu} - \text{V}_\text{Ti}$ is the binding energy of the copper impurity atom with the nitrogen and the titanium vacancy, respectively (the copper impurity atom is placed on the same sublattice as the vacancy); $\text{Cu}_\text{I} \rightarrow \text{I}$ is the migration energy of the copper impurity atom on the interstitial sublattice; $\text{N} \rightarrow \text{V}_\text{N}$ and $\text{Ti} \rightarrow \text{V}_\text{Ti}$ are the migration energies of the nitrogen and titanium atom, respectively, in the adjacent site of the copper impurity atom sitting on the same sublattice. All energies are given in the units of eV. . . . .	85
7.2	Calculated values of the effective activation energy $Q$ and the pre-factor $D_0$ of the copper impurity diffusion for studied mechanisms and compositions in comparison to the experimental results. . . . .	88



# Bibliography

- [1] International Technology Roadmap for Semiconductors (ITRS), 2013.
- [2] International Technology Roadmap for Semiconductors (ITRS), 2007.
- [3] Gopal Raghavan, Chien Chiang, Paul B. Anders, Sing-Mo Tzeng, Reynaldo Villasol, Gang Bai, Mark Bohr, and David B. Fraser. Diffusion of copper through dielectric films under bias temperature stress. *Thin Solid Films*, 262(1):168 – 176, 1995.
- [4] A.A. Istratov and E.R. Weber. Electrical properties and recombination activity of copper, nickel and cobalt in silicon. *Applied Physics A*, 66(2):123–136, 1998.
- [5] A. A. Istratov, H. Hedemann, M. Seibt, O. F. Vyvenko, W. Schrter, T. Heiser, C. Flink, H. Hieslmair, and E. R. Weber. Electrical and recombination properties of coppersilicide precipitates in silicon. *Journal of The Electrochemical Society*, 145(11):3889–3898, 1998.
- [6] P.S. Ho. General aspects of barrier layers for very-large-scale integration applications I: Concepts. *Thin Solid Films*, 96(4):301 – 316, 1982.
- [7] M.-A. Nicolet. Diffusion barriers in thin films. *Thin Solid Films*, 52(3):415 – 443, 1978.
- [8] L. E. Toth. *Transition metal carbides and nitrides*. Academic Press, New York, 1971.
- [9] J.-E. Sundgren. Structure and properties of TiN coatings. *Thin Solid Films*, 128(1-2):21–44, 1985.
- [10] S. C. Sun, M. H. Tsai, H. T. Chiu, S. H. Chuang, and C. E. Tsai. A comparative study of CVD TiN and CVD TaN diffusion barriers for copper interconnection. In *Proceedings of International Electron Devices Meeting*, pages 461–464, 1995.

## BIBLIOGRAPHY

- [11] Ki-Chul Park and Ki-Bum Kim. Effect of annealing of titanium nitride on the diffusion barrier property in Cu metallization. *Journal of The Electrochemical Society*, 142(9):3109–3115, 1995.
- [12] Ki-Chul Park, Ki-Bum Kim, Ivo J. M. M. Raaijmakers, and Ken Ngan. The effect of density and microstructure on the performance of TiN barrier films in Cu metallization. *Journal of Applied Physics*, 80(10):5674–5681, 1996.
- [13] J. Baumann, T. Werner, A. Ehrlich, M. Rennau, Ch. Kaufmann, and T. Gessner. TiN diffusion barriers for copper metallization. *Microelectronic Engineering*, 37/38(0):221 – 228, 1997.
- [14] Sa-Kyun Rha, Won-Jun Lee, Seung-Yun Lee, Yong-Sup Hwang, Yoon-Jik Lee, Dong-Il Kim, Dong-Won Kim, Soung-Soon Chun, and Chong-Ook Park. Improved TiN film as a diffusion barrier between copper and silicon. *Thin Solid Films*, 320(1):134 – 140, 1998.
- [15] Sa-Kyun Rha, Seung-Yun Lee, Won-Jun Lee, Yong-Sup Hwang, Chong-Ook Park, Dong-Won Kim, Youn-Seoung Lee, and Chung-Nam Whang. Characterization of TiN barriers against Cu diffusion by capacitance-voltage measurement. *Journal of Vacuum Science & Technology B: Microelectronics and Nanometer Structures*, 16(4):2019–2019, 1998.
- [16] M.Y. Kwak, D.H. Shin, T.W. Kang, and K.N. Kim. Characteristics of TiN barrier layer against Cu diffusion. *Thin Solid Films*, 339(12):290 – 293, 1999.
- [17] Dong-Jin Kim, Young-Bae Jung, Myoung-Bok Lee, Yong-Hyun Lee, Jong-Hyun Lee, and Jung-Hee Lee. Applicability of ALE TiN films as Cu/Si diffusion barriers. *Thin Solid Films*, 372(12):276 – 283, 2000.
- [18] S. Riedel, S.E. Schulz, J. Baumann, M. Rennau, and T. Gessner. Influence of different treatment techniques on the barrier properties of MOCVD TiN against copper diffusion. *Microelectronic Engineering*, 55:213 – 218, 2001.
- [19] Ki Tae Nam, Arindom Datta, Soo-Hyun Kim, and Ki-Bum Kim. Improved diffusion barrier by stuffing the grain boundaries of TiN with a thin Al interlayer for Cu metallization. *Applied Physics Letters*, 79(16):2549–2551, 2001.
- [20] Wen-Horng Lee, Yu-Lin Kuo, Hong-Ji Huang, and Chiapyng Lee. Effect of density on the diffusion barrier property of TiNx films between Cu and Si. *Materials Chemistry and Physics*, 85(23):444 – 449, 2004.

## BIBLIOGRAPHY

- [21] L. C. Yang, C. S. Hsu, G. S. Chen, C. C. Fu, J. M. Zuo, and B. Q. Lee. Strengthening TiN diffusion barriers for Cu metallization by lightly doping Al. *Applied Physics Letters*, 87(12):121911–121911, 2005.
- [22] Young-Joo Lee, Han-Wool Yeon, Sung-Yup Jung, Se-Kwon Na, Jong-Seung Park, Yong-Yoon Choi, Hoo-Jeong Lee, Oh-Sung Song, and Young-Chang Joo. Effects of film thickness and deposition rate on the diffusion barrier performance of titanium nitride in Cu-through silicon vias. *Electronic Materials Letters*, 10(1):275–279, 2014.
- [23] Larissa Djomeni, Thierry Mourier, Stéphane Minoret, Sabrina Fadloun, Fabien Piallat, Steve Burgess, Andrew Price, Yun Zhou, Christopher Jones, Daniel Mathiot, and Sylvain Maitrejean. Study of low temperature MOCVD deposition of TiN barrier layer for copper diffusion in high aspect ratio through silicon vias. *Microelectronic Engineering*, 120:127–132, 2014.
- [24] M. Mühlbacher, F. Mendez-Martin, B. Sartory, N. Schalk, J. Keckes, J. Lu, L. Hultman, and C. Mitterer. Copper diffusion into single-crystalline TiN studied by transmission electron microscopy and atom probe tomography. *Thin Solid Films*, 574:103–109, 2015.
- [25] M.B. Chamberlain. Diffusion of copper in thin TiN films. *Thin Solid Films*, 91(2):155 – 162, 1982.
- [26] K.Y. Lim, Y.S. Lee, Y.D. Chung, I.W. Lyo, C.N. Whang, J.Y. Won, and H.J. Kang. Grain boundary diffusion of Cu in TiN film by X-ray photoelectron spectroscopy. *Applied Physics A*, 70(4):431–434, 2000.
- [27] M Moriyama, T Kawazoe, M Tanaka, and M Murakami. Correlation between microstructure and barrier properties of TiN thin films used Cu interconnects. *Thin Solid Films*, 416(12):136 – 144, 2002.
- [28] Chiapyng Lee and Yu-Lin Kuo. The evolution of diffusion barriers in copper metallization. *JOM*, 59(1):44–49, 2007.
- [29] L. Tsetseris, S. Logothetidis, and S. T. Pantelides. Migration of species in a prototype diffusion barrier: Cu, O, and H in TiN. *Applied Physics Letters*, 94(16):–, 2009.
- [30] M. Born and R. Oppenheimer. Zur Quantentheorie der Molekeln. *Annalen der Physik*, 389(20):457–484, 1927.
- [31] D. R. Hartree. The wave mechanics of an atom with a non-coulomb central field. Part I. Theory and methods. *Mathematical Proceedings of the Cambridge Philosophical Society*, 24(1):89–110, 1928.

## BIBLIOGRAPHY

- [32] V. Fock. Näherungsmethode zur Lösung des quantenmechanischen Mehrkörperproblems. *Zeitschrift für Physik*, 61(1):126–148, 1930.
- [33] Mervyn Roy and P. A. Maksym. Effective mass theory of interacting electron states in semiconducting carbon nanotube quantum dots. *Phys. Rev. B*, 85:205432, 2012.
- [34] P. Hohenberg and W. Kohn. Inhomogeneous electron gas. *Phys. Rev.*, 136:B864–B871, 1964.
- [35] Mel Levy. Electron densities in search of Hamiltonians. *Phys. Rev. A*, 26:1200–1208, 1982.
- [36] W. Kohn. Nobel lecture: Electronic structure of matter—wave functions and density functionals. *Rev. Mod. Phys.*, 71:1253–1266, 1999.
- [37] M. Marques C. Fiolhais, F. Nogueira, editor. *A Primer in Density Functional Theory*. Springer Berlin Heidelberg New York, 2003.
- [38] Mel Levy. Universal variational functionals of electron densities, first-order density matrices, and natural spin-orbitals and solution of the  $v$ -representability problem. *Proceedings of the National Academy of Sciences*, 76(12):6062–6065, 1979.
- [39] W. Kohn and L. J. Sham. Self-consistent equations including exchange and correlation effects. *Phys. Rev.*, 140:A1133–A1138, 1965.
- [40] Murray Gell-Mann and Keith A. Brueckner. Correlation energy of an electron gas at high density. *Phys. Rev.*, 106:364–368, 1957.
- [41] Rosemary A. Coldwell-Horsfall and Alexei A. Maradudin. Zero-point energy of an electron lattice. *Journal of Mathematical Physics*, 1(5):395–404, 1960.
- [42] John P. Perdew and Yue Wang. Accurate and simple analytic representation of the electron-gas correlation energy. *Phys. Rev. B*, 45:13244–13249, 1992.
- [43] D. M. Ceperley and B. J. Alder. Ground state of the electron gas by a stochastic method. *Phys. Rev. Lett.*, 45:566–569, 1980.
- [44] J. P. Perdew and Alex Zunger. Self-interaction correction to density-functional approximations for many-electron systems. *Phys. Rev. B*, 23:5048–5079, 1981.
- [45] S. H. Vosko, L. Wilk, and M. Nusair. Accurate spin-dependent electron liquid correlation energies for local spin density calculations: A critical analysis. *Canadian Journal of Physics*, 58(8):1200–1211, 1980.

## BIBLIOGRAPHY

- [46] John P. Perdew. Generalized gradient approximations for exchange and correlation: A look backward and forward. *Physica B: Condensed Matter*, 172(1):1 – 6, 1991.
- [47] Kieron Burke, John P. Perdew, and Yue Wang. *Derivation of a Generalized Gradient Approximation: The PW91 Density Functional*, pages 81–111. Springer US, Boston, MA, 1998.
- [48] Gábor I. Csonka, John P. Perdew, Adrienn Ruzsinszky, Pier H. T. Philipsen, Sébastien Lebègue, Joachim Paier, Oleg A. Vydrov, and János G. Ángyán. Assessing the performance of recent density functionals for bulk solids. *Phys. Rev. B*, 79:155107, 2009.
- [49] Philipp Haas, Fabien Tran, and Peter Blaha. Calculation of the lattice constant of solids with semilocal functionals. *Phys. Rev. B*, 79:085104, 2009.
- [50] A. D. Becke. Density-functional exchange-energy approximation with correct asymptotic behavior. *Phys. Rev. A*, 38:3098–3100, 1988.
- [51] John P. Perdew, J. A. Chevary, S. H. Vosko, Koblar A. Jackson, Mark R. Pederson, D. J. Singh, and Carlos Fiolhais. Atoms, molecules, solids, and surfaces: Applications of the generalized gradient approximation for exchange and correlation. *Phys. Rev. B*, 46:6671–6687, 1992.
- [52] Chengteh Lee, Weitao Yang, and Robert G. Parr. Development of the Colle-Salvetti correlation-energy formula into a functional of the electron density. *Phys. Rev. B*, 37:785–789, 1988.
- [53] John P. Perdew, Kieron Burke, and Matthias Ernzerhof. Generalized gradient approximation made simple. *Phys. Rev. Lett.*, 77:3865–3868, 1996.
- [54] John P. Perdew, Adrienn Ruzsinszky, Gábor I. Csonka, Oleg A. Vydrov, Gustavo E. Scuseria, Lucian A. Constantin, Xiaolan Zhou, and Kieron Burke. Restoring the density-gradient expansion for exchange in solids and surfaces. *Phys. Rev. Lett.*, 100:136406, 2008.
- [55] Adolph Fick. V. On liquid diffusion. *Philosophical Magazine Series 4*, 10(63):30–39, 1855.
- [56] Helmut Mehrer. *Diffusion in Solids*. Springer, 2007.
- [57] Richard Ghez. *A Primer Of Diffusion Problems*. Wiley, 1 edition, 1988.
- [58] G. E. Murch. *Diffusion in Crystalline Solids*. Materials science and technology (New York, N.Y.). Academic Press, 1984.

## BIBLIOGRAPHY

- [59] A. Einstein. Über die von der molekularkinetischen Theorie der Wärme geforderte Bewegung von in ruhenden Flüssigkeiten suspendierten Teilchen. *Annalen der Physik*, 322(8):549–560, 1905.
- [60] Albert Einstein. *Investigations on the theory of the Brownian movement*. Dover Publications, New York, 1956.
- [61] Paul Shewmon. *Diffusion in Solids*. Wiley, 2 edition, 1989.
- [62] W. Shockley. *Imperfections in Nearly Perfect Crystals*. Wiley, 1952.
- [63] Henry Eyring. The activated complex in chemical reactions. *The Journal of Chemical Physics*, 3(2):107–115, 1935.
- [64] C. A. Wert. Diffusion coefficient of C in  $\alpha$ -iron. *Phys. Rev.*, 79:601–605, 1950.
- [65] B.S. Bokshteyn, S.Z. Bokshteyn, and A.A. Zhukhovitskiy. *Thermodynamics and kinetics of diffusion in solids*. Metallurgia, Moscow, 1974. (in russian).
- [66] George H. Vineyard. Frequency factors and isotope effects in solid state rate processes. *Journal of Physics and Chemistry of Solids*, 3(12):121 – 127, 1957.
- [67] Louis A. Girifalco. *Statistical Mechanics of Solids*. Monographs on the physics and chemistry of materials 58. Oxford University Press, 2000.
- [68] A. R. Allnatt and A. B. Lidiard. *Atomic transport in solids*. Cambridge University Press, 1993.
- [69] G. L. Montet. Integral methods in the calculation of correlation factors in diffusion. *Phys. Rev. B*, 7:650–662, 1973.
- [70] A B Lidiard. Impurity diffusion in crystals (mainly ionic crystals with the sodium chloride structure). *Philosophical Magazine*, 46:1218, 1955.
- [71] A. D. LeClaire and A. B. Lidiard. LIII. Correlation effects in diffusion in crystals. *Philosophical Magazine*, 1(6):518–527, 1956.
- [72] A. B. Lidiard. The influence of solutes on self-diffusion in metals. *Philosophical Magazine*, 5(59):1171–1180, 1960.
- [73] A. D. Le Claire. Solute diffusion in dilute alloys. *Journal of Nuclear Materials*, 6970(0):70 – 96, 1978.
- [74] John R. Manning. Correlation factors for impurity diffusion. bcc, diamond, and fcc structures. *Phys. Rev.*, 136:A1758–A1766, 1964.

## BIBLIOGRAPHY

- [75] J. W. Gibbs. On the equilibrium of heterogeneous substances. *Transactions of the Connecticut Academy of Arts and Sciences*, 3:108–248, 1874-1878.
- [76] C. Woodward, M. Asta, G. Kresse, and J. Hafner. Density of constitutional and thermal point defects in  $L1_2$   $Al_3Sc$ . *Phys. Rev. B*, 63:094103, 2001.
- [77] Y. Mishin and Chr. Herzig. Diffusion in the Ti-Al system. *Acta Materialia*, 48(3):589 – 623, 2000.
- [78] Green M.S. (eds.) Domb C. Phase transitions and critical phenomena 3. Academic Press, 1974.
- [79] Mark Asta, S. Foiles, and A. Quong. First-principles calculations of bulk and interfacial thermodynamic properties for fcc-based Al-Sc alloys. *Phys. Rev. B*, 57:11265–11275, 1998.
- [80] A. S. Bochkarev, S. O. Zamulko, O. I. Gorbatov, S. I. Sidorenko, P. Puschnig, and A. V. Ruban. A single-volume approach for vacancy formation thermodynamics calculations. *EPL (Europhysics Letters)*, 116(1):16001, 2016.
- [81] Yaakov Kraftmakher. Equilibrium vacancies and thermophysical properties of metals. *Physics Reports*, 299(23):79 – 188, 1998.
- [82] H.-E. Schaefer. Investigation of thermal equilibrium vacancies in metals by positron annihilation. *Phys. Status Solidi A*, 102(1):47–65, 1987.
- [83] H. Ullmaier, editor. *Atomic Defects in Metals*, volume 25 of *Landolt-Börnstein - Group III Condensed Matter*. Springer Berlin Heidelberg, 1991.
- [84] M J Gillan. Calculation of the vacancy formation energy in aluminium. *Journal of Physics: Condensed Matter*, 1(4):689, 1989.
- [85] B. Drittler, M. Weinert, R. Zeller, and P.H. Dederichs. Vacancy formation energies of fcc transition metals calculated by a full potential Green’s function method. *Solid State Communications*, 79(1):31 – 35, 1991.
- [86] H. M. Polatoglou, M. Methfessel, and M. Scheffler. Vacancy-formation energies at the (111) surface and in bulk Al, Cu, Ag, and Rh. *Phys. Rev. B*, 48:1877–1883, 1993.
- [87] W. Frank, U. Breier, C. Elsässer, and M. Fähnle. Properties of monovacancies and self-interstitials in bcc Li: An *ab initio* pseudopotential study. *Phys. Rev. B*, 48:7676–7678, 1993.
- [88] N. Chetty, M. Weinert, T. S. Rahman, and J. W. Davenport. Vacancies and impurities in aluminum and magnesium. *Phys. Rev. B*, 52:6313–6326, 1995.

## BIBLIOGRAPHY

- [89] T. Korhonen, M. J. Puska, and R. M. Nieminen. Vacancy-formation energies for fcc and bcc transition metals. *Phys. Rev. B*, 51:9526–9532, 1995.
- [90] Enrico Smargiassi and Paul A. Madden. Free energies of point defects in sodium from first-principles molecular-dynamics simulations. *Phys. Rev. B*, 51:129–136, 1995.
- [91] W. Frank, U. Breier, C. Elsässer, and M. Fähnle. First-principles calculations of absolute concentrations and self-diffusion constants of vacancies in lithium. *Phys. Rev. Lett.*, 77:518–521, 1996.
- [92] Michael J. Mehl and Dimitrios A. Papaconstantopoulos. Applications of a tight-binding total-energy method for transition and noble metals: Elastic constants, vacancies, and surfaces of monatomic metals. *Phys. Rev. B*, 54:4519–4530, 1996.
- [93] B. Meyer and M. Fähnle. *Ab initio* calculation of the formation energy and the formation volume of monovacancies in Mo. *Phys. Rev. B*, 56:13595–13598, 1997.
- [94] D. E. Turner, Z. Z. Zhu, C. T. Chan, and K. M. Ho. Energetics of vacancy and substitutional impurities in aluminum bulk and clusters. *Phys. Rev. B*, 55:13842–13852, 1997.
- [95] Alessandra Satta, F. Willaime, and Stefano de Gironcoli. Vacancy self-diffusion parameters in tungsten: Finite electron-temperature LDA calculations. *Phys. Rev. B*, 57:11184–11192, 1998.
- [96] Alessandra Satta, F. Willaime, and Stefano de Gironcoli. First-principles study of vacancy formation and migration energies in tantalum. *Phys. Rev. B*, 60:7001–7005, 1999.
- [97] P. A. Korzhavyi, I. A. Abrikosov, B. Johansson, A. V. Ruban, and H. L. Skriver. First-principles calculations of the vacancy formation energy in transition and noble metals. *Phys. Rev. B*, 59:11693–11703, 1999.
- [98] Per Söderlind, L. H. Yang, John A. Moriarty, and J. M. Wills. First-principles formation energies of monovacancies in bcc transition metals. *Phys. Rev. B*, 61:2579–2586, 2000.
- [99] Karin Carling, Göran Wahnström, Thomas R. Mattsson, Ann E. Mattsson, Nils Sandberg, and Göran Grimvall. Vacancies in metals: From first-principles calculations to experimental data. *Phys. Rev. Lett.*, 85:3862–3865, 2000.
- [100] Thomas R. Mattsson and Ann E. Mattsson. Calculating the vacancy formation energy in metals: Pt, Pd, and Mo. *Phys. Rev. B*, 66:214110, 2002.

## BIBLIOGRAPHY

- [101] Karin M. Carling, Göran Wahnström, Thomas R. Mattsson, Nils Sandberg, and Göran Grimvall. Vacancy concentration in Al from combined first-principles and model potential calculations. *Phys. Rev. B*, 67:054101, 2003.
- [102] D. A. Andersson and S. I. Simak. Monovacancy and divacancy formation and migration in copper: A first-principles theory. *Phys. Rev. B*, 70:115108, 2004.
- [103] T. R. Mattsson, N. Sandberg, R. Armiento, and A. E. Mattsson. Quantifying the anomalous self-diffusion in molybdenum with first-principles simulations. *Phys. Rev. B*, 80:224104, 2009.
- [104] Darko Simonovic and Marcel H. F. Sluiter. Impurity diffusion activation energies in Al from first principles. *Phys. Rev. B*, 79:054304, 2009.
- [105] B. Grabowski, L. Ismer, T. Hickel, and J. Neugebauer. *Ab initio* up to the melting point: Anharmonicity and vacancies in aluminum. *Phys. Rev. B*, 79:134106, 2009.
- [106] B. Grabowski, T. Hickel, and J. Neugebauer. Formation energies of point defects at finite temperatures. *Phys. Status Solidi B*, 248(6):1295–1308, 2011.
- [107] R. Nazarov, T. Hickel, and J. Neugebauer. Vacancy formation energies in fcc metals: Influence of exchange-correlation functionals and correction schemes. *Phys. Rev. B*, 85:144118, 2012.
- [108] Bharat Medasani, Maciej Haranczyk, Andrew Canning, and Mark Asta. Vacancy formation energies in metals: A comparison of MetaGGA with LDA and GGA exchange-correlation functionals. *Computational Materials Science*, 101:96 – 107, 2015.
- [109] R. Armiento and A. E. Mattsson. Functional designed to include surface effects in self-consistent density functional theory. *Phys. Rev. B*, 72:085108, 2005.
- [110] Ann E. Mattsson, Ryan R. Wixom, and Rickard Armiento. Electronic surface error in the Si interstitial formation energy. *Phys. Rev. B*, 77:155211, 2008.
- [111] Ann E. Mattsson, Rickard Armiento, Joachim Paier, Georg Kresse, John M. Wills, and Thomas R. Mattsson. The AM05 density functional applied to solids. *The Journal of Chemical Physics*, 128(8), 2008.
- [112] A. Glensk, B. Grabowski, T. Hickel, and J. Neugebauer. Breakdown of the Arrhenius law in describing vacancy formation energies: The importance

## BIBLIOGRAPHY

- of local anharmonicity revealed by ab initio thermodynamics. *Phys. Rev. X*, 4:011018, 2014.
- [113] L Zhao, R Najafabadi, and D J Srolovitz. Finite temperature vacancy formation thermodynamics: local harmonic and quasiharmonic studies. *Modelling and Simulation in Materials Science and Engineering*, 1(4):539, 1993.
- [114] Stephen M. Foiles. Evaluation of harmonic methods for calculating the free energy of defects in solids. *Phys. Rev. B*, 49:14930–14938, 1994.
- [115] P. E. Blöchl. Projector augmented-wave method. *Phys. Rev. B*, 50:17953–17979, 1994.
- [116] G. Kresse and D. Joubert. From ultrasoft pseudopotentials to the projector augmented-wave method. *Phys. Rev. B*, 59:1758–1775, 1999.
- [117] G. Kresse and J. Hafner. *Ab initio* molecular dynamics for liquid metals. *Phys. Rev. B*, 47:558–561, 1993.
- [118] G. Kresse and J. Hafner. *Ab initio* molecular-dynamics simulation of the liquid-metal-amorphous-semiconductor transition in germanium. *Phys. Rev. B*, 49:14251–14269, 1994.
- [119] G. Kresse and J. Furthmüller. Efficient iterative schemes for *ab initio* total-energy calculations using a plane-wave basis set. *Phys. Rev. B*, 54:11169–11186, 1996.
- [120] Hendrik J. Monkhorst and James D. Pack. Special points for Brillouin-zone integrations. *Phys. Rev. B*, 13:5188–5192, 1976.
- [121] A J Cornish and J Burke. A high temperature attachment for an X-ray diffractometer for precision lattice parameter measurements. *Journal of Scientific Instruments*, 42(4):212, 1965.
- [122] G. Langelaan and S. Saimoto. Thermal expansion measurement of pure aluminum using a very low thermal expansion heating stage for x-ray diffraction experiments. *Review of Scientific Instruments*, 70(8):3413–3417, 1999.
- [123] M. E. Straumanis and C. L. Woodward. Lattice parameters and thermal expansion coefficients of Al, Ag and Mo at low temperatures. Comparison with dilatometric data. *Acta Crystallographica Section A*, 27(6):549–551, 1971.
- [124] In-Kook Suh, H. Ohta, and Y. Waseda. High-temperature thermal expansion of six metallic elements measured by dilatation method and X-ray diffraction. *Journal of Materials Science*, 23(2):757–760, 1988.

## BIBLIOGRAPHY

- [125] M. E. Straumanis and L. S. Yu. Lattice parameters, densities, expansion coefficients and perfection of structure of Cu and of Cu–In  $\alpha$  phase. *Acta Crystallographica Section A*, 25(6):676–682, 1969.
- [126] John W. Arblaster. Crystallographic properties of palladium. *Platinum Metals Review*, 56(3):181–189, 2012.
- [127] James W. Edwards, Rudolph Speiser, and Herrick L. Johnston. High temperature structure and thermal expansion of some metals as determined by X-ray diffraction data. I. Platinum, tantalum, niobium, and molybdenum. *Journal of Applied Physics*, 22(4):424–428, 1951.
- [128] R.G. Ross and W. Hume-Rothery. High temperature X-ray metallography: I. A new Debye-Scherrer camera for use at very high temperatures II. A new para-focusing camera III. Applications to the study of chromium, hafnium, molybdenum, rhodium, ruthenium and tungsten. *Journal of the Less Common Metals*, 5(3):258 – 270, 1963.
- [129] Atsushi Togo and Isao Tanaka. First principles phonon calculations in materials science. *Scr. Mater.*, 108:1–5, 2015.
- [130] G. Kresse, J. Furthmüller, and J. Hafner. Ab initio force constant approach to phonon dispersion relations of diamond and graphite. *EPL (Europhysics Letters)*, 32(9):729, 1995.
- [131] Th. Hehenkamp. Absolute vacancy concentrations in noble metals and some of their alloys. *Journal of Physics and Chemistry of Solids*, 55(10):907 – 915, 1994.
- [132] K. Aigner, W. Lengauer, D. Rafaja, and P. Ettmayer. Lattice parameters and thermal expansion of  $\text{Ti}(\text{C}_x\text{N}_{1-x})$ ,  $\text{Zr}(\text{C}_x\text{N}_{1-x})$ ,  $\text{Hf}(\text{C}_x\text{N}_{1-x})$  and  $\text{TiN}_{1-x}$  from 298 to 1473 K as investigated by high-temperature X-ray diffraction. *Journal of Alloys and Compounds*, 215(12):121 – 126, 1994.
- [133] Marlene Mühlbacher, Anton S. Bochkarev, Francisca Mendez-Martin, Bernhard Sartory, Livia Chitu, Maxim N. Popov, Peter Puschnig, Jürgen Spitaler, Hong Ding, Nina Schalk, Jun Lu, Lars Hultman, and Christian Mitterer. Cu diffusion in single-crystal and polycrystalline TiN barrier layers: A high-resolution experimental study supported by first-principles calculations. *Journal of Applied Physics*, 118(8):085307, 2015.
- [134] Shanyong Zhang and Weiguang Zhu. TiN coating of tool steels: a review. *Journal of Materials Processing Technology*, 39(1-2):165 – 177, 1993.
- [135] Paul H. Mayrhofer, Christian Mitterer, Lars Hultman, and Helmut Clemens. Microstructural design of hard coatings. *Progress in Materials Science*, 51(8):1032 – 1114, 2006.

## BIBLIOGRAPHY

- [136] Raymond Constantin and Baham Miremad. Performance of hard coatings, made by balanced and unbalanced magnetron sputtering, for decorative applications. *Surface and Coatings Technology*, 120-121:728–733, 1999.
- [137] Stefano Piscanec, Lucio Colombi Ciacchi, Erik Vesselli, Giovanni Comelli, Orfeo Sbaizero, Sergio Meriani, and Alessandro De Vita. Bioactivity of TiN-coated titanium implants. *Acta Materialia*, 52:1237–1245, 2004.
- [138] A. E. Kaloyeros and E. Eisenbraun. Ultrathin diffusion barriers/liners for gigascale copper metallization. *Annual Review of Materials Science*, 30(1):363–385, 2000.
- [139] Soo-Hyun Kim, Ki Tae Nam, Arindom Datta, and Ki-Bum Kim. Failure mechanism of a multilayer (TiN/Al/TiN) diffusion barrier between copper and silicon. *Journal of Applied Physics*, 92(9):5512–5512, 2002.
- [140] W. Sinke, G. P. A. Frijlink, and F. W. Saris. Oxygen in titanium nitride diffusion barriers. *Applied Physics Letters*, 47(5):471–473, 1985.
- [141] A. Gupta, H. Wang, A. Kvit, G. Duscher, and J. Narayan. Effect of microstructure on diffusion of copper in TiN films. *Journal of Applied Physics*, 93(9):5210–5214, 2003.
- [142] Milton Ohring. *The Materials Science of Thin Films*, page 233. Academic Press, San Diego, 1992.
- [143] Milton Ohring. *The Materials Science of Thin Films*, page 131. Academic Press, San Diego, 1992.
- [144] D. Chen, X. Ma, Y. Wang, and L. Chen. Electronic properties and bonding configuration at the TiN/MgO(001) interface. *Physical Review B*, 69(15):155401–155401, 2004.
- [145] A. M. Minor, E. A. Stach, J. W. Morris, and I. Petrov. In-situ nanoindentation of epitaxial TiN/MgO (001) in a transmission electron microscope. *Journal of Electronic Materials*, 32(10):1023–1027, 2003.
- [146] H. Ljungcrantz, M. Odén, L. Hultman, J. E. Greene, and J.-E. Sundgren. Nanoindentation studies of single-crystal (001)-, (011)-, and (111)-oriented TiN layers on MgO. *Journal of Applied Physics*, 80(12):6725–6733, 1996.
- [147] K. Kutschej, B. Rashkova, J. Shen, D. Edwards, C. Mitterer, and G. Dehm. Experimental studies on epitaxially grown TiN and VN films. *Thin Solid Films*, 516(2-4):369–373, 2007.

## BIBLIOGRAPHY

- [148] J.-E. Sundgren, B.-O. Johansson, S.-E. Karlsson, and H.T.G. Hentzell. Mechanisms of reactive sputtering of titanium nitride and titanium carbide II: Morphology and structure. *Thin Solid Films*, 105(4):367 – 384, 1983.
- [149] I. Petrov, L. Hultman, J.-E. Sundgren, and J. E. Greene. *Journal of Vacuum Science & Technology A: Vacuum, Surfaces, and Films*, volume 10, chapter Polycrystalline TiN films deposited by reactive bias magnetron sputtering: Effects of ion bombardment on resputtering rates, film composition, and microstructure, pages 265–272. 1992.
- [150] L. Névot and P. Croce. Caractérisation des surfaces par réflexion rasante de rayons X. Application à l'étude du polissage de quelques verres silicates. *Revue de Physique Appliquée*, 15(3):761–779, 1980.
- [151] A. Ulyanenkov. Novel methods and universal software for HRXRD, XRR and GISAXS data interpretation. *Applied Surface Science*, 253:106–111, 2006.
- [152] K. Thompson, D. Lawrence, D. J. Larson, J. D. Olson, T. F. Kelly, and B. Gorman. In situ site-specific specimen preparation for atom probe tomography. *Ultramicroscopy*, 107:131–139, 2007.
- [153] G. Kresse and J. Furthmüller. Efficiency of ab-initio total energy calculations for metals and semiconductors using a plane-wave basis set. *Computational Materials Science*, 6(1):15 – 50, 1996.
- [154] M. Methfessel and A. T. Paxton. High-precision sampling for Brillouin-zone integration in metals. *Phys. Rev. B*, 40:3616–3621, 1989.
- [155] Daniel Sheppard, Rye Terrell, and Graeme Henkelman. Optimization methods for finding minimum energy paths. *The Journal of Chemical Physics*, 128(13):–, 2008.
- [156] Hong Ding, Bharat Medasani, Wei Chen, Kristin A. Persson, Maciej Haranczyk, and Mark Asta. PyDII: A python framework for computing equilibrium intrinsic point defect concentrations and extrinsic solute site preferences in intermetallic compounds. *Computer Physics Communications*, 193:118 – 123, 2015.
- [157] Mario Birkholz. *Thin Film Analysis by X-Ray Scattering*. WILEY-VCH Verlag GmbH & Co. KGaA, Weinheim, 2006.
- [158] *International Centre for Diffraction Data, Powder Diffraction File 00-038-1420*,. 2007.

## BIBLIOGRAPHY

- [159] *International Centre for Diffraction Data, Powder Diffraction File 00-004-0836*,. 2007.
- [160] *International Centre for Diffraction Data, Powder Diffraction File 00-045-0946*,. International Center for Diffraction Data, PDF-2/Release. 2007.
- [161] Milton Ohring. *The Materials Science of Thin Films*, page 316. Academic Press, San Diego, 1992.
- [162] J. W. Matthews and A. E. Blakeslee. *Journal of Crystal Growth*, volume 27, chapter Defects in epitaxial multilayers, pages 118–125. 1974.
- [163] S. Cazottes, Z. L. Zhang, R. Daniel, J. S. Chawla, D. Gall, and G. Dehm. Structural characterization of a Cu/MgO(001) interface using CS-corrected HRTEM. *Thin Solid Films*, 519(5):1662–1667, 2010. 37th International Conference on Metallurgical Coatings and Thin Films (ICMCTF).
- [164] G. Abadias and Y. Y. Tse. Determination of intrinsic stresses in textured and epitaxial TiN thin films deposited by dual ion beam sputtering. *Surface and Coatings Technology*, 180-181:33–40, 2004.
- [165] J.-D. Kamminga, Th H. de Keijser, R. Delhez, and E. J. Mittemeijer. On the origin of stress in magnetron sputtered TiN layers. *Journal of Applied Physics*, 88(2000):6332–6345, 2000.
- [166] L Hultman. Thermal stability of nitride thin films. *Vacuum*, 57(1):1 – 30, 2000.
- [167] J. A. Thornton. *Annual Review of Materials Science*, volume 7, chapter High rate thick film growth, pages 239–260. 1977.
- [168] David B. Williams and C. Barry Carter. *Transmission electron microscopy: A textbook for materials science*, page 161. Springer Science+Business Media, New York, 2009.
- [169] H. Wang, Ashutosh Tiwari, X. Zhang, A. Kvit, and J. Narayan. Copper diffusion characteristics in single-crystal and polycrystalline TaN. *Applied Physics Letters*, 81(8):1453–1455, 2002.
- [170] P. Patsalas, C. Charitidis, and S. Logothetidis. The effect of substrate temperature and biasing on the mechanical properties and structure of sputtered titanium nitride thin films. *Surface and Coatings Technology*, 125(1-3):335–340, 2000.
- [171] Carl V. Thompson. Solid-state dewetting of thin films. *Annual Review of Materials Research*, 42(1):399–434, 2012.

## BIBLIOGRAPHY

- [172] J. Yu, J. Bian, L. Jiang, Y. Qiu, W. Duan, F. Meng, and Z. Liu. Tungsten-doped indium oxide thin film as an effective high-temperature copper diffusion barrier. *ECS Solid State Letters*, 3(6):N15–N17, 2014.
- [173] Devendra Gupta. *Diffusion Processes in Advanced Technological Materials*. William Andrew Publishing, Norwich, NY, 2005.
- [174] David B. Williams and C. Barry Carter. *Transmission electron microscopy: A textbook for materials science*, page 616. Springer Science+Business Media, New York, 2009.
- [175] L. Hultman. Ar and excess N incorporation in epitaxial TiN films grown by reactive bias sputtering in mixed Ar/N<sub>2</sub> and pure N<sub>2</sub> discharges. *Journal of Vacuum Science & Technology A: Vacuum, Surfaces, and Films*, 7(3):1187–1187, 1989.
- [176] J.-E. Sundgren, B.-O. Johansson, and S.-E. Karlsson. Mechanisms of reactive sputtering of titanium nitride and titanium carbide I: Influence of process parameters on film composition. *Thin Solid Films*, 105(4):353–366, 1983.
- [177] James P. Schaffer. Defects in hard coatings studied by positron annihilation spectroscopy and x-ray diffraction. *Journal of Vacuum Science & Technology A: Vacuum, Surfaces, and Films*, 10(1):193–193, 1992.
- [178] L. Tsetseris, N. Kalfagiannis, S. Logothetidis, and S. Pantelides. Trapping and release of impurities in TiN: A first-principles study. *Physical Review B*, 78(9):094111–094111, 2008.
- [179] Devendra Gupta. *Diffusion Processes in Advanced Technological Materials*. William Andrew Publishing, Norwich, NY, 2005.
- [180] R. E. Hoffman. *Acta Metallurgica*, volume 4, chapter Anisotropy of grain boundary self-diffusion, pages 97–98. 1956.
- [181] M. Murakami and D. deFontaine. X-ray diffraction study of interdiffusion in bimetallic Ag/Cu thin films. *Journal of Applied Physics*, 47(7):2857–2861, 1976.
- [182] Anton S. Bochkarev, Maxim N. Popov, Vsevolod I. Razumovskiy, Jürgen Spitaler, and Peter Puschnig. *Ab initio* study of Cu impurity diffusion in bulk TiN. *Phys. Rev. B*, 94:104303, 2016.
- [183] A. J. Perry. On the existence of point defects in physical vapor deposited films of TiN, ZrN, and HfN. *Journal of Vacuum Science & Technology A*, 6(3):2140–2148, 1988.

## BIBLIOGRAPHY

- [184] Seung-Hoon Jhi, Jisoon Ihm, Steven G. Louie, and Marvin L. Cohen. Electronic mechanism of hardness enhancement in transition-metal carbonitrides. *Nature*, 399(6732):132–134, 1999.
- [185] J. Musil. Hard and superhard nanocomposite coatings. *Surface and Coatings Technology*, 125(1-3):322 – 330, 2000.
- [186] I. Pollini, A. Mosser, and J.C. Parlebas. Electronic, spectroscopic and elastic properties of early transition metal compounds. *Physics Reports*, 355(1):1 – 72, 2001.
- [187] Douglas E. Wolfe, Brian M. Gabriel, and Michael W. Reedy. Nanolayer (Ti,Cr)N coatings for hard particle erosion resistance. *Surface and Coatings Technology*, 205(19):4569 – 4576, 2011.
- [188] Mikko Ritala, Jaako Niinisto, Susan Krumdieck, Paul Chalker, H Aspinall, Martyn E Pemble, Wayne L Gladfelter, Barry Leese, Ronald A Fischer, Harish Parala, Ravi Kanjolia, Russell D Dupuis, S E Alexandrov, Stuart J C Irvine, Robert Palgrave, and Ivan P Parkin. *Chemical Vapour Deposition*. The Royal Society of Chemistry, Cambridge, 2009.
- [189] Takeo Oku, Eiji Kawakami, Masaki Uekubo, Katsumi Takahiro, Sadae Yamaguchi, and Masanori Murakami. Diffusion barrier property of TaN between Si and Cu. *Applied Surface Science*, 99(4):265 – 272, 1996.
- [190] Yu-Lin Kuo, Hsin-Hung Lee, Chiapyng Lee, Jing-Cheng Lin, Shau-Lin Shue, Mong-Song Liang, and Brian J. Daniels. Diffusion of copper in titanium zirconium nitride thin films. *Electrochemical and Solid-State Letters*, 7(3):C35–C37, 2004.
- [191] James E. Saal and C. Wolverton. Solute-vacancy binding of the rare earths in magnesium from first principles. *Acta Materialia*, 60(1314):5151 – 5159, 2012.
- [192] Dongwon Shin and Christopher Wolverton. First-principles study of solute-vacancy binding in magnesium. *Acta Materialia*, 58(2):531 – 540, 2010.
- [193] Shenyan Huang, Daniel L. Worthington, Mark Asta, Vidvuds Ozolins, Gautam Ghosh, and Peter K. Liaw. Calculation of impurity diffusivities in  $\alpha$ -Fe using first-principles methods. *Acta Materialia*, 58(6):1982 – 1993, 2010.
- [194] A. van de Walle and G. Ceder. The effect of lattice vibrations on substitutional alloy thermodynamics. *Rev. Mod. Phys.*, 74:11–45, 2002.
- [195] D. G. Sangiovanni, B. Alling, P. Steneteg, L. Hultman, and I. A. Abrikosov. Nitrogen vacancy, self-interstitial diffusion, and Frenkel-pair

## BIBLIOGRAPHY

- formation/dissociation in *B1* TiN studied by *ab initio* and classical molecular dynamics with optimized potentials. *Phys. Rev. B*, 91:054301, 2015.
- [196] Walter Lengauer, Peter Ettmayer, and Klaus Yvon. Low-temperature thermal expansion of refractory nitrides. *Journal of the Less Common Metals*, 168(2):L7 – L9, 1991.
- [197] C.R. Houska. Thermal expansion and atomic vibration amplitudes for TiC, TiN, ZrC, ZrN, and pure tungsten. *Journal of Physics and Chemistry of Solids*, 25(4):359 – 366, 1964.
- [198] V.S. Bogdanov, V.S. Neshpor, Yu.D. Kondrashev, A.B. Goncharuk, and A.N. Pityulin. Temperature dependence of the elementary cell constants of Groups III-V transition metal nitrides. *Soviet Powder Metallurgy and Metal Ceramics*, 21(5):412–416, 1982.
- [199] Y.S Touloukian, R.K. Kirby, R.E Taylor, and T.Y.R. Lee. *Thermophysical properties of matter*, volume 13. Plenum Press, 1977.
- [200] W. Lengauer, S. Binder, K. Aigner, P. Ettmayer, A. Guillou, J. Debuigne, and G. Groboth. Solid state properties of group IVb carbonitrides. *Journal of Alloys and Compounds*, 217(1):137 – 147, 1995.
- [201] C. Howard Shomate. Specific heats at low temperatures of TiO, Ti<sub>2</sub>O<sub>3</sub>, Ti<sub>3</sub>O<sub>5</sub>, and TiN. *Journal of the American Chemical Society*, 68(2):310–312, 1946.
- [202] Malcolm W. Chase. NIST-JANAF Thermodynamical tables. *Journal of Physical and Chemical Reference Data*, 9, 1998.
- [203] Shuo Huang, Rui-Zi Li, San-Tao Qi, Bao Chen, and Jiang Shen. Alloying-related trends in thermal properties of ternary TiN-based nitrides. *International Journal of Modern Physics B*, 28(15):1450087, 2014.
- [204] Ke Liu, Xiao-Lin Zhou, Hai-Hua Chen, and Lai-Yu Lu. Phase transition and thermodynamic properties of TiN under pressure via first-principles calculations. *Journal of Thermal Analysis and Calorimetry*, 110(2):973–978, 2012.
- [205] Aijun Wang, ShunLi Shang, Dongdong Zhao, Jiong Wang, Li Chen, Yong Du, Zi-Kui Liu, Tao Xu, and Shequan Wang. Structural, phonon and thermodynamic properties of fcc-based metal nitrides from first-principles calculations. *Calphad*, 37:126 – 131, 2012.
- [206] Satoshi Iikubo, Hiroshi Ohtani, and Mitsuhiro Hasebe. First-principles calculations of the specific heats of cubic carbides and nitrides. *Mater. Trans.*, 51(3):574–577, 2010.